

MULTI-SCALE 3D MODELING OF MESOSPHERIC ELECTRIC
FIELDS AND THUNDERSTORM ELECTRODYNAMICS

A DISSERTATION
SUBMITTED TO THE DEPARTMENT OF ELECTRICAL
ENGINEERING
AND THE COMMITTEE ON GRADUATE STUDIES
OF STANFORD UNIVERSITY
IN PARTIAL FULFILLMENT OF THE REQUIREMENTS
FOR THE DEGREE OF
DOCTOR OF PHILOSOPHY

Rasoul Kabirzadeh

August 2015

© Copyright by Rasoul Kabirzadeh 2015
All Rights Reserved

I certify that I have read this dissertation and that, in my opinion, it is fully adequate in scope and quality as a dissertation for the degree of Doctor of Philosophy.

(Umran S. Inan) Principal Adviser

I certify that I have read this dissertation and that, in my opinion, it is fully adequate in scope and quality as a dissertation for the degree of Doctor of Philosophy.

(Nikolai G. Lehtinen)

I certify that I have read this dissertation and that, in my opinion, it is fully adequate in scope and quality as a dissertation for the degree of Doctor of Philosophy.

(Howard A. Zebker)

Approved for the Stanford University Committee on Graduate Studies

*This dissertation is dedicated to my mother and father
Zahra and Mohammadali
to my brother and sister
Hojjat and Maryam
and to the memory of my sister
Marzieh*

Abstract

Thunderstorms are an important component of the Earth electrical system responsible for maintaining the fair weather potential difference between the Earth and its ionosphere. The electric fields created by thundercloud charges and lightning discharges create upward coupling between the tropospheric storms and the mesospheric regions at altitudes of $\sim 50\text{--}90$ km. The strong and slowly changing electric fields of lightning discharges referred to as quasi-electrostatic fields are capable of electron heating, ionization breakdown and excitation of optical emissions at mesospheric altitudes, resulting in high altitude gas discharges collectively known as transient luminous events. The thundercloud fields also keep the ionospheric electrons at a sustained heating level. The modification of the thunderstorm charges by a lightning discharge results in a transient change in the electron heating level which can be observed as the so-called Early/Fast VLF events: an amplitude and/or phase perturbation in subionospherically propagating VLF waves transmitted by naval submarine and long-range communications systems.

Over the last two decades, experimental observations have created a large data set and have vastly improved our understanding of thunderstorm upward coupling. However, theoretical and numerical models of the physics of the various processes involved are required to help understand the underlying physics of the observed features and to quantify their effects on ionospheric dynamics. With an improved understanding of the physics of these phenomena, we can use them as a remote sensing tool of the Earth's upper atmosphere, especially these altitude regions not easily accessible by satellites.

In this dissertation, we have developed the first three-dimensional model of thunderstorms electrodynamics and the resultant upward coupling between thundercloud systems and the overlying mesosphere and ionosphere. The model can accommodate any realistic background neutral and electron densities and thunderstorm charge distributions. Effects of the Earth's geomagnetic field on atmospheric electrical currents induced by the thundercloud charges and lightning discharges are also investigated. By including a realistic geomagnetic field, we demonstrate that the electrostatic fields of the thundercloud charges mapped to the mesosphere altitudes have been substantially underestimated by previously used 2D models.

The larger electric fields result in a stronger coupling of the thunderstorms and the Earth's upper atmosphere. These fields can map to much farther altitudes in the magnetosphere and create large scale electron irregularities known as whistler ducts that can trap and guide lightning generated whistler waves. This stronger coupling further leads to a more significant sustained heating of the ionospheric electrons which in turn more noticeably interact with the subionospheric propagating VLF signals. Using a 2D subionospheric propagation model of VLF waves, we estimate these perturbations and show that they are in good agreement with experimental observations. The sustained heating of the ionospheric electrons by thunderstorms is thus reintroduced as the most likely mechanism responsible for many of the Early/Fast VLF events.

The developed 3D model can also be used to simulate thunderstorm electrodynamics and lightning evolution. Combined with a physics-based lightning discharge model, we simulated long-time evolution of a thunderstorm electrical environment and the associated lightning activity. Important aspects of experimentally measured thunderstorm electrical features are reproduced. In particular, the model results indicate various phases of thunderstorm lightning activity and the transition of intracloud (IC) to cloud-to-ground (CG) lightning discharges which are consistent with observations of lightning discharges in a typical electrically active thunderstorm.

The new model of thunderstorm electrodynamic evolution reveals many interesting and new insights about lightning physics. Based on these results we propose a new mechanism for cloud-to-ground lightning discharge generation. The new mechanism

is capable of producing cloud-to-ground discharges from a dipolar charge distribution inside the thundercloud. The model results also support previously proposed mechanisms of creation of the lower positive charge layers in thunderstorm charge distributions.

Acknowledgements

The research presented in this dissertation has been benefited immensely from the support, guidance and wisdom of many people to whom I am deeply grateful.

I am indebted to my dissertation advisor Prof. Umran Inan for giving me the opportunity to work on challenging and exciting projects and for his leadership, dedication, and unwavering support during the last four years. His profound scientific insight and vision and his confidence in my abilities were crucial in my academic development. It has been an honor and great privilege to work and learn under his supervision at the VLF group at Stanford.

I am greatly privileged to have Dr. Nikolai Lehtinen as my academic mentor. Nikolai welcomed me to the group from my first day at Stanford and has since inspired and encouraged me on a daily basis. His patience, enthusiasm, and unbounded intellectual talent has provided an intellectually stimulating environment for me to learn and develop as a researcher. I am also grateful for his technical contributions and advice and his experienced perspective during the course of this study.

I would like to express my sincere gratitude to my co-advisor Prof. Howard Zebker for his continual support, especially at critical times during my studies at Stanford and this dissertation research, which has had immeasurable impact on this work.

I sincerely thank Prof. John Pauly for serving as the Chair of my defense committee, and Prof. Sigrid Close for serving on my defense committee.

Special thanks are directed to the wonderful research associates at VLF group. I am thankful to Prof. Robert Marshall for his always open door for fruitful discussions on various topics and sharing his passion of the space science and for helping me with the VLF propagation model presented in Chapter 4. I would like to thank

Prof. Morris Cohen for his many constructive suggestions during the group meetings, which greatly improved the study presented in Chapter 6. I deeply appreciate many useful discussions and contributions of valuable ideas from Drs. Maria Spasojevic and Timothy Bell during various stages of my research.

It is my absolute pleasure to thank the students at VLF group. I owe thanks to Can Liang for helping me to use his TDFL model which was essential for the results presented in Chapter 6. Special recognition goes to Patrick Blaes and David Strauss for keeping the servers running and up to date. I would like to also thank Fadi Zoghzoghy, Justin Li, Vijay Harid, Drew Compston, Austin Sousa, Chris Young, Salman Naqvi, Kevin Graf, Forrest Foust, George Jin, Naoshin Haque, Denys Pidyachiy, Daniel Golden, and Nick Bunch for making my experience at Stanford and VLF group truly memorable.

This research would have not been possible without the training and support I received prior to Stanford years. My sincere gratitude goes to Prof. David Knudsen for introducing me to the field of Space Science and for his seemingly endless support during my masters studies, and to Prof. Behrouz Maraghechi for his support and infectious enthusiasm of scientific research during my undergraduate studies.

I want to thank my many great friends in US, Canada, and Iran for creating a more fulfilling and enjoyable experience throughout the years.

Last but not least, I am forever indebted to my parents for their love, devotion, and unlimited moral support and to my brother and sisters for making many wonderful childhood memories and remaining my best friends throughout these years.

RASOUL KABIRZADEH

Stanford, California

August 27, 2015

This research was supported by Defense Advanced Research Projects Agency under the 'NIMBUS' program, via grant HR0011-10-1-0058 to Stanford University and in part by a Stanford University Fellowship Award.

Contents

Abstract	v
Acknowledgements	viii
1 Introduction	1
1.1 The Earth Electrical Environment	2
1.2 Thunderstorm Electrodynamics	4
1.2.1 Cloud Electrification	4
1.2.2 Lightning	6
1.2.3 Transient Luminous Events as Evidence of Thunderstorms Upward Electrodynamic Coupling	8
1.2.4 VLF Events as Evidence of Thunderstorms-Ionosphere Coupling	12
1.3 Thesis Organization	17
1.4 Scientific Contributions	19
2 Model Formulation	20
2.1 Thundercloud Charging Model	20
2.2 Calculation of Quasi-electrostatic Fields	22
2.3 Ambient Atmosphere and Lower Ionosphere	25
2.4 Nonlinear Effects and Self-consistent Evaluation of Conductivity	28
2.5 The Earth Magnetic Field	30
2.6 Parallel Computing and Domain Decomposition	32
2.7 Solution of QE Equations in Time	35

2.7.1	Exponential Time Differencing Method with Runge-Kutta Time Stepping	36
2.7.2	Implicit Adams-Moulton Method	38
3	Electrostatic Upward Coupling of Thunderstorms	40
3.1	Introduction	41
3.2	Model	44
3.3	Results	48
3.4	Discussion	52
3.4.1	Whistler duct formation	52
3.4.2	Early/Fast VLF events	52
3.4.3	Implications for sprites	53
4	Quiescent Heating of the Lower Ionosphere	54
4.1	Introduction	54
4.2	3D QES Modeling	55
4.3	Propagation Modeling	57
4.4	Results	58
4.5	Discussion	63
5	Lightning Quasi-Electrostatic Fields	66
5.1	Introduction	66
5.2	Model	69
5.3	Results	70
5.3.1	QE Fields at Middle and Low Latitudes	70
5.3.2	Sprite Halos in a Neutral Atmosphere Perturbation	73
6	Thunderstorm and Lightning Evolution	77
6.1	Introduction	77
6.2	Model for Thunderstorm and Lightning Evolution	80
6.2.1	Calculation of Charges and Electric Fields	80
6.2.2	Lightning Discharge	82

6.2.3	Model Integration	83
6.3	Results	85
6.4	Discussion	88
7	Conclusions and Suggestions for Future Work	92
7.1	Summary of results	92
7.2	Suggestions for Future Work	95

List of Tables

4.1	Dependence of VLF transmitter signal perturbation on ionospheric electron density profile and the Earth magnetic field dip angle	61
-----	--	----

List of Figures

1.1	Earth's atmospheric temperature and electron density profile	2
1.2	Collisional charging of ice crystals and graupels	6
1.3	Transient Luminous Events	9
1.4	Schematic mechanism of sprite discharges	11
1.5	Early/fast VLF events and lightning-induced ionospheric disturbances	14
2.1	2D and 3D models coordinate systems	24
2.2	Ambient electron density and conductivity profiles	26
2.3	Nonlinear reactions of electrons due to an external electric field	29
2.4	Dipole model of geomagnetic field	31
2.5	Domain decomposition and computer architecture	34
3.1	3D coordinate system	45
3.2	Thundercloud electrostatic fields in mesosphere	48
3.3	Lateral shifts of thundercloud electrostatic fields in mesosphere	50
4.1	VLF transmitter signal perturbation from quiescent heating of ionosphere	59
4.2	Electron collision frequency change as mechanism of Early/Fast VLF events	63
5.1	Lightning quasi-electrostatic fields at low latitudes	71
5.2	Sprites in the presence of gravity waves	75
6.1	Schematic model of charge distribution within a supercell thunderstorm	80
6.2	Probabilistic model of lightning leaders propagation	83

6.3	Thunderstorm electrodynamic model integration	84
6.4	Lightning simulation in a dipole thundercloud field	86
6.5	Thunderstorm electrodynamics and lightning activity	87
6.6	Lightning evolution	88

Chapter 1

Introduction

The main scientific motivation of this study is to model the thunderstorm electro-dynamics and lightning activity and their resulting upward coupling. Thunderstorms can significantly disturb the electrical environment at distances of hundreds of kilometers away both horizontally and vertically through their strong electrostatic and electromagnetic fields. Benjamin Franklin's famous kite experiment in 1752 was among the first observations of these strong fields and their connection with damaging and destructive lightning discharges. By studying the electrical structure of thunderstorms we gain access to a tremendous knowledge base that can be used to help us protect human lives and important technological infrastructure from the destructive force of lightning and thunderstorms. Today, however, despite over a century of efforts in studying thunderstorm electrical activity and lightning discharges, our understanding of these phenomena remains very limited. *In-situ* observations remain difficult due to the dangerous and hostile nature of thunderstorms for instrumentations, sensors, aircraft and other carrier of sensors. Remote sensing and physical modeling of the various related phenomena, have thus been largely used to improve our understanding in this field. In this dissertation we have developed new models of thunderstorms electro-dynamics that can simulate phenomena with various temporal and spatial scales. We discuss the predictions obtained from the models and validate them against experimental observations and discuss new insights obtained from the developed models. This chapter briefly introduces the necessary background and

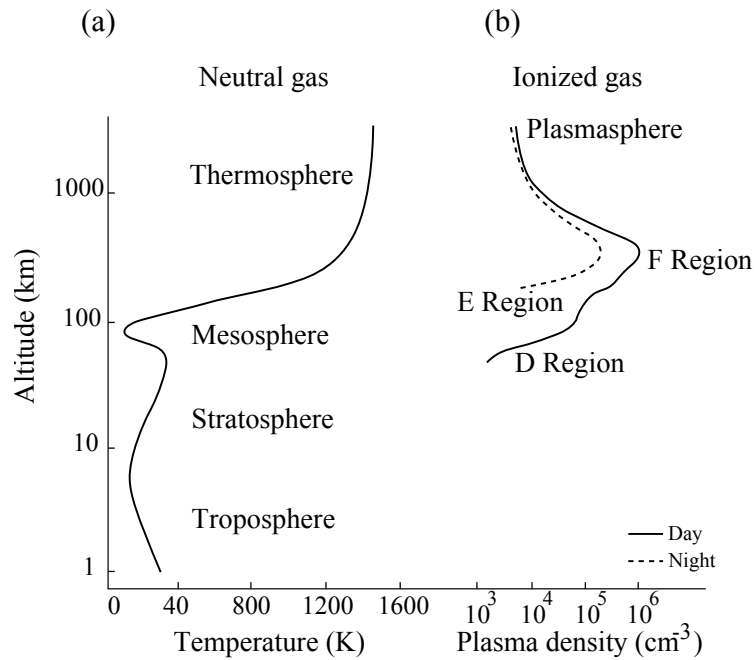


Figure 1.1: Earth's atmospheric temperature and electron density profile (adapted with modifications from [Kelley \[2009\]](#) Fig. 1.1).

concepts that are further explained in detail in later chapters.

1.1 The Earth Electrical Environment

The Earth's atmosphere is composed of various molecules and atoms creating a complex, non-linear, and dynamic system which interacts and evolves through space and time. The interplay between solar radiation absorption efficiency, density changes with altitude, chemical reactions and energy exchange between various atmospheric constituents, and atmospheric convection and advection patterns creates a temperature profile as shown in Figure 1.1a with different regions defined based on temperature gradients [[Kelley, 2009](#), p. 4–5]. Among these atmospheric regions we focus on two that are relevant to this study, namely the **troposphere** and the **mesosphere**.

The troposphere is defined as the atmospheric region between the ground and the reversal point in the temperature gradient which usually occurs at 10–12 km

above the ground. Troposphere hosts weather and storms and includes the altitude range of commercial airplanes. The mesosphere is the region from ~ 50 – 85 km above the ground where the atmospheric temperature decreases with altitude and reaches its minimum at the upper limit of the region called the mesopause. Mesosphere is the region in which most of the thunderstorm electrodynamic upward coupling, as explained in the next chapters, takes place. The details of the physics and chemistry of this region is very poorly understood, partly because of the difficulties involved in accessing it, due to the fact that the region is too high for balloons and airplanes to ascend and too low for satellites to descend. Short but extremely valuable data sets from sounding rockets experiments are the only means of *in-situ* measurements in this region. Remote sensing and modeling are extensively used to understand the mesosphere properties and its role in the interactions between neutral atmosphere and the electrically conductive upper atmosphere.

Due to the absorption of solar energetic radiation mostly in the ultraviolet (UV) and extreme ultraviolet (EUV) spectrum, the day-side Earth's upper atmosphere is constantly ionized. The ionizing radiation of the sun creates a pool of free electrons in the atmosphere. At lower altitudes these electrons frequently collide and recombine with neutrals and other ions and thus are neutralized. At higher altitudes, however, due to the lower neutral density, the electrons remain free and create a highly conductive gas of electrons and ions in the so-called **plasma** state. This plasma layer above the Earth is called the **ionosphere**. Figure 1.1b shows the vertical electric structure of the Earth's atmosphere. The ionosphere characterized by large electron density starts from ~ 60 km and extends up to ~ 1000 km in altitude. Several ionospheric layers are defined based on the altitude dependent electron density profile as *D*-region (60–90 km), *E*-region (90–150 km), *F*-region (150–500 km), and topside region (500–1000 km) [*Kelley, 2009*, p. 6].

The ionosphere extends farther out from the Earth where the recombination and electron-neutral collision rates drop significantly. At even higher altitudes above ~ 1000 km plasma around the Earth is dominantly controlled by the Earth's strong magnetic field which originates from deep inside the Earth. This region of the upper atmosphere constitutes a large bubble around the Earth called the **magnetosphere**.

The magnetosphere is the region where the motion of the charged particles are governed mostly by the magnetic field of the Earth. The ionospheric plasma is further mixed with the charged particles which originate from the sun, travel toward the Earth, enter the magnetosphere and are trapped by in the geomagnetic field.

The neutral particles at ionospheric heights are still the major constituent of the region and significantly affect the environment through collisions with charged particles. The relatively low conductivity of the mesosphere (compared to the ionosphere of higher altitudes) allows the electric fields generated by thunderstorm and lightning in the troposphere to penetrate and affect this ionospheric region. The electrostatic fields of thunderstorms can raise the ionospheric plasma temperature via collisional heating. The strong electromagnetic waves generated by lightning can also heat the ionospheric plasma. These fields can significantly modify the lower ionospheric electron density structure via different reactions such as electron ionization, attachment and detachment. The modifications of the ionospheric electron structure can be observed by remote sensing techniques as explained later throughout this dissertation.

Frequently, the electric fields due to lightning at high altitudes become so strong that they might cause secondary discharges and emissions of light in the mesosphere collectively known as transient luminous events (TLEs) and include sprites and halos, elves, blue jets, and gigantic jets. These TLEs are brief and spectacular light structures that can be observed by sensitive low light level cameras from the ground. The interaction between thunderstorms in the lower atmosphere and the overlying ionosphere is generally referred to as thunderstorm electrodynamic upward coupling.

1.2 Thunderstorm Electrodynamics

1.2.1 Cloud Electrification

Thunderclouds are strongly electrified environments capable of producing electric fields of thousands of volts per meter which frequently result in discharges in the form of lightning. The separation of charges in the clouds, also called electrification,

is due to processes that can be classified into two main categories: 1) the microphysical processes involved in the separation of charge particles on a small spatial scale [*Saunders, 2008*, and references therein] and 2) the large-scale mechanisms responsible for creation of large charge layers as observed by in-situ and remote sensing measurements [*Krehbiel et al., 1979*; *Marshall et al., 1995a*; *Stolzenburg et al., 1998a,b*].

The microphysical processes can further be divided into inductive and non-inductive charging. Non-inductive processes act independently from external electric fields and are due to charge exchange between colliding and rebounding particles. Inductive processes, however, can have different outcomes depending on the level and the direction of the electric field in which the particles collide.

There are many proposed mechanisms such as ion charging [*Wilson et al., 1929*], convective charging [*Helsdon et al., 2002*], inductive charging [*Mason, 1988*; *Brooks and Saunders, 1994*], and ice crystal/graupel collisional charging [*Baker et al., 1987*] with various degrees of success in explaining the observed features of a charging thundercloud. It is more likely that in a real thunderstorm several processes work together or are dominant at different phases of the cloud electrification. The non-inductive ice crystal/graupel collisional charging (schematically illustrated in Figure 1.2), however, is believed to be the most dominant charging mechanism currently proposed for cloud electrification [*Baker et al., 1987*; *Dash et al., 2001*]. In this theory, colliding ice particles and rimming graupels which are growing at different diffusional rates exchange charges in such a way that the particle that grows faster charges positively. The growth and sublimation rates of these particles depend on the local temperature and are influenced by local cloud water content [*Takahashi, 1978*; *Jayaratne et al., 1983*]. At some critical temperature, T_c , there is a change of the sign of the charge transferred to a rimming graupel pellet by a separating ice crystal following a collision. Laboratory measurements indicate $T_c \simeq -20$ °C [*Jayaratne et al., 1983*]. In particular, it has been shown that at temperatures warmer than T_c , larger rimming graupel stones become positively charged while the smaller ice crystals are negatively charged. At lower temperatures, the sign of the charged cloud particles is reversed. The larger cloud particles fall under gravity while the smaller ice crystals are carried aloft by the updrafts within the cloud. The temperature dependence of charging mechanisms

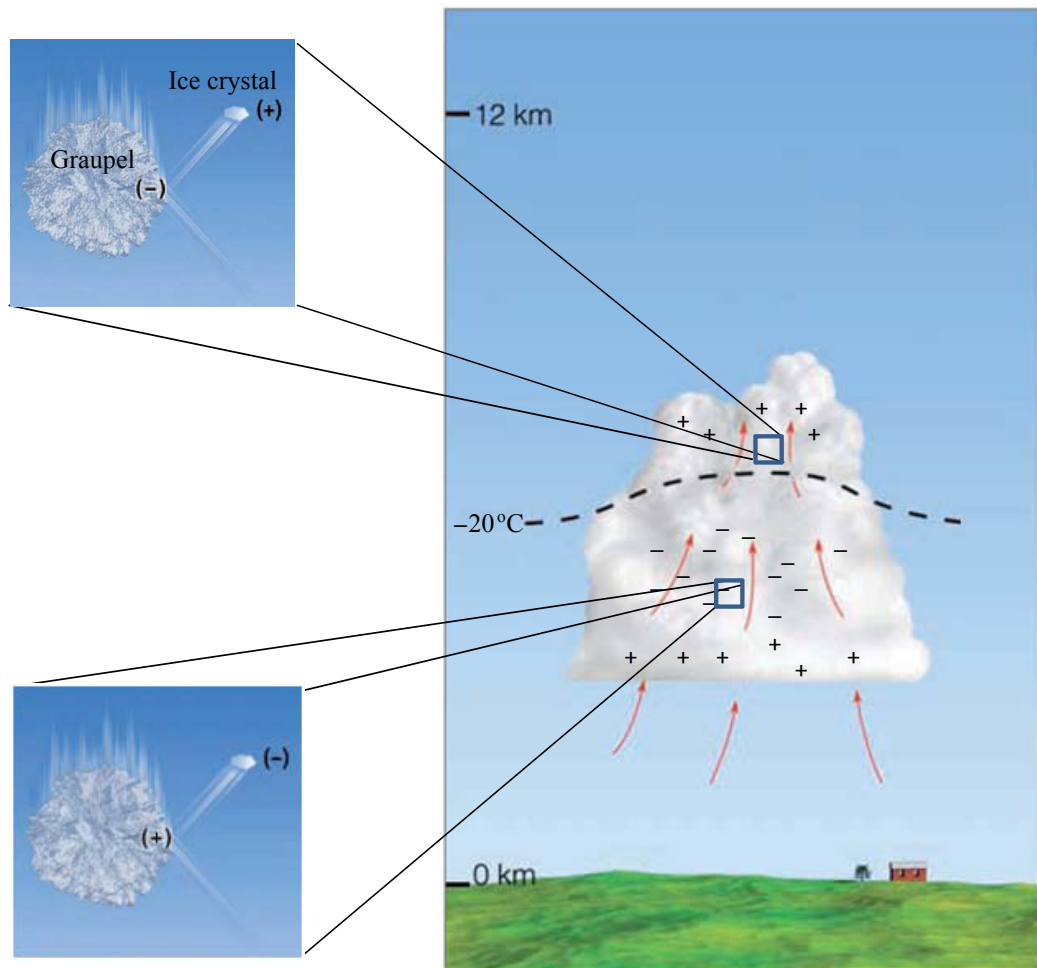


Figure 1.2: Collisional charging of graupels (soft-hail pellets) and ice crystals in a cloud (Adapted with modifications from [Ahrens \[2007, Fig. 14.2\]](#)).

can successfully explain both the dipole charge structure of thunderstorm clouds as reported by [[Wilson, 1916](#); [Wilson et al., 1929](#)] as well as the often observed tripole charge structure [[Williams, 1989](#)].

1.2.2 Lightning

Lightning is a spectacular natural phenomena exhibiting tremendous variety and occurring 40–50 times every second globally [[Christian et al., 2003](#)]. Lightning is an extremely dangerous phenomenon and kills hundreds of people and costs billions of

dollars of damage in United States and much more globally every year [*Rakov and Uman, 2003*, Ch. 18]. Lightning fatalities have been significantly higher than tornado, flood, or hurricane fatalities from 1940s up until 2000 except in 4 years with significant hurricane deaths. On average, every airplane is struck by lightning once or twice per year, with potential damage to the airplane and its components [*Sweers et al., 2004*].

Phenomenologically, lightning discharges are very diverse, but can be categorized into three main types [*Rakov and Uman, 2003*, p. 4]. The intra-cloud (IC) lightning discharges are the most common type of the lightning discharges ($\sim 75\%$ of the total) that initiate and remain within the cloud. The remaining discharges (about 25%) are cloud-to-ground (CG). The negative cloud-to-ground ($-CG$) discharges remove negative charge from the cloud to the ground and make up more than 90% of all cloud-to-ground discharges. Positive cloud-to-ground ($+CG$) discharges connect to the ground and destroy the positive charge inside the cloud. $+CG$ s are the least common type of the three main lightning categories but are often the most powerful type of lightning discharges, removing large amount of charge from the cloud and causing intense upward electrodynamic coupling.

Most of our current understanding of lightning discharges comes from studies of CG discharges. Most CG discharges start from a region with intense electric field within the cloud. The negative CGs propagate in a stepped-leader process and branch frequently in many directions until one of the branches connects (attaches) to the ground. The positive CGs reach the ground in the similar manner, although the details of the leader process are somewhat different. At this moment, a highly conductive channel, called the lightning channel, is formed, which serves as a suitable path for the stored electrostatic energy within the cloud to the ground. A large electrical current, called the return stroke, propagates upward toward the cloud through which the cloud discharges. Lightning activity does not terminate with the return stroke but usually continues with another downward leader channel, the dart leader, propagating within the previous channel and initiating one or several subsequent return strokes.

In addition to optical emissions from the lightning channels and strong shock and acoustic waves generated, lightning discharges emit strong electromagnetic radio

waves, in the frequency range from a few Hz up to ~ 10 GHz [Rakov and Uman, 2003, p. 6]. Observations of this radiated electromagnetic power has been used as a remote sensing tool for lightning activity and lightning physics. Most of the emitted waves are in the Very Low Frequency (VLF) range (3–30 kHz). These waves are efficiently reflected by the ionosphere and can propagate to large distances in the Earth-ionosphere waveguide. Triangulation techniques, can thus be used for accurate geolocation of lightning discharges around the globe [Said *et al.*, 2010, and references therein]. Signatures of the radiated VLF waves called “radio atmospherics” or “sferics” can be used to estimate the source lightning currents. Positive CGs are often followed by intense continuing currents that can last for hundreds of milliseconds and radiate in the Extremely Low Frequency (ELF) range [Bell *et al.*, 1998]. The ELF spectrum of the radiated waves can be used to estimate the charge moment change caused by lightning and therefore the amount of charge removed from the cloud [Cummer and Inan, 1997].

1.2.3 Transient Luminous Events as Evidence of Thunderstorms Upward Electrodynamic Coupling

Over the last several decades many observations have improved our understanding of thunderstorm upward electrodynamic coupling. Many of these observations have used various optical instruments and techniques such as low-light sensitive cameras, photometers, and spectroscopy [Sentman *et al.*, 1995; Wescott *et al.*, 1995; Mende *et al.*, 1995; Hampton *et al.*, 1996; Winckler *et al.*, 1996; Fukunishi *et al.*, 1996]. The optical signatures studied are often short in time and are thus collectively termed as transient luminous events or TLEs. The most prominent of these events are sprites, halos, elves, blue jets, and gigantic jets as schematically shown in Figure 1.3 with their occurrence altitude range.

An elves event, first observed from the Space Shuttle [Boeck *et al.*, 1992] and later by ground instruments [Fukunishi *et al.*, 1996], is an expanding ring of light [Inan *et al.*, 1997] typically occurring about 90 km above the ground. It is caused by the electromagnetic pulse (EMP) generated from a cloud-to-ground lightning strike

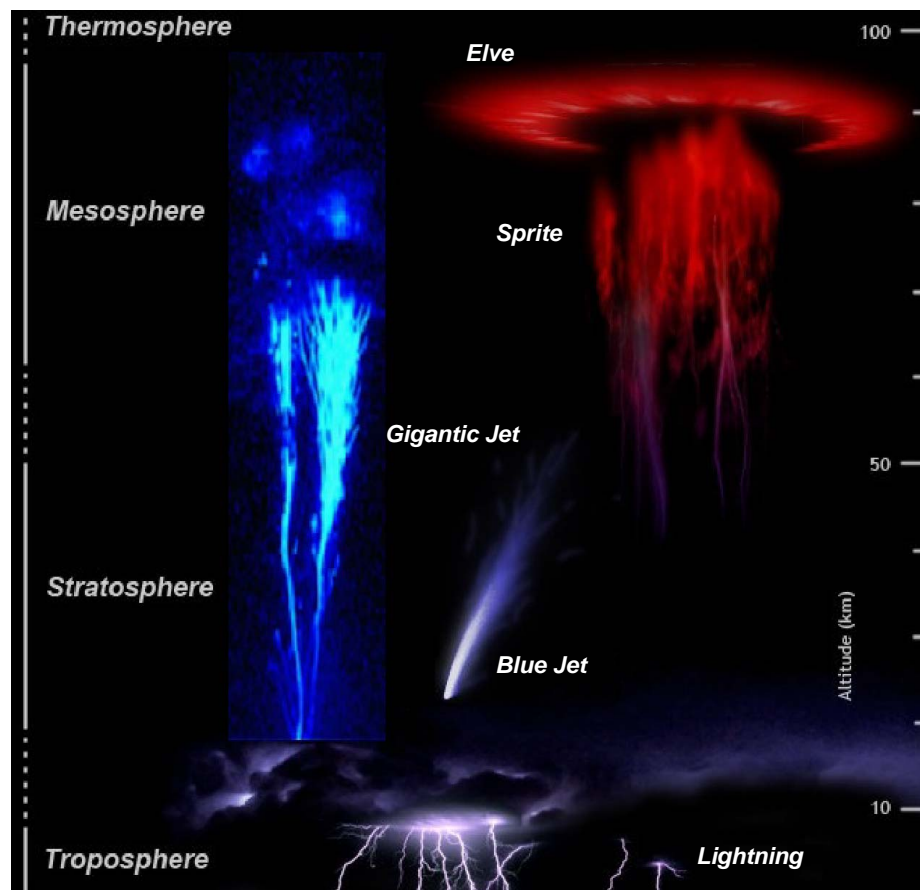


Figure 1.3: Transient Luminous Events observed above thunderstorms (Adapted with modifications from https://en.wikipedia.org/wiki/Upper-atmospheric_lightning).

and were first theoretically predicted by *Inan et al.* [1991]. The EMP generated by lightning propagates upward with a radiation pattern similar to a vertical antenna. The electric field of the pulse heats the electrons in the lowest layer of ionosphere (*D*-region). The accelerated electrons excite the higher energy levels of atmospheric constituents, which leads to emission of light [*Taranenko et al.*, 1993a]. In addition to the heating of the ionosphere, elves can cause appreciable changes in local electron density of *D*-region ionosphere through impact ionization and dissociative attachment reactions of the heated electrons [*Mende et al.*, 2005] (see Equations 2.11–2.13).

Another important type of TLEs are sprites and halos [*Sentman et al.*, 1995].

Sprites were first serendipitously observed during the testing of a sensitive low-light level camera by *Franz et al.* [1990]. These events are due to intense heating and ionization of the ionospheric plasma by a strong CG discharge [*Pasko et al.*, 1995]. After their discovery, they have been observed from the Space Shuttle [e.g., *Yair et al.*, 2004], from Earth orbiting satellites [e.g., *Mende et al.*, 2005], and from aircraft and ground stations extensively [*Sentman et al.*, 1995; *Mende et al.*, 1995; *Lyons et al.*, 1996, etc.].

High-resolution telescopic imaging of sprites unambiguously identified them as collections of filamentary streamer discharges elongated in altitude [*Gerken et al.*, 2000; *Gerken and Inan*, 2002]. Each steamer channel was measured to be about a few kilometer long in the vertical direction and a 150–200 m in diameter depending on the altitude of the measured width. Sprite steamers are typically initiated at an altitude of ~ 75 km and propagate downward. Sometimes the streamer discharges are associated with a diffuse glow of light at higher altitudes (~ 85 – 90 km) called “sprite halos” or “halos” [*Barrington-Leigh et al.*, 2001]. *Barrington-Leigh et al.* [2001], with a combination of optical measurements and numerical modeling, conclusively identified the sprite halos to be due to the strong quasi-electrostatic fields of lightning discharges confirming the previous predictions by *Pasko et al.* [1995, 1997a].

Figure 1.4 shows the mechanism postulated by *Pasko et al.* [1997a] to explain sprite emissions due to the quasi-electrostatic heating of the lower ionosphere. Based on this theory, the quasi-electrostatic fields developed over minutes during the accumulation of charges in a thundercloud, are screened from the higher altitudes by the conducting upper atmosphere via relatively slow charge redistributions. After the sudden removal of the thundercloud charges by a lightning discharge, because the response time of the *D*-region of the ionosphere is longer compared to the charge removal time scale, very strong quasi-electrostatic fields are created in that region which exceed the local breakdown field and lead to a secondary discharge in the lower ionosphere until the medium responds to screen the field via charge redistribution over time scales of tens of milliseconds.

This mechanism was first noted by *Wilson* [1924]: “The electric force due to a cloud of electric moment M , at a point vertically above it in the upper atmosphere,

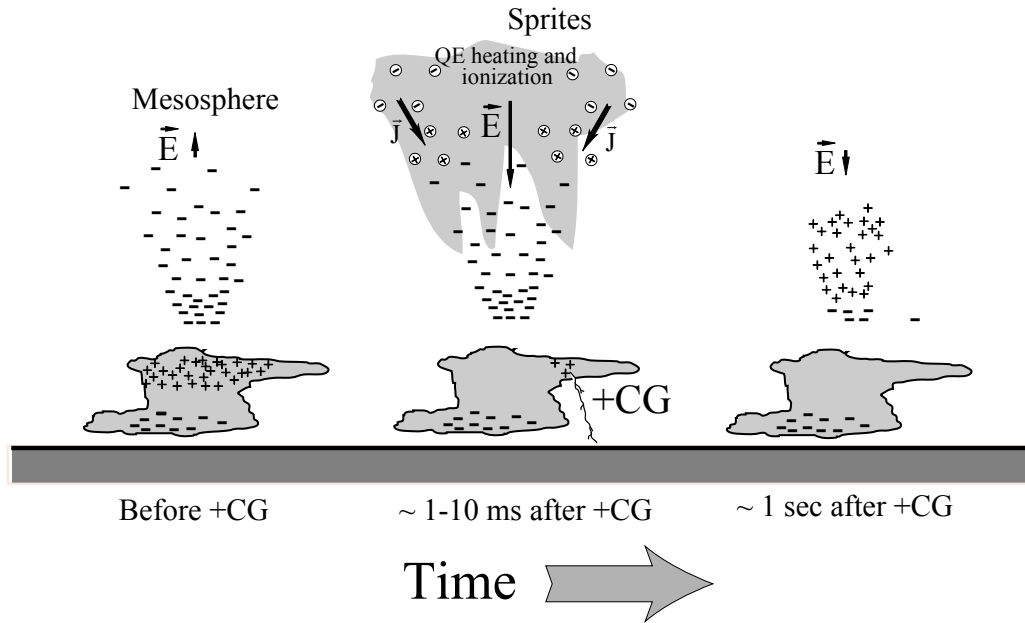


Figure 1.4: Schematic mechanism of sprite discharges (adapted from [Pasko et al. \[1997a\]](#) with modifications).

may be taken as approximately $2M/r^3$, where r is the height of the point above the ground. While the electric force due to the thundercloud falls off rapidly as r increases, the electric force required to cause sparking (which for a given composition of the air is proportional to its density) falls off still more rapidly. Thus, if the electric moment of a cloud is not too small, there will be a height above which the electric force due to the cloud exceeds the sparking limit”.

Another class of TLEs are blue jets which are columnar regions of blue light initiating from the cloud tops and expanding upward to $\sim 40\text{--}50$ km in altitude [[Wescott et al., 1995](#)]. Unlike sprites and elves, blue jets are not initiated due to a lightning discharge but are initiated close to the upper boundary of the thundercloud during the slow accumulation of a large amount of charge at altitudes ~ 20 km [[Pasko et al., 1996](#)]. Due to the severe scattering of the blue light in the atmosphere, these events are harder to observe from ground stations and often require airborne platforms. Even before their video observations, there had been reports of these events seen by naked eye as a “diffuse fan-shaped flashes of greenish colour extending up into a clear sky”

by *Wilson* [1956] in which he also provided an explanation for the possibility of such a discharge.

A more recently discovered category of TLEs are the gigantic jets. These events similar to blue jets start from the cloud tops but expand all the way to the lower ionosphere and connect the thunderclouds directly to the ionospheric regions [*Pasko et al.*, 2002; *Su et al.*, 2003]. Gigantic jets are a very rare phenomena and have been exclusively observed over large thunderstorms. These events have not yet been associated with any lightning type and existing models have failed to explain many of their fundamental features. Experimental and modeling studies of gigantic jets as well as their importance in the Earth global electric circuit are still active areas of research [*Krehbiel et al.*, 2008; *Cummer et al.*, 2009; *Lu et al.*, 2011; *Silva and Pasko*, 2013].

1.2.4 VLF Events as Evidence of Thunderstorms-Ionosphere Coupling

Efficient propagation of VLF signals in the Earth-ionosphere waveguide, combined with their ability to penetrate sea water, make this part of the electromagnetic spectrum suitable for long-range and submarine communications. Many VLF transmitters have been operated as Naval communication systems by the United States other countries for deep sea communication and pre-GPS navigation systems. Such VLF waves reflect from the lower ionospheric *D* region at different altitudes during the day and night.

The amplitude and phase of the received signal on the ground is a sensitive function of the ionosphere state along the signal path. *Helliwell et al.* [1973] were among the first who noticed and studied these modifications. They observed both increases and decreases of up to 2 dB signal amplitude perturbations associated with lightning generated whistler waves. To explain the observations they suggested a theoretical mechanism by which lightning-generated whistler waves pitch-angle scatter energetic magnetospheric electrons (30–300 keV) and cause their precipitation into the *D*-region ionosphere. These events, also sometimes referred to as Trimpi or Lightning-induced

Electron Precipitation (LEP) events, were later observed and studied by many others from ground-based VLF receivers [*Leyser et al., 1984; Inan et al., 1985; Inan and Carpenter, 1986; Carpenter and Inan, 1987; Peter, 2007*, and references therein], and with satellite and rocket observations of the precipitating electrons is association with whistlers [*Voss et al., 1984; Goldberg et al., 1986; Inan et al., 2007*].

LEP events have a $\sim 0.6\text{--}1$ s delay following the causative lightning, consistent with the propagation time of the whistler waves and bounce period of precipitating electrons [*Inan et al., 1988; Inan and Rodriguez, 1993*]. They show a decrease in the VLF signal amplitude consistent with electron precipitation which brings the ionospheric height to lower altitudes. The amplitude-phase perturbation of VLF transmitter signals can be described by a ~ 1 second rise time which is controlled by the source of the ionospheric perturbation and the whistler wave dispersion in the magnetosphere and a slower recovery time (~ 30 seconds) controlled by the equilibrium dynamics of the electron population.

Another type of lightning energy coupling to the lower ionosphere was first reported as a VLF perturbation event which showed a sudden increase of the VLF signal amplitude (< 20 ms) implying a direct effect of the lightning on the ionosphere [*Armstrong, 1983*]. The event was associated with strong ELF emissions due to the continuing currents and with a whistler which arrived later. This type of VLF perturbations came to be called the “Early/Fast” events, because the following observations characterized them as “Early” by a short delay from the causative lightning discharge (< 20 ms, constrained by 50 Hz sampling rate of the classification techniques) and “Fast” with a short rise time (< 20 ms). Most of the observations of Early/Fast events show positive step-like features in the signal amplitude as shown, for example, in Figure 1.5c [*Inan et al., 1988, 1993*], suggesting a sharpening of electron density profile by increased attachment/ionization below/above ~ 85 km [*Taranenko et al., 1993b*] which makes the Earth-ionosphere waveguide a better reflector of waveguide modes with resultant less absorption for the VLF signal along its path.

Figure 1.5a,b shows a sketch of strong lightning upward electrodynamic coupling sometimes manifested as sprites and/or elves which sometimes also creates a conductivity disturbance that can scatter subionospherically propagating VLF transmitter

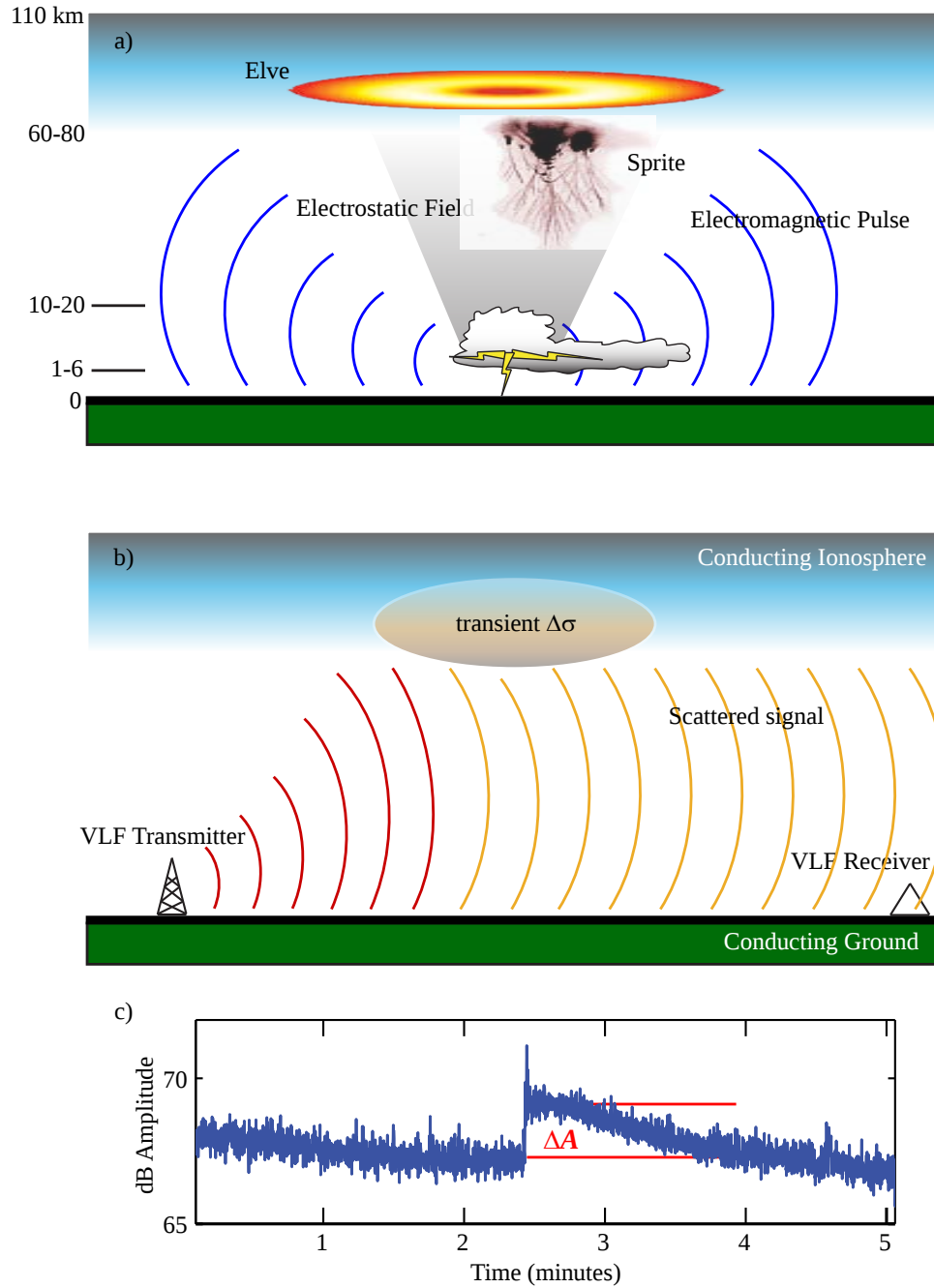


Figure 1.5: Schematic mechanism of Early/Fast VLF events due to the ionospheric disturbance created by a lightning discharge (adapted from [Marshall \[2009\]](#)).

signals and cause Early/Fast events, an example of which is shown in Figure 1.5c. Generally, a larger transverse size of the conductivity perturbation creates larger amplitude changes of the VLF signal [Inan *et al.*, 1996a]. Johnson *et al.* [1999] studied the scattering pattern of the lightning-induced ionospheric disturbances associated with Early/Fast VLF events using an array of VLF receivers. Their analysis suggested a rather narrow perturbation beam which indicates a disturbance size of 90 ± 30 km across. This information was determined by studying the transmitter-receiver signal path with respect to the location of the causative lightning discharge. A larger disturbance size would intercept the transmitter signal on more transmitter-receiver signal paths.

The conductivity perturbations of the lower ionosphere may be due to the electron mobility changes, electron density changes, or a combination of both effects. Despite many years of investigations, however, the exact mechanism responsible for the conductivity perturbations in the ionosphere that cause Early/Fast VLF events is still under debate. The vast number of parameters involved in the observations and the many unknowns in the ionospheric conditions along the long VLF signal propagation path has rendered most of the theoretical studies of the physical mechanism of Early/Fast events inconclusive.

Association of many of the Early/Fast and sprite observations [Inan *et al.*, 1995; Haldoupis *et al.*, 2004; Mika *et al.*, 2005] was used by Barrington-Leigh *et al.* [2001] to suggest that the Early/Fast events are created by the electron density changes associated with sprite halos. Moore *et al.* [2003], using a full-wave electromagnetic model of sprite halos combined with a VLF propagation model, calculated the signal perturbation amplitude of Early/Fast events from sprite halo plasma. The results were consistent with the observations within a factor of seven for the peak currents of the causative lightning, as reported by National Lightning Detection Network (NLDN). The continuing currents were argued to be the source of the discrepancy between NLDN reported peak current and the simulation results. However, the sprite halo mechanism requires a cloud-to-ground lightning which is not consistent with Inan *et al.* [1988] observations indicating that only about half of the observed Early/Fast VLF events were associated with CG flashes but that $\sim 98\%$ of them were associated

with sferics. IC discharges can thus be as important as CG discharges for ionospheric modifications since horizontal flashes from IC discharges radiate more efficiently upward. *Mika et al.* [2006] reported VLF perturbations similar to Early/Fast events but associated with elves based on ground and satellite observations. On average, the transmitter signal perturbations had a ~ 2 minute relaxation time which is consistent with an electron density change at higher altitudes associated with elves.

Marshall et al. [2008] calculated the cumulative effects of the lightning EMP-driven dissociative attachment caused by multiple consecutive pulses. The authors argued that Early/Fast events should be mostly positive changes in amplitude, due to lower absorption in the density depleted region, consistent with observations. However, their model did not show positive amplitude perturbations to be as frequent as observations suggest, but indicated the sign and magnitude of the perturbation depends largely on the transmitter, disturbance and receiver locations.

Haldoupis et al. [2006] reported on a new category of VLF events that were observed early (< 20 ms after the discharge) but showed a slow onset of 1–1.5 s. The events were associated with sprites and usually consisted of a post-onset sequence of CG discharges coming from the same area and a large number of weaker but densely-clustered sferics, most likely ICs in the same area. These events, termed as “Early/Slow”, were proposed to be due to secondary ionization buildup from successive CG and IC discharges which may increase the overall conductivity, despite the decreased mobility (due to enhanced collisions) of the heated primary electrons.

Another type of VLF events as evidence of lightning energy coupling to the lower ionosphere can be found in the observations of *Dowden et al.* [1994] and *Inan et al.* [1996a], called Rapid-Onset-Rapid-Decay (RORD). The VLF signal signatures for these events were typically similar to Early/Fast events but had a very short recovery time of only 1–2 s as opposed to tens of seconds as in the Early/Fast events. The fast recovery events were postulated to be due to electron heating of the lower ionosphere, where the electron temperature remains below the threshold of dissociative attachment of electrons. For these cases, no significant electron density changes occur and the conductivity changes due to increased electron temperature last only as long as the driving fields, typically less than a few seconds. The events are only detected

when the causative CG is within 50 km of the transmitter-receiver path and thus are signatures of a localized perturbation. However, not all CG flashes within 50 km off the signal path produced VLF or LF perturbations.

The observed Early/Fast events show vast range of recovery times [*Inan et al.*, 1993; *Sampath et al.*, 2000; *Mika et al.*, 2005; *Cotts and Inan*, 2007] and may be associated even with weak lightning discharges (as opposed to the LEP events that are mostly observed following strong +CG discharges). *Inan et al.* [1996b] proposed the sustained heating of the ionosphere as the driving mechanism for the Early/Fast observations. Based on this theory, the difference between the quiescent heating level of the ionosphere (maintained by the totality of the thunderstorm) before and after individual discharges can cause the VLF signal perturbation, with the recovery of the signal basically representing the recharging of the cloud. The observed “post-onset” peaks in the Early/Fast events [*Inan et al.*, 1996a] could be explained by the transient but intense heating of the ionosphere due to the discharge. However, *Inan et al.* [1996a] found that the estimated perturbation in signal amplitude was very small (0.01–0.1 dB) compared to the observations of the Early/Fast events of 0.2–1.7 dB with most of the events in 0.2–0.8 dB range [*Inan et al.*, 1988, 1993, 1996a]. The insufficient estimated amplitude changes have been used to rule out the sustained heating theory as a mechanism of Early/Fast events [*Moore et al.*, 2003; *Haldoupis et al.*, 2006]. In Chapter 4 we re-consider the sustained heating model of *Inan et al.* [1996b] with the inclusion of a realistic geomagnetic field in the model and show that with the improved model the estimated perturbation levels are well consistent with the Early/Fast observations.

1.3 Thesis Organization

In this introductory chapter we reviewed some of the previous theoretical and experimental work relevant to the development and the results presented in the rest of this dissertation. The brief introduction of the general electrical structure of the Earth’s lower atmosphere and the ionosphere is provided in Section 1.1. Some fundamental concepts of thunderstorm electrodynamics and lightning as well as several

different types of evidence of the thunderstorm direct upward coupling to the mesosphere/ionosphere regions are discussed in Section 1.2. The organization and the scientific contribution of this dissertation is summarized in Sections 1.3 and 1.4.

Chapter 2 describes the construction of the models developed for this dissertation in Section 2.1–2.5 along with the computational improvements of the new model by using parallel techniques and novel numerical schemes as explained in Sections 2.6 and 2.7.

The rest of the dissertation is designated for the applications of the model. The quasi-static fields of thunderclouds, corresponding to the charge accumulations inside the thunderclouds, are considered in Chapter 3. The effects of a realistic geomagnetic field, which was neglected by all previous studies, are taken into account and the new findings of the model associated with the upward electrodynamic coupling of thunderstorms are discussed. Chapter 4 considers the implications of the model on our current understanding of the source mechanism of Early/Fast events by revisiting the sustained heating model introduced in Section 1.2.4.

We continue our discussion of the high altitude applications of the model in Chapter 5, where some of the other capabilities of the model are demonstrated. Particularly, we put emphasis on the 3D model applications that were impossible for the previous 2D models, such as the effects of geomagnetic field and the presence of elongated gravity wave fronts in the ionosphere on the quasi-electrostatic fields and heating in the lower ionosphere.

Chapter 6 illustrates the low-altitude applications of the model, particularly the thunderstorm electrodynamic evolution and the lightning activity. We comment on the new findings of the model and propose and discuss a new mechanism for generation of cloud-to-ground lightning from a dipole charge structure in a thunderstorm.

Finally, we summarize our findings in Chapter 7 and give some suggestions for future work.

1.4 Scientific Contributions

The purpose of this PhD dissertation was to develop the first parallel 3D model of thunderstorm electrodynamics and upward coupling processes. The scientific contributions of this study are presented in Chapters 3–6 and are summarized here:

1. Developed a parallel 2D and the first parallel 3D and self-consistent model of the nonlinear upward coupling of quasi-electrostatic thundercloud fields;
2. Predicted an eastward and equatorial shift in the high-altitude electric fields created by thunderclouds;
3. By including the geomagnetic field direction, demonstrated that thundercloud electric field intensities in the mesosphere were until now underestimated;
4. Constructed a full thunderstorm development model by integrating a thundercloud charging model, the quasi-electrostatic model and a time domain lightning fractal model;
5. Simulated long-timescale thunderstorm development and reproduced IC to CG evolution of thundercloud discharges; and
6. Proposed a new mechanism for development of cloud-to-ground lightning from dipolar charge layers.

Chapter 2

Model Formulation

In this chapter, we describe our model formulation and implementation. The models developed are a parallel 2D and a parallel 3D model of thunderstorm electrodynamics and upward coupling and the interaction of thunderstorm and lightning quasi-electrostatic fields with the mesosphere and the ionosphere. The parallel 2D model extends the model of *Pasko* [1996]; *Pasko et al.* [1997a, 1995] and takes advantage of large computer clusters by reducing the computation time and gives us the ability to obtain solutions with much higher spatial resolution than previously possible. The parallel 3D model extends the parallel 2D model by relaxing the assumption of azimuthal symmetry and is thus capable of including any realistic charge distributions, geomagnetic field, ambient atmospheric and ionospheric profiles, and lightning activity evolution. In later chapters we show some applications of these models for specific studies.

2.1 Thundercloud Charging Model

Thundercloud evolution is a complicated phenomenon for numerical simulation due to the vast time and spatial scales associated with the physical mechanisms involved. A physically-accurate numerical cloud model to simulate thundercloud charging should include many of the physical phenomena involved, such as bulk microphysics, separate categories for cloud water, ice, rain, snow aggregates, hail stones, and frozen

drops and various charge separation mechanisms such as convective, inductive, and collisional charging [Ziegler *et al.*, 1986; Mansell, 2000; Mansell *et al.*, 2005]. These models are extremely complicated and computationally expensive and thus can only be used in limited cases. However, combined with data provided by observational techniques using radar, rocket, and balloon measurements of electric fields and radio remote sensing of the electromagnetic radiation from lightning discharges, such models have given us an estimate of the charge distributions and evolutions inside the cloud [Taylor, 1978; Marshall *et al.*, 1995a,b; Cummer and Inan, 1997; Stolzenburg and Marshall, 2008].

The upward electrodynamic coupling of thunderstorms, manifested as physical phenomena in the mesosphere, is not sensitive to the details of the physical processes responsible for cloud charging. This insensitivity allows us a degree of freedom in the formulation of the computational model, so that it does not have to include the unnecessary microphysical phenomena which would make the computation much more complicated. The simplified formulation and its justification are explained in detail in Section 2.2. In order to be able to interpret the results of our numerical model for the upward coupling of thunderstorms, we purposely choose to use a simple model of thundercloud charges and ignore the details of creation of the charges and their distribution within the cloud.

The evolution of the charges is assumed to be a known function of time that can be chosen before the start of the simulations. For example, we can choose a linear function for the charge accumulation phase of the storm and a linear or exponential function for the removal of the charge during a lightning discharge. In the 2D model we assume a symmetric dipole or a monopole charge structure located on the axis of symmetry. The charge densities are taken to be distributed with a Gaussian profile as:

$$\rho_{\pm}(\vec{r}, z) = \rho_0 \exp \left[- \left(\frac{r^2}{a_{\pm}^2} + \frac{(z - z_{\pm})^2}{b_{\pm}^2} \right) \right]$$

where z_{\pm} represents the height of the charges and a_{\pm} and b_{\pm} determine the sizes of the charges in the horizontal and vertical dimensions respectively. The charge densities are normalized by the total amount of charge in each layer of the cloud,

$Q_{\pm}(t) = \int \rho_{\pm}(\vec{r}, t) dV$. In the 3D model there is no need to assume a symmetric charge distribution. The charge distribution can be obtained from observations of the cloud or from the more complicated charging models and be used as an input into the 3D model. In many cases, in this and the following chapters however, we represent the charge layers in the cloud by a Gaussian-distributed charge profile as:

$$\rho_{\pm}(x, y, z) = \rho_0 \exp \left[- \left(\frac{(x - x_{\pm})^2}{a_{\pm}^2} + \frac{(y - y_{\pm})^2}{b_{\pm}^2} + \frac{(z - z_{\pm})^2}{c_{\pm}^2} \right) \right]$$

where $(x_{\pm}, y_{\pm}, z_{\pm})$ is the location of the charge center and a_{\pm} , b_{\pm} , and c_{\pm} are the sizes of the distribution in x , y , and z directions respectively. An even more complicated charge structure in the cloud may be represented in our code by a suitable collection of charge pockets each having a separate Gaussian (or other) distribution.

For low-altitude applications of the model, such as the study of lightning activity and thunderstorm electrical environment discussed in Chapter 6, we are particularly interested in the evolution of the charging and discharging mechanisms during the lifetime of a thunderstorm. Therefore, we need to use a different model of thunderstorm charging and discharging which includes more physics and which can provide insight about the dominant mechanisms that control the temporal and spatial distributions of lightning activity and charge structure within the cloud. We revisit this topic in Chapter 6 and reformulate our model for the application at low altitudes.

2.2 Calculation of Quasi-electrostatic Fields

The quasi-electrostatic (QE) fields are generated in the atmosphere and the mesosphere by accumulation of charges within the thundercloud and by their removal from the cloud during the lightning discharges. These fields last over a very long time and change very slowly and can be treated using quasi-electrostatic formulation of Maxwell's equations (i.e., the electromagnetic wave propagation is not considered and the speed of light is taken to be $c \rightarrow \infty$). We use the formulation of *Pasko* [1996]; *Pasko et al.* [1997a] which ignores the higher-frequency content of the electromagnetic waves radiated by the return stroke of lightning discharge. This formulation has been

shown to produce a very good estimate of quasi-electrostatic fields when compared to the solution of the full set of Maxwell's equations [*Baginski and Hodel, 1994*]. The effects of the magnetic fields, which are generated by the currents associated with the thundercloud charging and temporal variation of quasi-electrostatic fields, are ignored as they are at least two orders of magnitude smaller than the Earth's background geomagnetic field [*Pasko, 1996, Ch. 2*]. The electric fields, $\vec{E} = -\nabla\Phi$, are calculated using the following quasi-static equations:

$$\frac{\partial(\rho + \rho_s)}{\partial t} + \nabla \cdot (\vec{J} + \vec{J}_s) = 0 \quad (2.1)$$

$$\nabla \cdot \vec{E} = (\rho + \rho_s) / \epsilon_0 \quad (2.2)$$

where ρ_s and \vec{J}_s represent the thundercloud source charge and current density and ρ and \vec{J} represent the atmospheric charge and current density induced by the thundercloud charges. As mentioned in Section 2.1, for high-altitude applications of the model, we can use a known function for the temporal and spatial evolution of the thundercloud charge density. The use of a known function simplifies the continuity equation (2.1) as follows:

$$\frac{\partial\rho}{\partial t} + \nabla \cdot (\hat{\sigma}\vec{E}) - \rho_s\sigma_{\parallel}/\epsilon_0 = 0 \quad (2.3)$$

where we used $\vec{J} = \hat{\sigma}\vec{E}$ with $\hat{\sigma}$ being the atmospheric conductivity tensor due to electron and ion contributions, and the relation $\partial\rho_s/\partial t + \nabla \cdot \vec{J}_s = -\rho_s\sigma_{\parallel}/\epsilon_0$ as derived in *Pasko [1996, Ch. 2]*.

In the 2D model we use a cylindrical coordinate system as shown in Figure 2.1 (left) with r representing the horizontal distance from the center of the storm and z representing altitude. The simulation domain in the 3D model is changed to a Cartesian coordinate system (Figure 2.1; right-hand panel) to simplify the implementation of the model. In the 3D model configuration x points to the magnetic east, y points in the magnetic north direction, and z represents altitude and points upward. The ground at the lower boundary of the model is considered to be a perfect conductor (in which we may assume $\Phi = 0$) which is a well justified assumption for the slowly

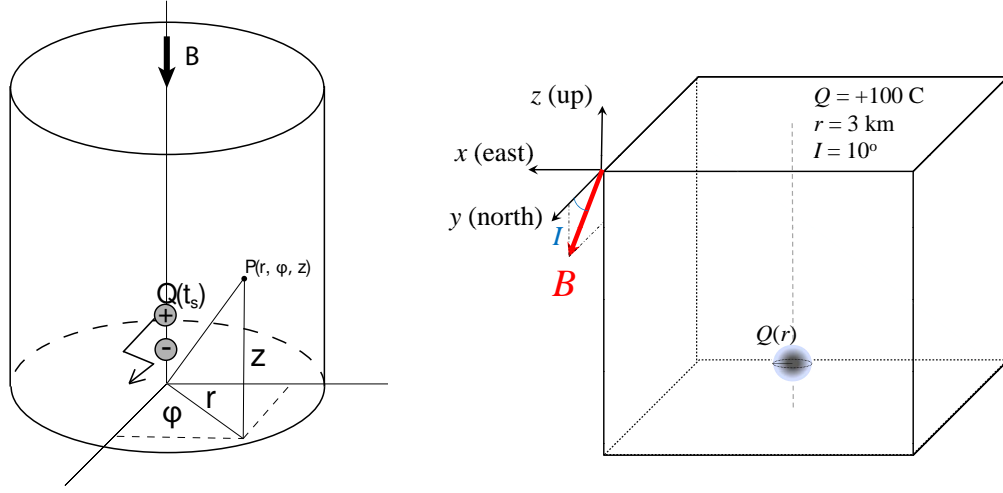


Figure 2.1: Left: 2D model coordinate system (adapted with modifications from [Pasko \[1996\]](#)), right: 3D model coordinate system

changing quasi-electrostatic fields. Either Neumann condition ($\partial\Phi/\partial t=0$) [[Tzur and Roble, 1985](#)] or Dirichlet condition ($\Phi=0$) [[Illingworth, 1972](#)] can be used for the top and side boundaries. These boundary conditions are not physical and introduce an error into our calculations near the boundaries. Such errors can be minimized if the boundaries are located at a farther distance. For example selecting the side boundaries at $r=60$ km introduces $\sim 10\%$ error on magnitude of the electric field at $r=50$ km and $z=10$ km [[Pasko, 1996](#)]. With a farther distance, however, the simulation domain becomes larger, which increases the time for solving the equations. In practice, we should fix the boundaries at a distance with a good trade-off between the accuracy and the computational cost of the model.

With the above setup for boundaries, a given thundercloud charge distribution and initial (ambient) conductivity profile, we can find the electric fields and the induced charges by alternatively solving the Equations 2.2 and 2.3 for the next value in time until the desired time interval of the electric field development has been simulated.

2.3 Ambient Atmosphere and Lower Ionosphere

The conductivity tensor $\hat{\sigma}$ used in Equation 2.3 depends on the ambient electron, ion and neutral profiles as well as the direction and magnitude of the geomagnetic field. In a 3D Cartesian coordinate system with a magnetic field in the yz plane, the tensor conductivity is written as [*Park and Dejnakarindra, 1973*]:

$$\hat{\sigma} = \begin{pmatrix} \sigma_P & \sigma_H S & \sigma_H C \\ -\sigma_H S & \sigma_P S^2 + \sigma_{\parallel} C^2 & (\sigma_P - \sigma_{\parallel}) SC \\ -\sigma_H C & (\sigma_P - \sigma_{\parallel}) SC & \sigma_P C^2 + \sigma_{\parallel} S^2 \end{pmatrix} \quad (2.4)$$

where $\sigma_{\parallel}, \sigma_P, \sigma_H$ are field-aligned, Pedersen, and Hall conductivities respectively, and $S = \sin(I), C = \cos(I)$ where I is the magnetic dip angle. These conductivity terms represent both electrons and ions contributions which may be calculated as [*Kelley, 2009, Ch. 2, p. 45*]:

$$\sigma_{\parallel e,i} = |q_{e,i}| N_{e,i} \mu_{e,i} \quad (2.5)$$

$$\sigma_{Pe,i} = |q_{e,i}| N_{e,i} \mu_{e,i} (1 + \mu_{e,i}^2 B^2)^{-1} \quad (2.6)$$

$$\sigma_{He,i} = -q_{e,i} N_{e,i} \mu_{e,i}^2 B (1 + \mu_{e,i}^2 B^2)^{-1} \quad (2.7)$$

where $q_{e,i}$ is the electronic charge, $N_{e,i}$ is the number density and $\mu_{e,i} = q_e / (m_{e,i} \nu_{e,i})$ is the non-magnetized mobility for electrons and ions. For the 2D formulation, the azimuthal symmetry assumption mandates a vertical (upward or downward) geomagnetic field ($I = \pm\pi/2$) for which the conductivity tensor is reduced to:

$$\hat{\sigma} = \begin{pmatrix} \sigma_P & \sigma_H & 0 \\ -\sigma_H & \sigma_P & 0 \\ 0 & 0 & \sigma_{\parallel} \end{pmatrix} \quad (2.8)$$

Furthermore, when evaluating the second term of Equation 2.3, the dependence on Hall conductivity is removed due to the azimuthal symmetry assumption of the 2D

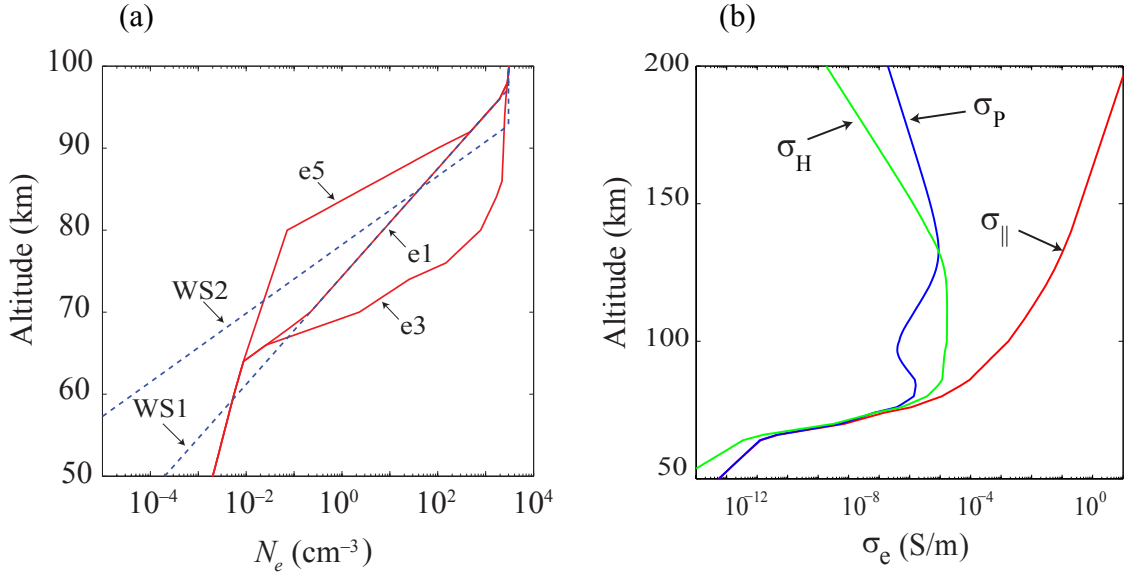


Figure 2.2: Ambient atmospheric and lower ionospheric profiles of (a) electron density and (b) electron conductivity.

formulation ($\partial/\partial\theta=0$) and thus the conductivity may be represented in (r, z) coordinates as:

$$\hat{\sigma} = \begin{pmatrix} \sigma_P & 0 \\ 0 & \sigma_{\parallel} \end{pmatrix} \quad (2.9)$$

The evaluation of the conductivity terms described in Equation 2.5–2.7 requires knowledge of the ambient electron and ion distributions. These parameters may be initialized from various theoretical and experimental profiles previously published.

Figure 2.2a shows various night-time ambient electron density profiles obtained from previous studies of atmospheric and ionospheric conditions. Profiles e1 and e3 are taken from profile 1 and 3 in Figure 4 of *Pasko and Inan* [1994] which have been used in the previous studies of subionospheric VLF propagation in the presence of localized ionospheric disturbances caused by lightning induced electron precipitation and later in sprite studies [*Pasko et al.*, 1997a]. Profile e5 is taken from *Pasko et al.* [1998] (profile E2 in Figure 1), where it was used in the study of mapping of thundercloud fields up to the ionosphere and the associated heating of the electron plasma. The WS1 and WS2 profiles are from the theoretical work of *Wait and Spies* [1964]

where the ambient electron density is given by the following equation:

$$N_e = N_{e0} e^{(-0.15h')} e^{(\beta-0.15)(h-h')} \quad (2.10)$$

Here, $N_{e0} = 1.43 \times 10^{13} \text{ m}^{-3}$, h [km] is height above the ground, and β [km^{-1}] and h' [km] represent the sharpness and reference altitude for the density profile, respectively. A larger value of β results in larger density gradients, while varying h' shifts the density profiles vertically. For a typical night-time ionosphere $h' = 85 \text{ km}$ [Han and Cummer, 2010] and $\beta = 0.5\text{--}0.7 \text{ km}^{-1}$ [Thomson et al., 2007] corresponding to WS1 and WS2 profiles in Figure 2.2a.

Figure 2.2b shows the ambient electron conductivity profiles used in this study. The electron contributions are found by using the ambient electron density profile e1 and assuming the mobility for cold electrons to be $\mu_e = 1.36N_0/N \text{ m}^2\text{V}^{-1}\text{s}^{-1}$, where $N_0 = 2.688 \times 10^{25} \text{ m}^{-3}$ and N is the number density of atmospheric molecules [Pasko, 1996, p. 33]. At altitudes above $\sim 60 \text{ km}$ the conductivity is dominated by the electron contribution, and at lower altitudes by the ions. Various ion conductivity profiles are used similar to Pasko [1996, Fig. 2.4] which are obtained from previous theoretical and experimental studies of ion conductivity above thunderstorms [Dejnakarintra and Park, 1974; Holzworth et al., 1985; Hale, 1994]. The ion conductivities are assumed to be constant in time in our model since the ions are not significantly heated by the electric fields. The differences in the above ion conductivity profiles represent the variability in the lower atmospheric conductivity and are valid for altitudes below $\sim 60 \text{ km}$. At higher altitudes we calculate the ion conductivity from Equations 2.5–2.7 by using the known ion mobility as a function of altitude, namely $\mu_i \sim 2.3N_0/N \text{ m}^2\text{V}^{-1}\text{s}^{-1}$ [Davies, 1983] and assuming singly charged positive ions and plasma approximation ($N_e \simeq N_i$). By doing so we use the fact that, at these altitudes, the contribution of negative ions to the total conductivity is negligible compared to that of the electrons.

2.4 Nonlinear Effects and Self-consistent Evaluation of Conductivity

Self-consistent evaluation of conductivity in the above formulation is a key point in the calculation of thundercloud electrodynamic upward coupling. The contributions to the field-induced conductivity changes come from the changes in both electron mobility and number density.

In a weakly ionized plasma environment such as the mesosphere and the lower ionosphere, the electron mobility is a nonlinear function of the applied electric field. At altitudes higher than ~ 60 km where the atmospheric conductivity is mainly dominated by the electron contribution, this nonlinear dependence becomes especially important. The electron mobility dependence on E may be obtained from the results of experimental studies (e.g., electron swarm experiment [[Davies, 1983](#)]) or the kinetic solutions of the Maxwell-Boltzmann equation [[Taranenko et al., 1993a,b](#); [Marshall, 2012](#)] and is a complex function of electric field determined by the various loss processes each with a different cross section.

Figure 2.3a shows the mobility as a function of the reduced electric fields E/N , which may be used at any altitude. The electron mobility change due to the applied electric field occurs because the effective electron temperature is increased and therefore is often referred in the literature as the electron heating. It may be understood also in terms of the change in the effective collision frequency of the electrons $\nu_{\text{eff}} = q_e/(\mu_e m_e)$. The heated electrons collide more frequently in general (we must also take into account that the collision cross-section also depends on the electron velocity). An important take-away point from Figure 2.3a is that with increasing electric field the electron mobility decreases because the effective collision frequency increases. We revisit this point in Chapters 3–5 and show its importance in modeling of upward electrodynamic coupling of thunderstorms.

Another important nonlinear effect included in the model is the change of electron density with the applied electric field. In the lower ionosphere electrons are a very small fraction of the total atmospheric constituents and thus interact (collide) with ions and neutral particles frequently. These interactions lead to many different

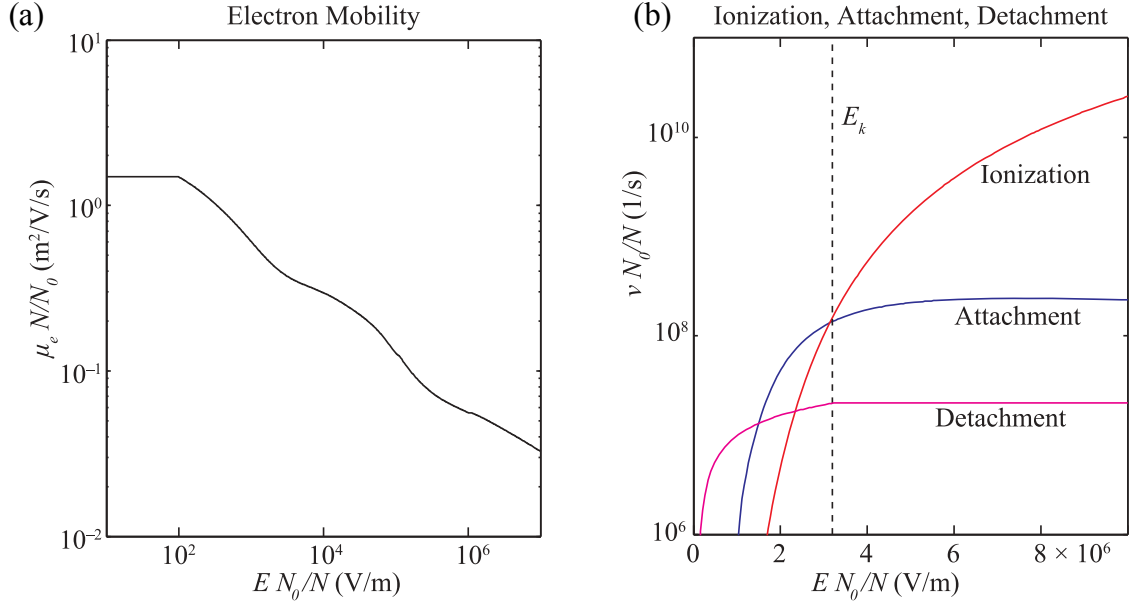


Figure 2.3: Nonlinear changes of (a) electron mobility and (b) ionization, attachment, and detachment rates with electric field (adapted with modification from [Marshall \[2012\]](#))

chemical reactions which can change the electron density and energy distributions on various time scales. For thundercloud upward coupling as well as sprite and halo studies where the physical processes mostly involve very short time scales, the most important chemical reactions identified by previous studies [[Pasko et al., 1997a](#); [Luque and Gordillo-Vázquez, 2012](#)] are as follows :



The first two reactions (2.11 and 2.12) are responsible for new free electron production via electron impact ionization of O_2 and N_2 molecules. Reaction 2.13 is the electron

loss process due to dissociative attachment of electrons with O_2 molecules. This reaction increases the density of O^- ions in the environment which can be subsequently removed after an impact with N_2 molecules through the associative detachment, process 2.14, which releases an electron in the process. The chemical reactions described above can significantly change the number density of constituents in the lower ionosphere when the electric field is applied, because the rates of these reactions have a strong nonlinear dependence on the electric field as shown in Figure 2.3b. These rates can be found from experimental data [Davies, 1983], kinetic solutions [Taranenko et al., 1993b], or computer simulations combined with experimental measurements [Papadopoulos et al., 1993] with reasonable agreement in the range of electric field values relevant to the present problem. With the given reactions and their known rates at various electric fields, we can calculate the evolution of the electron density profile in our model from the following system of equations:

$$\frac{\partial N_e}{\partial t} = (\nu_i - \nu_a) N_e + \nu_d N_{O^-} \quad (2.15)$$

$$\frac{\partial N_{O^-}}{\partial t} = \nu_a N_e - \nu_d N_{O^-} \quad (2.16)$$

where ν_i , ν_a , and ν_d are the impact ionization and dissociative attachment and associative detachment rates as shown in Figure 2.3b.

2.5 The Earth Magnetic Field

As was mentioned in Section 2.3, the azimuthal symmetry assumption of the 2D model mandates a vertical magnetic field which significantly reduces the applicability of the model. As shown in Figure 2.4, this magnetic field configuration corresponds to high latitude regions of the Earth. However, majority of thunderstorms occur at lower latitudes and their upward electrodynamic coupling is thus more significant at lower latitudes as it is evident by the number of sprite and halo events observed at those latitudes [Chen et al., 2008]. There, the magnetic field has a large horizontal

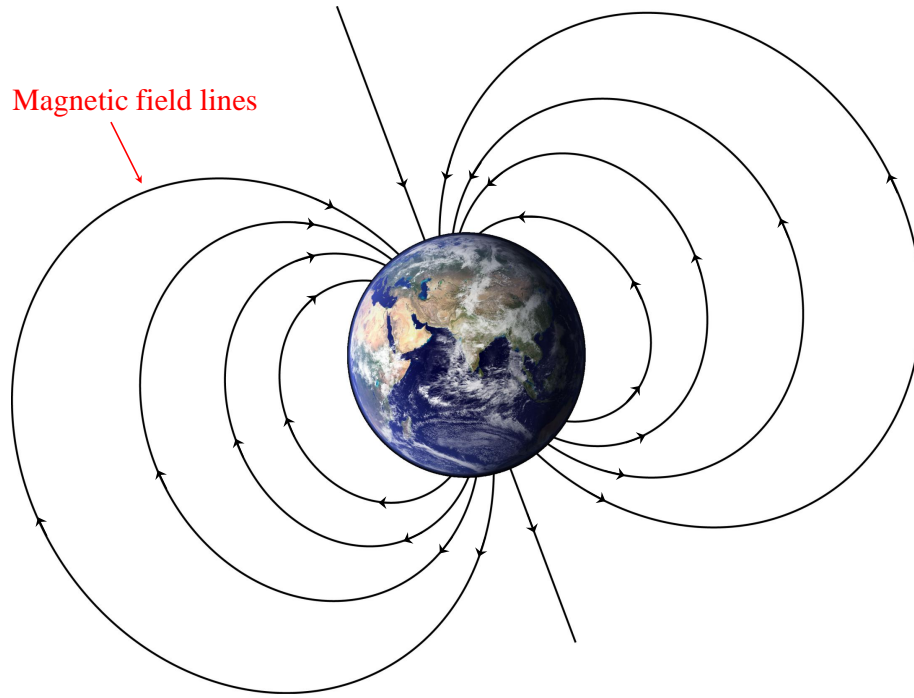


Figure 2.4: The dipole model of the Earth's magnetic field.

component and to study the effects of the Earth's geomagnetic field on the quasi-electrostatic fields, a 3D model which can incorporate a realistic background magnetic field must be utilized.

In the 3D model we include a realistic magnetic field based on a dipole magnetic field configuration, schematically demonstrated in Figure 2.4. This model is accurate enough for our purposes up to several thousand kilometers above the ground which is well above the top boundary in our model. The vector components of the geomagnetic field are

$$B_r = -2B_0 \left(\frac{R_E}{r} \right)^3 \sin \lambda \quad (2.17)$$

$$B_\theta = B_0 \left(\frac{R_E}{r} \right)^3 \cos \lambda \quad (2.18)$$

$$|B| = B_0 \left(\frac{R_E}{r} \right)^3 \sqrt{1 + 3 \sin^2 \lambda} \quad (2.19)$$

where $B_0 = 3.12 \times 10^{-5}$ T is the magnitude of the field on the ground at the equator,

$R_E \simeq 6371$ km is the Earth's radius, r is the distance from the Earth's center in kilometers, and λ is the magnetic latitude. Chapters 3–5 show in detail the implications of the non-vertical geomagnetic fields on the thunderstorm quasi-electrostatic fields which have been neglected in previous 2D models and studies of thunderstorm upward electrodynamic coupling.

2.6 Parallel Computing and Domain Decomposition

The 2D quasi-electrostatic model of *Pasko* [1996] has been used for about two decades to study the thunderstorm electric fields and their upward coupling. Due to the high computational cost of the model, however, many applications remain unexplored. For example, the azimuthal symmetry assumption of the 2D model prevents us from considering the effects of geomagnetic fields. Moreover, the effects of the horizontal charge transfer such as in IC lightning discharges and realistic, non-symmetric charge distributions have not been previously studied. The applications of the model have thus been limited to inputs which only very approximately describe realistic thunderclouds and which exclude the potential use of the model with inputs corresponding to the varying conditions obtained from experimental data. These considerations thus motivate the development of a 3D model.

At the core of the quasi-electrostatic model, one has to solve the Poisson and the continuity equations (Equations 2.2 and 2.3). Solving Poisson equation requires the solution of a sparse matrix whose dimensions grow in proportion to the number of grid points in the simulation domain. Solution of this system of equations is often a computationally expensive task and requires well designed software and fast numerical solvers. In order to calculate the time evolution of the fields and particles in the model, we have to utilize the continuity equation. The best modern approach to the solution of such an equation is to use the second-order Runge-Kutta (RK2) methods with a reasonable trade-off between the accuracy and numerical stability (see Section 2.2). Since RK2 is an explicit numerical scheme, the time step used

in the model has to be smaller than the smallest time scale in the model in order to assure numerical stability. Typically, the conductive relaxation time of the fields which inversely depends on the conductivity ($\tau_r \sim \epsilon_0/\sigma$) is the fastest time scale in the model. As the conductivity increases at higher altitudes, the fields relaxation time decreases, and one has to choose a smaller time step to satisfy the stability condition, which in turn increases the computational cost of the model.

The two above-mentioned computational complexities, namely the necessity to use many spatial grid points and a small time step, severely limit the computational capabilities of previously available 2D models which were designed to be executed on a single processor. The same limitation would apply to the design of a new 3D model, but even to a greater degree due to an increased number of grid points. In order to alleviate this problem, we employ parallel algorithms and techniques which enable the use of the power of a large collection of computers with multiple processing units. This technique has been previously used in many other academic and industrial fields. The class of numerical problems which can take advantage of these parallel techniques are said to have inherent concurrency, meaning that they can be solved by separate possibly communicating processing units.

In simulation of physical domains, a very popular technique used in many cases is to divide the simulation domain into smaller subdomains and use a separate processor for each subdomain. This technique is often referred to as *domain decomposition* in the parallel computing lexicon [[Quarteroni and Valli, 1999](#)]. This parallel algorithm works very well for models trying to solve differential equations with finite difference techniques, where the solution of the model at each point in the simulation grid may be calculated based on the knowledge of the previous solutions at that and possibly neighboring grid points.

To develop a better and faster 2D quasi-electrostatic model, we can use the domain decomposition technique. Here, we decompose our 2D (r, z) simulation domain into smaller subdomains in either r or z , (or both) directions. The solution of the equations in each subdomain can then be assigned to a specific processing unit. In this method, the points at the boundary of each smaller simulation grid often need to be shared with the adjacent processors at every iteration in time, being passed between the

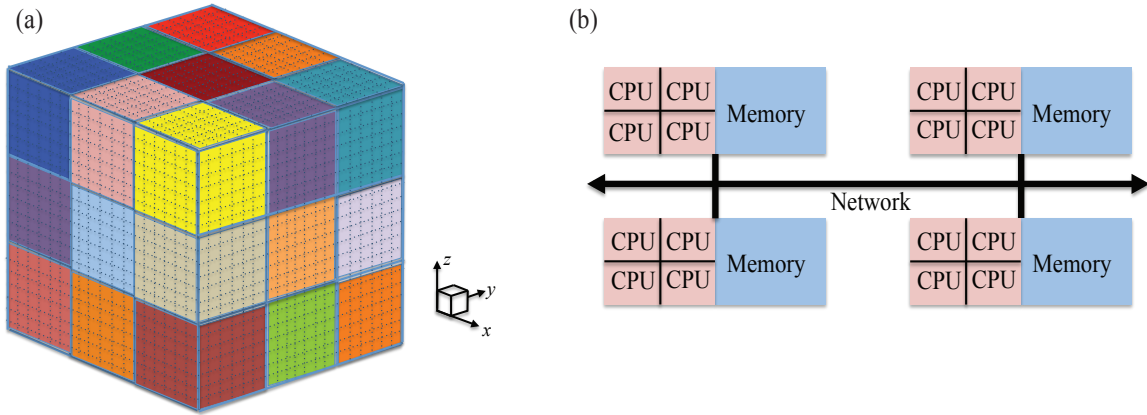


Figure 2.5: (a) A decomposed Cartesian grid into smaller subdomains for the domain decomposition technique and (b) the computer architecture used with MPI for the parallel solution of the equations.

processors using the Message Passing Interface (MPI).

To address the limitations of the 2D model explained above, we need to develop a 3D model. Moving from the 2D domain with (n_1, n_2) grid points to the 3D domain with (n_1, n_2, n_3) grid points, our simulation domain becomes $(n_3 - 1) \times n_2 \times n_1$ times larger and thus our model computational cost increases by at least $O(n_3)$ times. This estimate is in fact the lower limit on the increased complexity since the computational cost of the solution of the system of equations from Poisson's equation usually increases non-linearly with the number of unknowns. The large system of equations compared to the 2D model creates an immense memory and computational cost which would not be affordable on a single processing unit. To resolve this problem, we use the same domain-decomposition parallel technique explained above, this time in three dimensions (x, y, z) . The simulation domain can be similarly divided in one, two, or three dimensions into smaller subdomains. Figure 2.5a shows an example of a decomposed domain in all x , y , and z directions of a 3D Cartesian coordinate grid. Each smaller grid section, shown with a different color, can be assigned to a distinct processor and the processors can communicate with each other via a common network in order to obtain the necessary information for the solution of the equations as shown schematically in Figure 2.5b.

The parallel QES 2D model may be used for extremely fast solutions, e.g., when

we need multiple solutions for a large set of various inputs. Alternatively, in the same runtime as that of a serial (non-parallel) 2D model, one can increase the spatial resolution of the model and thus greatly improve the resultant accuracy. The higher spatial resolution is also very important in the study of small-scale physical phenomena, such as streamers, that need a very fine grid structure, smaller than the streamer length scale. For example, to obtain the higher spatial resolution for streamer physics, [Luque and Ebert \[2009\]](#) used a serial-computation model with Adaptive Mesh Refinement (AMR) algorithms to study the sprite streamer inception from the sprite halos. The results of their model, however, were later attributed to numerical instabilities by [Qin et al. \[2011\]](#) due to the coarse numerical grid used in the model. With the future inclusion of the equations for streamer physics and the combination of non-uniform grids [[Moin, 2010](#), Ch. 2, p. 23–25], the 2D parallel model has the potential to be used as an alternative approach to some of the previous models in describing the streamer formation from sprite halos.

2.7 Solution of QE Equations in Time

As was mentioned in Section 2.6, the explicit second-order Runge-Kutta scheme used in many previous studies [[Pasko, 1996](#); [Inan et al., 1996b](#); [Pasko et al., 1997a](#); [Lehtinen et al., 1997](#), etc.] requires an adaptive time step which depends on the maximum conductivity in the model. The simulation maximum altitude must thus be chosen with consideration of the computational cost of the model as a higher altitude results in smaller time steps and thus larger number of time steps to simulate a specific time period of the thunderstorm and atmospheric dynamics. The use of parallel algorithms described in the previous section can help solve each time step faster and thus speed up the simulation runtime. However, such an approach is still computationally wasteful and could be improved by using an algorithm that has better stability region for the same or higher numerical order of accuracy so that one can take larger and fewer time steps.

2.7.1 Exponential Time Differencing Method with Runge-Kutta Time Stepping

The second-order Exponential Time Difference Runge-Kutta (**ETD2RK**) method of *Cox and Matthews* [2002] developed for stiff systems has been shown to have better accuracy and a superior numerical stability when compared to other standard second-order numerical schemes such as the second-order Adams-Bashforth/Adams-Moulton (AB2AM) methods (for example see Figure 1 of *Cox and Matthews* [2002]). The model ordinary differential equation (ODE) used by *Cox and Matthews* [2002] is:

$$\dot{u} = au + F(u, t) \quad (2.20)$$

where a is a constant and $F(u, t)$ represents nonlinear and forcing terms. After multiplying both sides by the integrating factor e^{-at} and integrating the equation over a single time step from $t = t_n$ to $t = t_{n+1} = t_n + h$, we find the *exact* expression:

$$u(t_{n+1}) = u(t_n)e^{ah} + e^{ah} \int_0^h e^{-a\tau} F(u(t_n + \tau), t_n + \tau) d\tau \quad (2.21)$$

To use the exponential time differencing method with Runge-Kutta time stepping to solve the equation, the first step of the Runge-Kutta scheme (the predictor step) is found by assuming F is constant between $t = t_n$ to $t = t_{n+1}$, $F = F_n + O(h)$. Thus, Equation 2.21 becomes:

$$u_{n+1}^* = u_n e^{ah} + F_n (e^{ah} - 1)/a \quad (2.22)$$

with a local truncation error of $h^2 \dot{F}/2$. The second step of the Runge-Kutta scheme (the corrector step) then uses the approximation $F = F(u_n + t_n) + (t - t_n)(F(u_{n+1}^*, t_n + h) - F(u_n, t_n))/h + O(h^2)$ in solving the exact Equation (2.21) which yields the **ETD2RK** solution

$$u_{n+1} = u_{n+1}^* + (F(u_{n+1}^*, t_n + h) - F_n)(e^{ah} - 1 - ha)/ha^2 \quad (2.23)$$

with a local truncation error of $-h^3\ddot{F}/12$.

Due to the large variation of the conductivity from the ground up to the ionosphere and thus the large relaxation time-scales present in the model, the quasi-electrostatic formulation creates a stiff system of equations. To demonstrate, we can rewrite Equation 2.3 as

$$\frac{\partial \rho}{\partial t} = -\frac{\sigma_{\parallel}}{\epsilon_0}\rho + \sigma_{\parallel}\nabla \cdot \vec{E} - \nabla \cdot \sigma \vec{E} \quad (2.24)$$

where we replaced ρ_s using Poisson's equation, $\rho_s = \epsilon_0\nabla \cdot \vec{E} - \rho$. Equation 2.24 is similar to 2.20 if we choose $a = -\sigma_{\parallel}/\epsilon_0$ and $F = \sigma_{\parallel}\nabla \cdot \vec{E} - \nabla \cdot \sigma \vec{E}$. However, due to the self-consistent treatment of the conductivity, here a is not a constant and can change in time.

We can extend the results of *Cox and Matthews* [2002] to the case where $a = a(t)$. Equation 2.21 can be rewritten as

$$\int_0^h \dot{u}e^{-a\tau} d\tau = \int_0^h aue^{-a\tau} d\tau + \int_0^h e^{-a(\tau+t_n)} F(u, t_n + \tau) d\tau \quad (2.25)$$

Similar to Equation 2.22 we can assume F and a as constant ($F = F_n$ and $a = a_n$) in the predictor step of Runge-Kutta scheme. Evaluating the equation at $t_n + h/2$ yields:

$$u_{n+\frac{1}{2}}^* = u_n e^{a_n h/2} + F_n (e^{a_n h/2} - 1)/a_n \quad (2.26)$$

With the given $u_{n+\frac{1}{2}}^*$ we can find an estimate for $a_{n+\frac{1}{2}} = a^*$ for the updated conductivity (see Section 2.4). We then use this estimate to formulate the corrector step by assuming $F = F(a^*, t_{n+\frac{1}{2}})$ and $a = a^*$ as follows:

$$u_{n+1} = u_n e^{a^* h} + F_{n+\frac{1}{2}} (e^{a^* h} - 1)/a^* \quad (2.27)$$

Expanding the Taylor series of the time dependent variables confirms the second order accuracy of the scheme.

2.7.2 Implicit Adams-Moulton Method

The modified continuity equation as written in the Equation 2.24 can also be solved by using an implicit trapezoidal rule for the first term on the right hand side and an explicit euler rule for the second and third terms on the right hand side given by

$$\rho_{n+1} = \frac{(1 - h\sigma_{\parallel}/2\epsilon_0)\rho_n - (\nabla \cdot \sigma \vec{E} - \sigma_{\parallel} \nabla \cdot \vec{E})h}{1 + h\sigma_{\parallel}/2\epsilon_0} \quad (2.28)$$

The above scheme is accurate to first order and is conditionally stable since the second term in the numerator on the right hand side $(\nabla \cdot \sigma \vec{E} - \sigma_{\parallel} \nabla \cdot \vec{E})$ is evaluated at t_n .

Alternatively, we can use the second-order Adams-Moulton scheme (trapezoidal rule) for Equation 2.3, assuming the conductivity changes are small in each time step, which yields

$$\rho_{n+1} = \rho_n + \frac{h}{2} \left[\nabla \cdot (\hat{\sigma} \nabla (\Phi_n + \Phi_{n+1})) + \frac{\sigma_{\parallel}}{\epsilon_0} (\rho_{s,n} + \rho_{s,n+1}) \right] \quad (2.29)$$

If we combine Equation 2.29 with Poisson's equation, we can obtain the following scheme

$$-\left[\nabla^2 + \frac{h}{2\epsilon_0} \nabla \cdot (\hat{\sigma} \nabla) \right] \Phi_{n+1} = \frac{\rho_n + \rho_{s,n+1}}{\epsilon_0} + \frac{h}{2\epsilon_0} \left(\nabla \cdot (\hat{\sigma} \nabla \Phi_n) + \frac{(\rho_{s,n} + \rho_{s,n+1})\sigma_{\parallel}}{\epsilon_0} \right) \quad (2.30)$$

The above equation is accurate to second order and is unconditionally stable if the time scale of the conductivity change is much larger than the time step of the algorithm. If the conductivity varies faster than the time step, then the accuracy reduces to first order. However, our empirical analysis shows that the unconditional stability of the equation still remains.

The top boundary used in the current models of thunderstorm electrostatics is assumed to be less than ~ 60 km [Krehbiel *et al.*, 2008]. At these altitudes, the conductivity is dominated by the ions and the dynamical changes of the electron conductivity can thus be ignored. The above improved numerical scheme can thus calculate the quasi-electrostatic fields at these altitudes with very good accuracy and computational efficiency.

The above developed numerical algorithms have been tested against the more traditional RK2 schemes used in previous studies [[Pasko et al., 1997a](#); [Lehtinen et al., 1997](#)] and produce similar results for the simulated physics in all cases. Throughout the rest of this dissertation, however, we only employ the previously used and rigorously tested second order Runge-Kutta scheme. We may thus be assured that the new results obtained with the new model are due to the newly included physics, and that the possibility of new results to be artifacts of numerical error be minimized. Furthermore, we make an important and interesting observation that the equation set solved in the quasi-electrostatic model also appears in other areas of physics so that our approach may possibly be applicable in many other applications as well.

Chapter 3

Electrostatic Upward Coupling of Thunderstorms

Electrostatic fields generated by thunderclouds can significantly heat and modify the lower ionospheric electrons at altitudes of 70–80 km. These fields can also map to higher altitudes along the geomagnetic field lines and have been proposed as the mechanism for generation of whistler ducts. Previous 2D modeling of these fields have been limited to azimuthally symmetric cases which require a vertical magnetic field. Incidentally, in this case, as shown later in this Chapter, the electric field mapped into the magnetosphere is significantly smaller than that with a non-vertical geomagnetic field, therefore such a limited model may significantly underestimate the role of thunderclouds in formation of whistler ducts. Here we use the 3D model of the electrostatic thundercloud fields developed in Chapter 2 which allows the consideration of the effects of the geomagnetic field dip angle $I \neq \pm 90^\circ$ on the mapping of the fields to high altitudes. The results show stronger electric fields at altitudes of 70–110 km with an equatorward and eastward shift of tens of kilometers at lower geomagnetic latitudes. These stronger fields are mapped into the magnetosphere and may therefore be important for whistler duct generation. The fields also indicate a more significant quiescent heating of the ionosphere by underlying thunderstorms, leading to potentially larger Early/Fast VLF signal changes in response to individual lightning discharges.

Most of the results presented in this chapter are published in [Kabirzadeh et al. \[2015\]](#).

3.1 Introduction

The influence of thundercloud electrostatic and quasi-electrostatic fields at high altitudes ($\sim 60\text{--}150$ km) has been the subject of numerous studies (see, for example, [Holzer and Saxon \[1952\]](#), [Park and Dejnakintra \[1973\]](#), [Dejnakintra and Park \[1974\]](#), [Tzur and Roble \[1985\]](#), [Pasko et al. \[1995\]](#), [Inan et al. \[1996b\]](#), [Pasko et al. \[1998\]](#), [Pulinets et al. \[2000\]](#), [Tonev and Velinov \[2005\]](#)). The fields are generated by charged particles created by various mechanisms in the thundercloud and distributed by updrafts within the cloud. The charging process takes place over many minutes and the fields created can thus be considered electrostatic. A lightning discharge results in the sudden removal or redistribution of the thundercloud charges and can thus disturb the steady-state conditions. These disturbances persist over a relatively long time scale and thus may be considered as quasi-electrostatic (QE). The quasi-electrostatic field perturbations due to lightning discharges at high altitudes and their role in generation of sprites and runaway electrons have been also the subject of many studies [[Lehtinen et al., 1996, 1997](#); [Pasko et al., 1997a](#); [Qin et al., 2011](#), and references therein]. These phenomena are also influenced by the steady-state conditions generated by the electrostatic fields before the lightning strike such as the quiescent heating of the ionospheric electrons [[Inan et al., 1996b](#); [Pasko et al., 1998](#)].

The thundercloud electrostatic fields may also have a role in whistler duct formation when they penetrate higher upward. Based on the simple model of [Holzer and Saxon \[1952\]](#), there are three factors that increase penetration of thundercloud fields to ionospheric altitudes: 1) higher altitude of thundercloud charges, 2) larger magnitude of these charges, and 3) larger scale height of ambient conductivity profile. Due to very high specific conductivity, the electrostatic potential can map from the ionospheric D and E regions to higher altitudes along the geomagnetic field lines with very small attenuation. [Park and Helliwell \[1971\]](#) showed that transverse (i.e.,

perpendicular to the geomagnetic field) electric fields of 10 mV/m at 100 km altitude can create 5% field-aligned electron density variations at $L=4$ in ~ 30 minutes, which can trap whistler waves. The same authors proposed thunderclouds as the source of this electric field. With a simple analytical model considering a single point charge inside the thundercloud at mid to high latitudes, *Park and Dejnakarindra [1973]* (hereafter referred to as PD73) calculated the transverse electric fields to be $\sim 50 \mu\text{V/m}$ in the equatorial plane of the magnetosphere. They also considered the effects of anisotropies in the ionospheric conductivity for altitudes above ~ 70 km. Their calculations show that with anisotropic conductivities, i.e., taking into account the effect of the geomagnetic field, maximum radial electric field, E_r^{max} , is 3 orders of magnitude larger than in the case of isotropic conductivity. Although PD73 model calculations considered a vertical geomagnetic field, the effects of these fields at lower latitudes are stronger since the attenuation of fields due to geomagnetic field line divergence when they are mapped to magnetosphere is weaker for these lower latitudes [*Park and Helliwell, 1971*]. The model of PD73 has been since used by many others to study the thundercloud electrostatic fields and their role in high altitudes chemistry and dynamics. *Vellinov and Tonev [1994]* improved the PD73 model for a thundercloud with multiple charge layers, by modeling the finite sizes of charges using a disk shape. They showed, as PD73 had predicted, that in most cases the relative contribution of the lowest positive charge for E_r in a thundercloud with three charge layers is negligible. *Vellinov and Tonev [1994]* further took into account electron production, loss, and advection and showed that the intense E_r can produce an electron hole above a thunderstorm of radius 50–100 km in the E and F regions. On the other hand, for an inverted dipole charge distribution, an electron density enhancement was created at the same heights. *Vellinov and Tonev [1995]* further improved the previous models by using a piecewise exponential conductivity profile and found values of $E_r^{\text{max}} = 10 \mu\text{V/m}$ at $z = 150$ km (for a charge $Q = 100$ C at $z_0 = 15$ km), which are about 2 orders of magnitude smaller than the values obtained by PD73.

Rodger et al. [1998a] tested the formulation of PD73 and confirmed it to be consistent with the experimental results of *Holzworth et al. [1985]*. The authors, however,

suggested a much smaller upper (10–15 km) positive charge (7–8 C compared to 40–70 C suggested by *Holzworth et al.* [1985]) based on the model results and argued that the lower charge may be due to the screening charge layer above the top layer. Thundercloud electric fields at high altitudes and their possible role in whistler duct formation was also considered by *Rodger et al.* [1998b, 2002] and *McCormick et al.* [2002] with contradicting conclusions. Namely, *Rodger et al.* [1998b, 2002], using experimentally measured conductivity profiles of the atmosphere [*Hale, 1984; Holzworth et al., 1985*], suggested that the fields can play an important role in the duct creation, while *McCormick et al.* [2002], using the same conductivity profiles and a more realistic charge structure, argued that the fields are not important.

The non-vertical geomagnetic field may significantly influence the geometry and magnitude of thundercloud electrostatic fields in the lower ionosphere (D and E region) as well. *Tonev and Velinov* [2002] were the first to consider the effects of non-vertical geomagnetic field on the structure and strength of the electrostatic fields above a thunderstorm. They solved for the electrostatic fields at polar and equatorial latitudes (vertical and horizontal magnetic fields). At the equator, they reported an eastward horizontal shift of 3–100 km at 70–100 km altitude in the electric field structure, which increased with altitude. Their results, however, underestimated the experimental results found by *Holzworth et al.* [1985] by a factor of ~ 3 . The authors explain the discrepancy by stating that “the model can not adequately reflect the modification of the thundercloud conductivity itself”. The asymmetric structure and the shift of the electric field were later also predicted for the transient quasi-electrostatic fields following a lightning discharge [*Tonev and Velinov, 2005*].

Pasko et al. [1998] developed a cylindrically symmetric 2D numerical model, self-consistently solving for conductivity changes by taking into account the electron heating. The electric field used was below breakdown threshold and thus no ionization effect was considered. Intense heating regions were predicted with lateral extent varying from 150 km to 350 km and the vertical extent of about 10 km covering most of the D region at 70–80 km which could extend to 85 km depending on the conductivity profile used. The heating effect on the specific conductivity, σ_{\parallel} , which controls the

penetration of the vertical component of the electric field, is such that the conductivity in the lower part of D region is decreased but then sharply increases to the values which remain at the ambient level at higher altitudes. The decrease of σ_{\parallel} smooths out the vertical gradients, facilitating the upward penetration of the vertical electric fields. However, the sudden increase of conductivity, inhibits the penetration so that at 90 km the electric field is 70% lower than in the case without heating.

In this chapter, a high-resolution three-dimensional electrostatic heating model is developed to determine the penetration of electric fields generated by a thundercloud into ionosphere. The model self-consistently considers E -field-driven electron heating and the resulting conductivity changes and can include a realistic geomagnetic field. For this study we consider only the long time scale effects (minutes to hours) in the charge accumulation phase of the thundercloud.

3.2 Model

The model is based on the solutions of the quasi-electrostatic equations [[Pasko et al., 1998](#)] in a three dimensional Cartesian coordinate system. The axes are chosen so that \hat{x} points to the magnetic east, \hat{y} is in the meridian plane and points to the magnetic north, and \hat{z} points to the zenith. The electrostatic potential Φ in the simulation domain is found from charge conservation equation

$$\nabla \cdot \vec{J}_{\text{tot}} = \nabla \cdot (-\hat{\sigma} \nabla \Phi + \vec{J}_{\text{s}}) = 0 \quad (3.1)$$

where the source \vec{J}_{s} is the current density inside the thunderstorm responsible for the electrification of the cloud. The conductivity tensor, $\hat{\sigma}$, for a magnetic field in the yz plane is found from Equation 2.4. The total conductivity tensor consists of both ion and electron conductivities, $\hat{\sigma} = \hat{\sigma}_{\text{e}} + \hat{\sigma}_{\text{i}}$. At altitudes below $z = 70$ km the ion-neutral and electron-neutral collision frequencies are much higher than the ions and electrons gyro-frequencies. Thus ions and electrons can be considered as unmagnetized and the conductivity tensors are approximately diagonal. The model ion conductivities at these altitudes are constant in time during the simulation and are initialized to

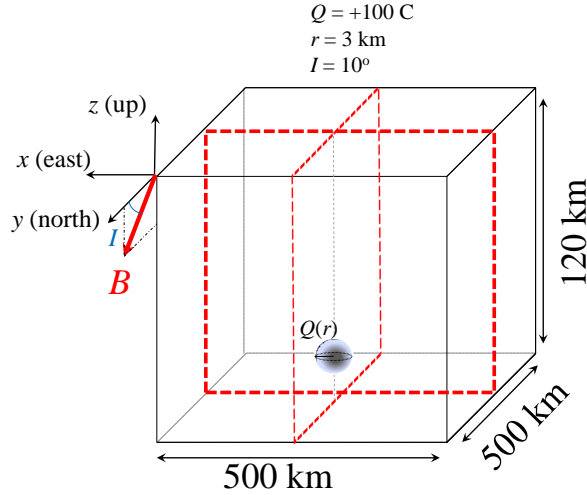


Figure 3.1: Cartesian coordinate system configuration used here, shown with a magnetic dip angle $I = 10^\circ$. The red dashed rectangles illustrate the two orthogonal slabs of the domain where the solution is shown in Figure 3.2.

a profile obtained from previous experimental and modeling studies of atmospheric conductivities [Hale, 1984; Holzworth et al., 1985; Park and Helliwell, 1971]. At higher altitudes electron and ion conductivities can be expressed by Equations 2.5–2.7. We use a dipole-model geomagnetic field, $B = (B_0/R^3) \sqrt{1 + 3 \sin^2 \lambda}$, where R is the distance from the center of the Earth in Earth radii, λ is the geomagnetic latitude and $B_0 = 3.06 \times 10^{-5}$ T. The electron mobility changes greatly with electric field and introduces nonlinear behavior into the calculations. The changes in the electron density due to ionization and attachment are neglected here since the calculated electric fields are well below the values at which the effect of these processes becomes appreciable [Inan et al., 1996b; Pasko et al., 1998].

The second term in Equation (3.1) may be expressed as $\nabla \cdot \vec{J}_s = -\rho_s \sigma_{\parallel} / \epsilon_0$ where ρ_s is the source charge density inside the thundercloud [Pasko et al., 1998].

Equation (3.1) with a constant ρ_s is solved on a three-dimensional structured grid in the Cartesian coordinate system as illustrated in Figure 3.1. In order to take the conductivity changes into account self-consistently, the equation is solved iteratively until the conductivities and electric fields converge to their final values as in Pasko et al. [1998], a process which usually takes only a few iterations. At the side

boundaries we can use any combination of Dirichlet or Neumann boundary conditions (e.g. $\Phi = 0$ or $\partial\Phi/\partial x = 0$ respectively at $x = \pm x_{\max}$). At $z = 0$ the ground conductivity can be assumed as infinite for the electrostatic case and thus we can take $\Phi = 0$. The choice of the boundary conditions at the top boundary, however, is more complicated. For example, Dirichlet ($\Phi = 0$) condition may not be used because it amounts to “short-circuiting” the transverse E -field, in which we are interested, in particular, for its role in the generation of the whistler ducts. One way to overcome this problem is to extend the boundary to the conjugate hemisphere. However, such an extension is computationally prohibitive. A better choice of the boundary conditions would be to assume that only the electric field component parallel to the B field (due to the very high parallel conductivities) is zero at the top boundary. This assumption is also consistent with satellite and rocket observations of the parallel DC electric fields in the topside ionosphere and the magnetosphere. With the choice of the magnetic field direction in the yz plane we can express this condition as follows:

$$\frac{\partial\Phi}{\partial y} \cos I - \frac{\partial\Phi}{\partial z} \sin I = 0 \quad (3.2)$$

Condition (3.2) is neither a Dirichlet nor a Neumann boundary condition and the existence and uniqueness of the solution to (3.1) is not guaranteed. However there has been at least one previous report of its use which has produced successful results [Moelter *et al.*, 1998]. Note that the condition reduces to a Neumann boundary condition for a vertical magnetic field. Although a rigorous mathematical proof of the existence of the solution with the above boundary condition is beyond the scope of this study, our analysis and results shown in the next section support the correctness of the solutions and corroborate the validity of our assumptions. The choice of the top boundary as described by Equation (3.2) is limited to altitudes above ~ 120 km where the parallel conductivity exceeds several orders of magnitude the conductivities across the magnetic field lines and the magnetic field lines can be considered as equipotential. This boundary condition might not be valid in the case of strong field-aligned currents like during a magnetospheric substorm.

At the side boundaries, both Dirichlet and Neumann boundary conditions introduce an error of 5–10% in the solutions close to the boundary. Thus, to minimize the error in the region of interest, it is necessary to take the side boundaries at a far enough distance away from the center of the charge distributions. On the other hand, the spatial discretization of the Equation (3.1) is second-order accurate and to minimize the error from the finite-difference approximation of the derivatives a small spatial grid size $(\Delta x, \Delta y, \Delta z)$ should be chosen. These two requirements dictate a very large number of grid points in each direction, which results in a very large system of discretized equations to be solved. In order to optimize the computer resources, we use a non-uniform coordinate system in the x and y directions, with a higher resolution in the region of interest, i.e., around the middle of the computational domain. To keep the second order accuracy of the finite approximations we use the chain rule method for derivatives [Moin, 2010, Ch. 2, p. 23–25].

Even when using non-uniform grids, the system of discretized equations is still too large to fit in the memory of a single computer, and even if enough memory is found, the limited processing power of a single computer would still not allow the calculation to be completed in a reasonable time. To overcome this problem, the model is parallelized using the domain-decomposition method for better performance, and the sparse system of difference equations is solved using HYPRE package with generalized minimal residual (GMRES) solver with a Semi-coarsening Multi-grid (SMG) preconditioner [Falgout *et al.*, 2006].

In order to obtain the results shown in the next section we put the side boundaries 300 km away from the center of charge distributions and the top boundary at 200 km altitude. We discretize the domain with $(856 \times 856 \times 500)$ points with a resolution of 339–8053 m depending on whether we are at the center of the domain or close to the side boundaries. The equations are solved with 56 processing cores on a cluster of computers each with 64 GB of memory and 12 processors.

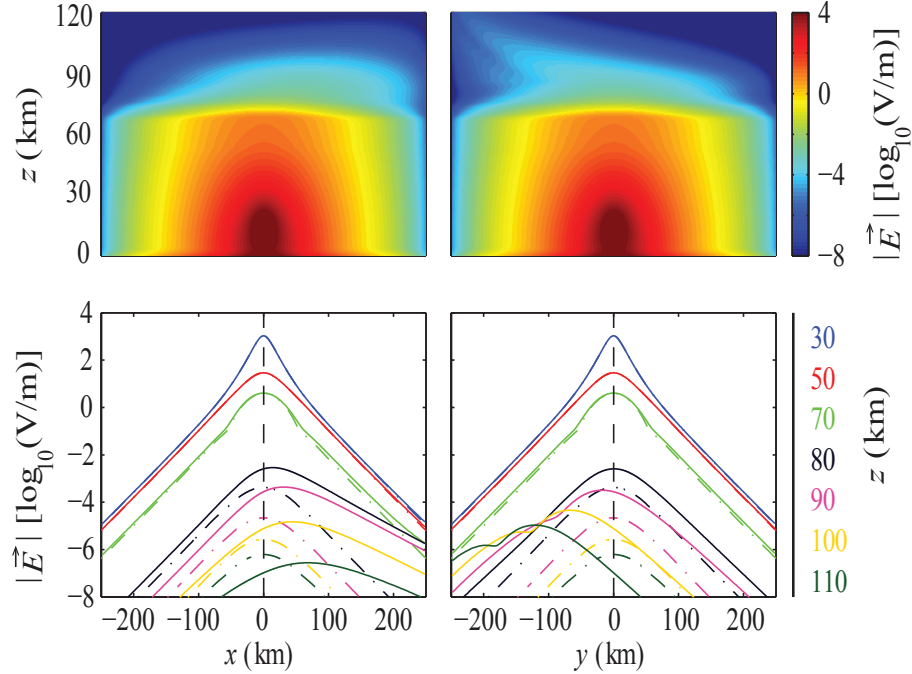


Figure 3.2: Top row: Electrostatic fields at xz and yz planes passing from the center of charge distributions at low latitudes (dip angle $I = 10^\circ$). Bottom row: Electric field profiles at selected altitudes and the comparison between high latitude ($I = 90^\circ$, dash-dot lines) and low latitude (solid lines) fields.

3.3 Results

Figure 3.2 shows the magnitude of the electrostatic fields found from solving equation (3.1) on xz plane at $y=0$ and yz plane at $x=0$ (see Figure 3.1). The top row shows the field intensities on a logarithmic scale and the bottom row displays the corresponding electric field profiles at selected altitudes represented by different colors. The results of the 2D model which assumes a vertical geomagnetic field are shown in the line plots as dash-dot lines, and the 3D model results with a 10° magnetic dip angle are plotted as solid lines. To isolate the effect of the geomagnetic field direction, the system of source charges has been kept the same, namely azimuthally symmetric, in both 3D and 2D models. The upper thundercloud charge was assumed to be a

Gaussian-distributed monopole charge of 100 C:

$$\rho_s(x, y, z) = \rho_0 \exp \left[- \left(\frac{(x - x_0)^2}{a^2} + \frac{(y - y_0)^2}{b^2} + \frac{(z - z_0)^2}{c^2} \right) \right]$$

where $x_0 = 0$, $y_0 = 0$, $z_0 = 15$, $a = b = c = 3$ km.

The results shown in Figure 3.2 indicate that below ~ 70 km the fields are symmetric around the z axis and that there is very good agreement between the vertical and non-vertical geomagnetic field solutions at these altitudes. The D -region ionosphere at such altitudes is non-magnetized due to very high rates of collisions between the charged and the neutral particles and the geomagnetic field direction can thus be safely ignored. The 2D model is thus sufficient at $z \lesssim 70$ km. At altitudes above ~ 70 km, however, the vertical and non-vertical geomagnetic field solutions start to deviate. The electric field structure at these altitudes are not axisymmetric and the peak electric fields are shifted in a horizontal direction. The shift in the \hat{x} direction (Eastward) is due to the almost horizontal geomagnetic field, or low dip angle ($I = 10^\circ$ in this case). The electric field being mostly vertical, the large angle between \vec{E} and \vec{B} introduces the Hall currents in the $-\vec{E} \times \vec{B}$ direction.

Beside the \hat{x} shift, the peak electric fields are also displaced in the $-\hat{y}$ direction (Southward). Further analysis of the solution of the fields in the southern hemisphere (not shown) shows a northward displacement therein. At the equator the electric field distribution becomes symmetric in the north-south direction at all altitudes. Thus the north-south shift of the peak electric field is an equatorward shift in both hemispheres, which is larger at lower latitudes. This result is related to the fact that, due to very high ionospheric conductivity along the geomagnetic field lines, the electrostatic potential can map along the magnetic field lines with very low attenuation. At the equator, instead of the shift, we obtain symmetrical and slowly decaying electric field profiles in the north-south direction.

The self-consistent conductivity profiles at the location of maximum electric fields at altitudes of 60–120 km are shown in Figure 3.3(a), where we compare the high-latitude (magnetic dip angle $I = 90^\circ$) and low-latitude ($I = 10^\circ$) profiles. The differences between these profiles are due both to the differences in the magnetic field

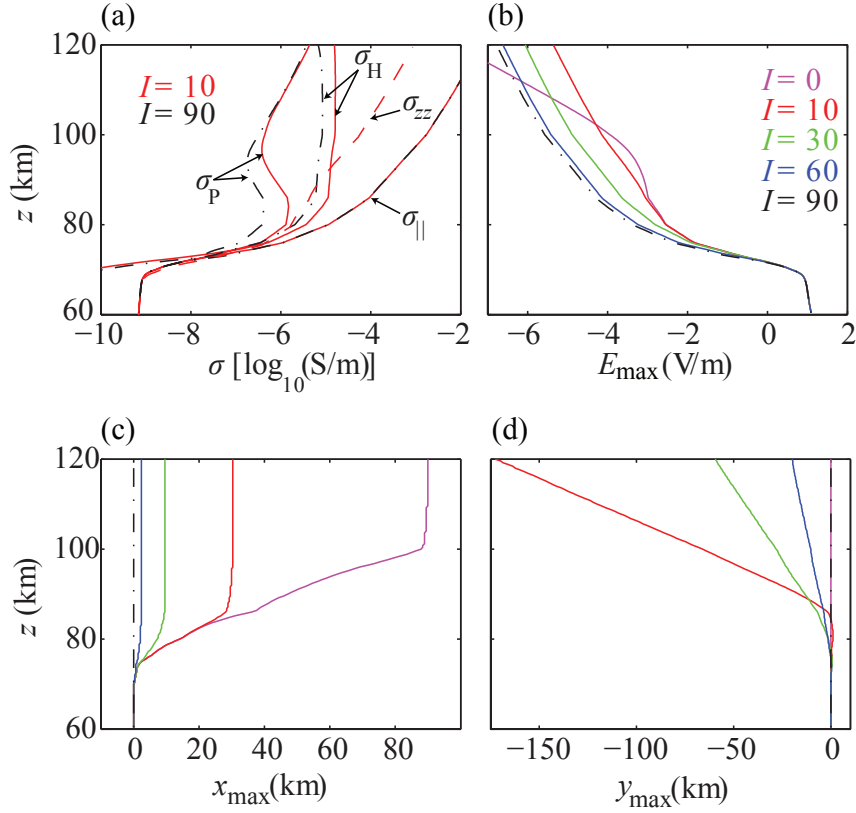


Figure 3.3: (a) The conductivity profiles at the location of E_{max} ; (b) maximum electric field; (c) eastward shift of E_{max} ; and (d) equatorial shift of E_{max} . The results shown are for 60–120 km altitude range for various magnetic dip angles.

strength and the non-linear change of the electron mobility with electric fields.

As mentioned in Section 3.1, the scale height of the conductivity profile in the \hat{z} direction, $\sigma_{zz} = \sigma_P \cos^2(I) + \sigma_{\parallel} \sin^2(I)$, determines the strength of the electric fields mapped to higher altitudes. For vertical geomagnetic fields at high latitudes $\sigma_{zz} \simeq \sigma_{\parallel}$ and the conductivity parallel to the geomagnetic field lines maps the fields to higher altitudes. At low latitudes, however, the conductivity profile in the vertical direction is more complicated, as shown in Figure 3.3(a) for $I = 10^\circ$ magnetic dip angle with the red dashed line. At altitudes below ~ 70 km $\sigma_P \simeq \sigma_{\parallel}$ and thus $\sigma_{zz} \simeq \sigma_{\parallel}$. At altitudes between 70–85 km σ_{zz} is controlled by both parallel and Pedersen conductivity terms. At higher altitudes, because $\sigma_{\parallel} \gg \sigma_P$, the term proportional

to the parallel conductivity dominates over the term proportional to the Pedersen conductivity and $\sigma_{zz} \simeq \sigma_{\parallel} \sin^2(I) < \sigma_{\parallel}$. Thus, the vertical conductivity σ_{zz} grows slower with altitude than σ_{\parallel} . This can be also seen in Figure 3.3(a), in the case of a non-vertical geomagnetic field. Therefrom, we observe that the vertical conductivity profile at altitudes higher than ~ 70 km has a larger scale height, and consequently the electric fields are mapped with less attenuation, which finds confirmation in the next panel. As shown in Figure 3.3(b), the magnitude of the peak electric field is significantly (up to 2 orders of magnitude) larger at lower latitudes than at the high latitudes. The larger peak electric fields have significant implications for the mesospheric and thermospheric processes and indicate a stronger upward coupling between the electrified thunderstorms and the high-altitude space environment at middle to equatorial latitudes than previously believed. At the equator ($I = 0$) the electric field has to penetrate across the magnetic field lines to higher altitudes which becomes harder at higher altitudes since the ratio of $\sigma_P/\sigma_{\parallel}$ decreases with altitude.

Figures 3.3(c,d) show the horizontal location of the peak electric fields at altitudes of 60–120 km, for different magnetic dip angles. For non-vertical magnetic fields, the peak electric field starts to shift eastward above ~ 70 km altitude, and the shift linearly grows with altitude until it reaches its maximum, after which it remains constant. The altitude at which the fields reach their maximum eastward shift depends on the magnetic dip angle and is higher for smaller dip angles. The equatorward shift of the peak electric fields also starts above ~ 70 km, linearly grows with altitude and is higher for lower dip angles. As discussed above, this result is consistent with the transverse electric field being efficiently “mapped” along the geomagnetic field lines. At the equator the electric fields are symmetric in the north-south direction and the peak electric fields are not shifted in this direction.

3.4 Discussion

3.4.1 Whistler duct formation

The whistler duct formation mechanism proposed by *Park and Helliwell* [1971] needs strong transverse (i.e., perpendicular to the magnetic field lines) electric fields in order to create density irregularities in the average lifetime of a thunderstorm. Our calculations show that thundercloud-generated electrostatic fields are mostly vertical in D region at all latitudes. This result is probably due to the fact that the source charges are well below in the troposphere and the atmospheric conductivity gradient is vertical. At lower latitudes these vertical electric fields have a larger component perpendicular to the geomagnetic fields and may thus be more effective in the duct generation mechanism proposed by *Park and Helliwell* [1971]. The transverse electrostatic fields at the non-polar latitudes, unlike those used by *Park and Helliwell* [1971], are not symmetrical around the \hat{z} axis. This asymmetry may impact the effectiveness of the fields in modifying the plasma density, as well as the spatial size and small-scale structures of the generated duct, which may also be calculated according to *Park and Helliwell* [1971] theory. The detailed analysis of the effectiveness of the fields at non-polar latitudes in the duct formation mechanism is the subject of future work.

3.4.2 Early/Fast VLF events

Electrostatic thundercloud fields have been proposed to persistently heat the ionospheric electrons, maintaining quiescent level throughout the duration of a thunderstorm [*Inan et al.*, 1996b]. Changes in the thundercloud charges by lightning discharges lead to heating/cooling above/below this quiescent level, which results in ionospheric modifications that can be seen as Early/Fast perturbations in VLF waves propagating in the Earth-ionosphere waveguide. The calculated stronger electrostatic fields at non-polar latitudes may lead to a stronger level of heating above the thunderclouds and thus a larger ionospheric modification due to lightning discharges than previously estimated. These larger modifications may render the quiescent heating

model more plausible [*Inan et al.*, 1996b]. This topic is investigated in more detail in the next Chapter.

3.4.3 Implications for sprites

As can be seen in Figure 3.3, the maximum electric fields at altitudes above ~ 70 km at low latitudes are larger than the maximum electric fields at the polar latitudes by up to 2 orders of magnitude. The electrostatic fields at lower latitudes also show an eastward and equatorward shift at altitudes higher than ~ 70 km. The eastward shift is qualitatively consistent with the results of *Tonev and Velinov* [2002]. These shifts displace the heating region above the thundercloud horizontally.

In addition to heating, electron density perturbations could be caused by electron convection or other mechanisms, such as chemical reactions neglected in this study which are important on long timescales comparable to the thundercloud charging time [*Gordillo-Vazquez et al.*, 2008]. These pre-conditioning effects could be related to the observations of large-scale optical structures in the diffuse halos [*Moudry et al.*, 2003] and eventually lead to sprite initiation [*Qin et al.*, 2014].

Although the results presented here do not include the sprite-producing post-discharge quasi-electrostatic fields, *Tonev and Velinov* [2005] estimated the eastward shift to be similar for the post-discharge fields in equatorial regions. Their analysis, however, does not self-consistently take into account the conductivity modification due to the electric fields. Further work on self-consistent analysis of the post-discharge lightning quasi-electrostatic fields at non-polar latitudes is needed to examine the effects of the magnetic field dip angle for these fields. If such calculations show a similar horizontal shift and stronger fields at high altitudes, the results would have extremely important implications on our understanding of the mechanisms responsible for the observations of horizontally displaced sprites [*Wescott et al.*, 2001; *São Sabbas et al.*, 2003] and the measurements and modeling of electric fields at the sprite initiation altitudes [*Hu et al.*, 2007]. This topic is further investigated in Chapter 5.

Chapter 4

Quiescent Heating of the Lower Ionosphere

As mentioned in Section 1.2.4, thunderstorms and lightning are known to cause perturbations to sub-ionospheric VLF transmitter signals, known as Early/Fast events, through direct heating and ionization of the lower ionosphere. Modifications of the sustained heating level of the ionosphere due to a lightning flash has been proposed by *Inan et al.* [1996b] as the causative mechanism of Early/Fast VLF events. However, the perturbations predicted by this mechanism have been much smaller than experimental observations of 0.2–1 dB or higher. In this Chapter, by using the improved thundercloud electrostatic upward-coupling model developed and described in Chapter 3, we show that perturbations are small, similar to *Inan et al.* [1996b], for vertical magnetic fields, but for lower dip angles the perturbations are significantly larger and may account for many Early/Fast events measured in the 0.2–1 dB range.

The material in this Chapter is submitted to *Geophysical Research Letter* for publication.

4.1 Introduction

Despite decades of study, the physical mechanism(s) responsible for Early/Fast VLF events are still under debate. *Marshall et al.* [2008] listed the candidate physical

mechanisms identified to date. These include (i) scattering from ionization patches created by the quasi-electrostatic (QE) field, and associated with sprite halos [*Inan et al., 1996a; Pasko et al., 1998*]; (ii) scattering from ionization columns manifested in sprites [*Dowden et al., 1994*]; (iii) scattering from ionization associated with the lightning electromagnetic pulse (EMP) and thus elves [*Mika et al., 2006; Marshall et al., 2010*]; (iv) scattering from ionization produced by the combined QE and EMP fields [*Moore et al., 2003*]; and (v) “sustained heating” of the lower ionosphere by thunderstorms below [*Inan et al., 1996b*].

Possibilities (i)–(iv) have received the most attention and scrutiny. Category (v), has been “ruled out” because *Inan et al. [1996b]* were only able to reproduce Early/Fast VLF perturbations of ≤ 0.1 dB using charge moments of 100–200 C-km. In contrast, Early/Fast VLF observations are typically 0.2–1 dB and sometimes higher. Larger charge moments result in ionization changes in the lower ionosphere, in which case the sustained heating mechanism becomes swamped by the QE and/or EMP mechanisms described above. Nonetheless, Early/Fast VLF events do exist even for small lightning discharges, as measured by peak current [e.g., *Marshall et al., 2006*].

4.2 3D QES Modeling

To calculate the thundercloud electric fields which lead to ionospheric heating, we use the 3D model developed and described in Chapter 2. The self-consistent solution for the fields and the conductivity modification is calculated by iteratively solving the charge conservation equation obtained as described below (Equation 3.1):

$$\nabla \cdot (\hat{\sigma} \nabla \Phi) = -\rho_s \sigma_{\parallel} / \epsilon_0 \quad (4.1)$$

where ρ_s , ϵ_0 , and Φ are thundercloud charge density, permittivity of free space, and electrostatic potential respectively and $\hat{\sigma}$ is the three-dimensional conductivity tensor for a magnetized plasma (see Equation 2.4). The contributions from both ion and electron conductivities are considered. The ion conductivity is obtained from previous experimental studies of the lower ionosphere [*Hale, 1984*]. The electron conductivity

is initialized from a given electron density profile which is then found self-consistently in the model (see Chapter 2).

The model uses a cartesian coordinate system with a non-uniform grid that has higher resolution closer to the center of the source charge distributions. The side boundaries are placed at a horizontal distance of 300 km from the charges and the top boundary is chosen at 200 km altitude above the ground.

While 2D models either neglect the geomagnetic field or must assume a vertical field, the 3D model described in the previous two Chapters takes into account the geomagnetic field magnitude and dip angle at different latitudes and altitudes. The inclusion of the dip angle is an important improvement compared to the previous models of thundercloud-ionosphere electrostatic interaction [*Pasko et al., 1998*], because at altitudes above ~ 70 km the electron gyrofrequency is larger than its collision frequency and the ionosphere behaves as a magnetized plasma. In Chapter 3, we showed that for a non-vertical geomagnetic field (non-polar latitudes) the electric fields at altitudes higher than ~ 70 km are larger than previously thought. These larger electric fields significantly heat the ionospheric electrons at middle and low latitudes and thus change their mobility and therefore the ionosphere conductivity.

The model neglects any electron density modifications for two reasons. First, the purpose of this study is to isolate the thundercloud E -field-driven electron heating effect and its contribution to the VLF transmitter signal perturbations observed as Early/Fast events. Second, the chemical reaction (ionization and attachment) processes need larger electric fields which only occur as the transient fields generated by strong lightning. Thus, fields of this magnitude are not available during weaker lightning processes on which we concentrate here. In this connection, it is worthwhile to note that Early/Fast VLF events have been documented to occur even in association with lightning discharges of relatively low intensity.

We assume thermal, chemical and electrostatic equilibrium state both before and after the lightning discharge. However, there may be chemical reactions occurring at the thundercloud charging time-scale and under the action of electric fields of relevant magnitudes. Moreover, the convection movement of ionospheric electrons due to the radial component of the electric fields might also change the electron

density configuration. The effectiveness and relevance of these effects are beyond the scope of this study and require further investigation.

4.3 Propagation Modeling

To estimate the VLF subionospheric signal perturbation resulting from these thundercloud fields and heating of the ionosphere, we use a 2D Finite-Difference Frequency-Domain (FDFD) model as described in detail by *Chevalier et al.* [2008].

Using a VLF transmitter signal with known frequency and power, the model solves Maxwell's equations in a cold, collisional, magnetized plasma. The model calculates the electromagnetic wave amplitude and phase, for all six field components, in the Earth-ionosphere waveguide and in the lower ionosphere with high spatial resolution over propagation distances of thousands of km. The model can take as inputs ionospheric parameters such as arbitrary electron density, collision frequency and background magnetic field profiles that can vary over the 2D simulation space, as well as ground parameters (conductivity and permittivity) that vary along the 1D propagation path.

In this Chapter, we solve for subionospheric VLF waves propagating over ~ 3500 km horizontal distance (x) and up to 110 km altitude (z), well above the reflection altitude of the transmitter signal (~ 85 km). The transmitter signal used for the simulations is at a frequency of 24 kHz, corresponding to the NAA transmitter in Cutler, Maine. The modified electron collision frequency determined from the 3D QES model is inserted into the propagation model ~ 2800 km from the transmitter. This scenario simulates the VLF transmitter path from NAA to VLF receivers in Colorado, with Early/Fast VLF events occurring ~ 700 km from the receiver; many such events were observed by *Johnson et al.* [1999] and others [e.g., *Marshall et al.*, 2006] with this arrangement. The solutions are found on a spatial grid with $\Delta x = \Delta z = 0.5$ km.

4.4 Results

In order to calculate the parameters of an ionospheric perturbation, namely the modified electron collision frequency, we employ the 3D QES model. We begin with a dipole charge distribution, with +20 C placed at 20 km altitude, and -20 C placed at 10 km altitude; this charge distribution is the same as the charge scenario in *Inan et al.* [1996b]. We calculate the electrostatic fields in the steady state using the QES model. We then repeat the model calculation after having removed the positive charge from 20 km altitude (a charge moment change ΔM_q of 400 C-km). These calculations result in two different 3D profiles of modified collision frequency, which are then input into the propagation model.

Note that this ΔM_q of 400 C-km does produce electric fields strong enough to exceed the threshold for dissociative attachment, but not strong enough to exceed the breakdown threshold (and thus produce ionization). However, the inclusion of associative detachment nulls the effect of attachment, since the electrons detach from O^- very quickly [Liu, 2012]. We observe that the electron density change due to this ΔM_q only persists for a few milliseconds. Furthermore, the results for the VLF signal perturbation shown below are approximately proportional to the charge moment change, which is in contrast with the highly non-linear dependence to be expected if the electron density change were the main mechanism. Namely, a ΔM_q of 200 C-km does not produce any attachment, but does produce perturbations about half as large as those shown below.

Similarly, two simulations are computed using the propagation model, first using the collision frequency associated with the dipole charge, and second with the monopole charge, the latter representing the charge configuration after the removal of positive charge via the lightning discharge. The difference between the resulting field calculations yields the VLF perturbation magnitude.

Figure 4.1 shows an example of the transmitter signal interaction with the thundercloud perturbation. The top panel shows a side view slab of the 24 kHz transmitter signal horizontal magnetic field component (i.e., perpendicular to the plane

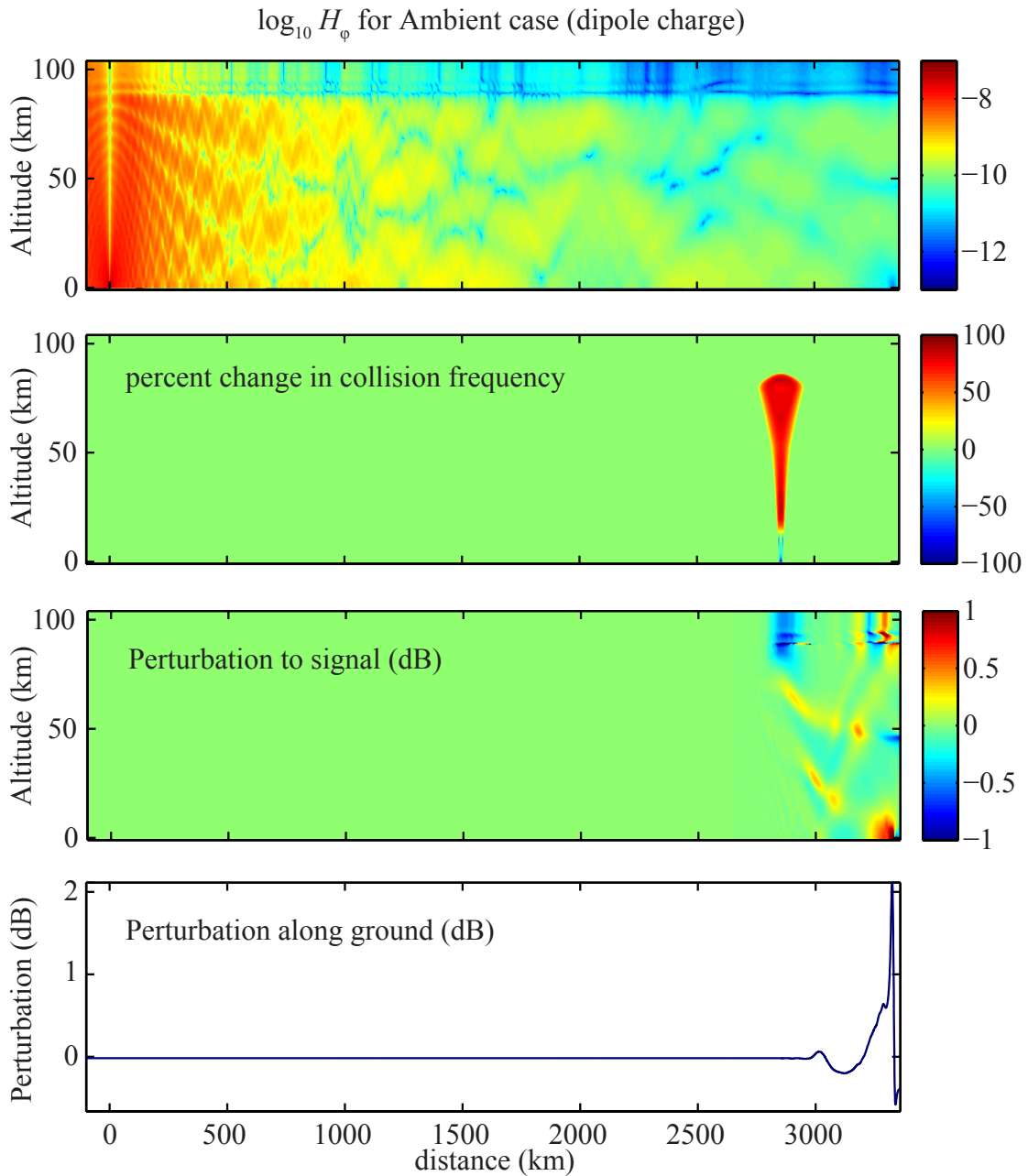


Figure 4.1: Example perturbation for $B_{\text{dip}} = 30^\circ$, ionosphere density profile e5 (see Figure 2.2a). Top: Unperturbed VLF wave, namely the horizontal magnetic field perpendicular to the image plane in 2D space. 2nd panel: difference in collision frequency due to monopole vs. dipole charge distributions. 3rd panel: Perturbed horizontal magnetic field after charge is removed from dipole leaving monopole. Bottom: perturbation measured along the ground.

of the page), injected in the Earth-ionosphere waveguide from the ground, propagating under and through an ionosphere prior to the thundercloud discharge (i.e., the dipole-related collision frequency profile). The relative wave magnetic field amplitude is indicated with the color scale. The results are consistent with other propagation models such as the Long-Wave Propagation Capability (LWPC) model [e.g., *Ferguson et al., 1989*]. The second panel shows the electron collision frequency change, in percent, between the quiescent heating level of a dipole and a monopole charge distribution; this change corresponds to the difference between the equilibrium state of the ionospheric heating before and after a +CG removing the upper charge distribution. For this simulation, the thundercloud location is assumed to be at a latitude corresponding to a 30° Earth geomagnetic field dip angle. The 3D QES model results show changes in quiescent collision frequency of $>80\%$ at mesospheric altitudes. The third and fourth panels of Figure 4.1 show the amplitude of the forward scattering of the VLF transmitter signal due to the thundercloud disturbances, in the 2D space and along the ground. The results show that depending on the location of the VLF receiver on the ground it can record an amplitude perturbation up to ~ 2 dB. However, note that this 2 dB peak occurs at a “null” in the transmitter amplitude pattern (top panel), which is an unlikely scenario for measured events. This position dependence effect is further addressed later in this section.

The results shown in Figure 4.1 can significantly vary with the ionospheric background conditions, the geomagnetic field direction, the thundercloud charge parameters, and the location of the thundercloud along the VLF signal path. Table 4.1 shows a summary of the model results for different ionospheric conditions and geomagnetic latitudes.

To take into account ionospheric variability, we consider five different electron density profiles, shown in Figure 2.2a. Profiles e1, e3, and e5 are taken from previous studies of subionospheric VLF transmission [*Pasko and Inan, 1994*; *Pasko et al., 1998*]. The WS1 and WS2 profiles are from theoretical studies of the ionosphere [*Wait and Spies, 1964*] with the VLF reflection height $h' = 85$ km and the “steepness” parameter $\beta = 0.5$ and 0.7 km^{-1} for WS1 and WS2, respectively.

The variation of the electrostatic fields with geomagnetic latitude was discussed

B-dip (deg)	ionosphere	$P(\Delta A > 0.1 \text{ dB})$	$P(\Delta A > 0.2)$	$P(\Delta A > 0.5)$	$\max(\Delta A)$
10	e1	0.85	0.62	0.13	0.64
10	e3	0	0	0	0.061
10	e5	0.86	0.72	0.44	15.0
10	WS1	0.85	0.62	0.13	0.64
10	WS2	0.89	0.68	0.28	1.20
30	e1	0.84	0.58	0	0.47
30	e3	0	0	0	0.058
30	e5	0.80	0.61	0.24	3.86
30	WS1	0.83	0.58	0	0.46
30	WS2	0.86	0.44	0.18	0.80
60	e1	0.75	0.13	0	0.27
60	e3	0	0	0	0.050
60	e5	0.56	0.35	0.082	1.50
60	WS1	0.75	0.13	0	0.27
60	WS2	0.75	0.21	0	0.44
90	e1	0.69	0.074	0	0.22
90	e3	0	0	0	0.042
90	e5	0.40	0.33	0.051	1.15
90	WS1	0.69	0.071	0	0.22
90	WS2	0.52	0.17	0	0.35

Table 4.1: Perturbation probabilities P for different magnetic dip angles and different ionospheres, for a 400 C-km charge moment change. The “ionosphere” column denotes the electron density profile as shown in Figure 2.2a.

in detail in the previous Chapter, where the main result was that the electrostatic fields generally penetrate higher into the ionosphere at lower latitudes. In Table 4.1, this variation is taken into account with four geomagnetic dip angles which represents the high, middle, and low magnetic latitude cases.

As shown in the bottom panel of Figure 4.1, the received VLF signal amplitude perturbation strongly depends on the location of the VLF receiver and its distance from the ionospheric disturbance. In effect, the large number of amplitude nulls and peaks exhibited along the signal path introduces a degree of randomness to the measurements, since ionospheric conditions at the time of a specific measurement are not precisely known. In order to take the randomness of the distance between the receiver and thundercloud in the observations into account, we use a probability

metric [Marshall and Snively, 2014] for which the probability of a received amplitude is defined assuming the receiver could be equally likely located anywhere behind the disturbance (with a uniform distribution over the area of the Earth). The results for such a probability metric, along with the maximum possible observed amplitude change (occurring at the null) are listed in Table 4.1.

The results at 90° magnetic latitude are consistent with Inan *et al.* [1996b]; for most of the profiles the maximum amplitude change from quiescent heating is 0.1–0.2 dB, with the exception of profile e5 which shows the largest possible amplitude change in all cases. Overall, at lower geomagnetic latitudes the effects of the thundercloud disturbances on the transmitter signal are stronger. This result is expected as the thundercloud fields at these latitudes can penetrate to higher altitudes (as explained in Chapter 3) and thus significantly change the electron collision frequency and thus the transmitter signal amplitude.

The perturbations also vary significantly with the electron density profile used. As seen in Figure 2.2a, density profiles e1 and WS1 are identical at altitudes above ~ 68 km, but differ at lower altitudes. The model results of the perturbations in Table 4.1 show that the transmitter signal perturbations are almost identical for these two density profiles, indicating that most of the signal perturbations are due to the transmitter signal interaction with the thundercloud disturbances at higher altitudes. This result is further supported by the results for profile e3, which has the densest electron density profile. For this case the thundercloud electric fields do not penetrate to altitudes higher than ~ 70 km, and thus the heating disturbances occur at lower altitudes and have minimal interaction with the VLF transmitter signal.

The effects of the electron density profile and the geomagnetic field direction is further illustrated in Figure 4.2 which shows the collision frequency perturbation due to different ionospheres (top) and magnetic field dip angles (bottom). For the top row, the dip angle is held constant at 30 degrees; for the bottom row, the ionosphere used is e5. The black dashed lines mark 80 km altitude to highlight the differences near the base of the *D*-region.

Results using profiles e5 and WS2 show the largest transmitter signal perturbation on the ground. These profiles represent tenuous *D*- and *E*-region ionospheric density

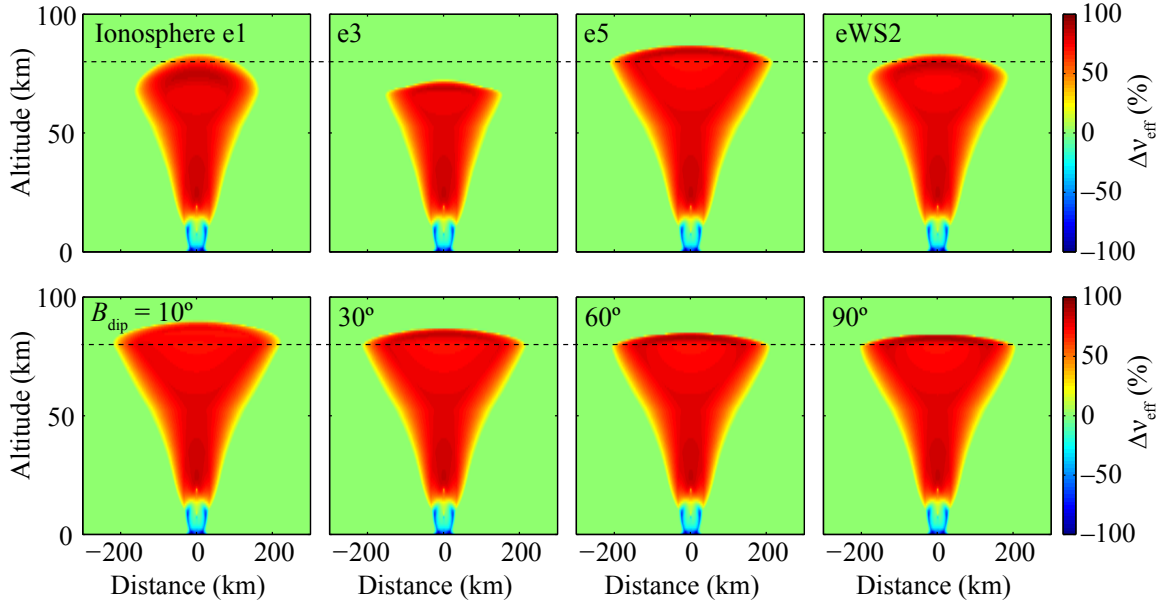


Figure 4.2: Electron collision frequency change, $\Delta\nu_{\text{eff}}$, associated with a +CG lightning removing the top positive charge layer. Top row: $\Delta\nu_{\text{eff}}$ due to ionospheric variability as represented by different electron density profiles (the geomagnetic dip angle is chosen at 30°). Bottom row: The effects of geomagnetic field dip angle in size and penetration altitude of the perturbation region (e5 electron density profile is used).

which accommodate the penetration of the thundercloud fields to higher altitude. Analysis of the heating region size as shown in the top row of Figure 4.2 also indicates that for these profiles the heating region has the largest spatial size up to ~ 150 km radius at the widest parts. These spatial sizes are consistent with the scattering pattern of the disturbance sizes found in the previous studies [Inan *et al.*, 1995; Johnson *et al.*, 1999].

4.5 Discussion

The results presented in the previous section support the quiescent heating model of Inan *et al.* [1996b] as a likely physical mechanism for Early/Fast VLF events. By considering the Earth’s magnetic field dip angle, we have shown that ionospheric heating alone is a sufficient mechanism to account for observations of many Early/Fast VLF

events. The results show large perturbations in the VLF transmitter subionospheric signals received on the ground that have a higher likelihood of detection at middle and low latitudes.

Based on the theory of *Inan et al.* [1996b], the thundercloud electric fields keep the lower ionospheric region in a quiescent heating level, which can be disturbed by a lightning discharge due to the slight modification of the charge distribution in the cloud. An important implication of the quiescent heating model is the source of the disturbance which controls the decay rate (the duration at which the signal returns to the pre-disturb level) of the Early/Fast VLF event. Based on this model, the decay rate is controlled by the interplay between the charging mechanism in the thundercloud and the relaxation time of the E field at different altitudes and is not controlled by the relaxation of the ionospheric electrons due to recombination. Thus, observations of Early/Fast VLF events can be used as a remote sensing technique for measuring the charging rate of the thundercloud.

Another implication of the quiescent heating model is in regard to the observations of Early/Slow events. *Marshall et al.* [2008] showed that Early/Slow events can be the cumulative result of hundreds of in-cloud lightning electromagnetic pulses creating a density hole through dissociative attachment at lower ionospheric altitudes. Alternatively, the quiescent heating model can explain these observations as the repetitive redistribution and removal of the thundercloud charge density which can change the ionospheric heating level. Such a scenario is consistent with observations of lightning activity associated with Early/Slow VLF events. As was noted by *Haldoupis et al.* [2006], lightning activity associated with Early/Slow events usually consists of a post-onset sequence of CG discharges coming from the same area and a large number of weaker but densely clustered sferics which are most likely ICs in the same area. The subsequent CGs and the in-cloud activity can each contribute to the modification of charge distribution and thus ionospheric heating which leads to the gradual change in the VLF transmitter signal amplitude and/or phase. The rise time of the signal is thus associated with the time span of the burst of lightning activity. The existence of some “pre-early” events where the VLF events start even before the causative CG lightning [*Haldoupis et al.*, 2006] suggests that the electron density disturbances

associated with sprite halos were not the cause of the VLF perturbations; rather, the in-cloud activity prior to the CG caused changes in the ionospheric conditions through the quiescent heating mechanism. The quiescent heating model is thus as effective as the lightning EMP model of *Marshall et al.* [2008] in explaining Early/Slow events. In fact, since the field intensities involved do not need to exceed the threshold for dissociative attachment, the quiescent heating based model requires much less lightning intensity than the lightning EMP model and is thus a more natural model for these events.

There has been a question of the frequency of the observations of Early/Fast VLF events based on the predictions of the quiescent heating model [*Haldoupis et al.*, 2006]. As shown in Figure 4.1 and Table 4.1, the VLF signal amplitude change observed at a receiver depends on the receiver location behind the disturbance. The largest signal perturbations are predicted when the lightning-associated heating of the lower ionosphere lies on the great circle path between the transmitter and the receiver. However, even for this case the received signal perturbation depends on the distance between the receiver and the disturbance in a non-linear way. Thus, large ionospheric disturbances might result in negligible received signal perturbations, below the accuracy of the receiver, and are left undetected. Moreover, the ionospheric electron density profile and the geomagnetic dip angle can greatly impact the effectiveness of the thunderclouds in influencing the VLF transmitter signals.

It is very likely that during strong cloud-to-ground lightning, a combination of the electron density changes and electron heating mechanisms contribute to observed Early/Fast VLF events. The quiescent heating model, therefore, is also consistent with observations of sprites in association with Early/Fast VLF events [*Haldoupis et al.*, 2004; *Mika et al.*, 2005], as well as observations of these events not associated with sprites [*Marshall et al.*, 2006].

Chapter 5

Lightning Quasi-Electrostatic Fields

5.1 Introduction

Sprites are transient mesospheric discharges due to strong cloud-to-ground (CG) lightning [*Sentman et al., 1995*]. The optical emissions from sprites start a few to tens of milliseconds after the return stroke of the causative lightning flash and can last up to tens of milliseconds. These emissions show complex morphological structures from narrow, vertically long, and highly structured ionization regions known as sprite streamers at lower altitudes [*Gerken et al., 2000*] to amorphous, diffuse, and horizontally extensive glow regions called sprite halos at higher altitudes [*Barrington-Leigh et al., 2001*].

Barrington-Leigh et al. [2001, 2002] with the use of intensified video and broadband array photometry, conclusively identified sprites to be the result of the quasi-electrostatic (QE) fields generated by a strong CG lightning consistent with the previous modeling results [*Pasko et al., 1997a; Veronis et al., 1999*] rather than the electromagnetic pulse (EMP) generated by the return stroke of the lightning.

Sprite halos and streamers are sometimes, but not always, observed together. If there is a direct connection between the two phenomena [*Luque and Ebert, 2009*], the non-ideal detection efficiency of the optical instruments can partly account for

the fact that they are not always observed simultaneously. Recently, based on high-speed camera observations of sprite events, many sprite streamers have been shown to initiate from within or the bottom of halo events. These observations indicate a strong connection between sprite halos and the initiation of sprite streamers.

Over the past two decades, extensive scientific experiments using both modeling and observational techniques have led to a better understanding of sprites. Specifically, there appears to be wide agreement on the main mechanisms responsible for halos. Currently, sprite halos are believed to be due to heating and ionization of the *D*-region ionospheric plasma by the QE fields of a lightning discharge. This ionization happens at high altitudes ($\sim 70\text{--}90$ km) where the electron density is high and the seed electron avalanches overlap with each other (Townsend multiplication) resulting in a smooth and diffuse ionization front [*Qin et al.*, 2011].

On the other hand, the generation mechanisms of sprite streamers, are not yet fully understood. *Qin et al.* [2011] attributed streamer discharges to the development of electron avalanches of the seed electrons below the sprite halos due to lower electron density from attachment processes. *Luque et al.* [2008], on the other hand, concluded that streamers are manifestation of Saffman-Taylor instabilities which leads to the increase of electron density only in certain locations.

Luque and Ebert [2009], using an adaptively refined grid, showed that the sprite streamers can naturally emerge from the bottom of a descending halo. In their model, the downward-propagating screening-ionization halo front sharpens and eventually collapses into a sprite streamer. However, these results have been questioned later by *Qin et al.* [2011] and have been associated with a numerical instability in the *Luque and Ebert* [2009] model.

Despite the qualitative agreement between modeling results of the sprite halos and streamers [*Pasko et al.*, 2013, and references therein] and the observations of the optical emissions from these events [*Gerken and Inan*, 2002; *Barrington-Leigh et al.*, 2002; *Pasko and Stenbaek-Nielsen*, 2002], many questions remain unanswered. Measurements of ELF radiation of lightning have been used to estimate the charge moment change of a lightning flash [*Cummer and Inan*, 1997], a key parameter in sprite generation. *Hu et al.* [2007] used the experimentally-measured change in the

charge moment of sprite-producing lightning flashes as an input into a 2D FDTD model of the electromagnetic fields generated from the lightning. For many of the sprite events, the modeled electric fields at the sprite initiation altitudes were below the conventional breakdown, making the creation of sprites theoretically impossible based on the models available at the time, in contradiction to observations of sprites at those altitudes.

To address this discrepancy, much attention has been paid to the effects of ionospheric electron density irregularities, resulting in successful explanation of some of the observations [Qin *et al.*, 2014]. For example, Qin *et al.* [2012], by using a spherically symmetric initial electron density inhomogeneity, estimated the minimum charge moment change for a +CG producing discharge to be ~ 200 C km. Some of the parameters used in their model, however, put uncommonly stringent limits on upper atmospheric ambient conditions. Namely, the reference altitude of the D-region electron density profiles needs to be higher than 90 km, and the peak electron density of the inhomogeneity at the sprite initiation altitude (~ 75 km) has to be very large ($> 2 \times 10^9 \text{m}^{-3}$). Using an inhomogeneity elongated in the orientation of the electric field might slightly alleviate the strict conditions. However, the frequency of the events with a charge moment change of 200 C km and observations of sprites with even smaller charge moment change of 120 C km [Hu *et al.*, 2002] indicate the insufficiency of the present models to explain the physics involved in the sprite streamer initiation.

Another discrepancy between the current models and experimental data of sprite streamers is shown in the observations of sprites that are horizontally displaced up to 50 km from the location of the causative lightning flash [Wescott *et al.*, 2001; São Sabbas *et al.*, 2003]. All existing models of lightning quasi-electrostatic fields, in a horizontally homogeneous ambient atmosphere, predict the strongest electric fields of the lightning at each altitude to be centered over the location of lightning discharge. Consequently, the most likely location of sprite events is also predicted to be immediately above the lightning discharge. More recently, some models have used ionospheric irregularities at horizontally displaced locations from the causative lightning and have shown that in the case of pre-existing ionospheric irregularities,

sprite discharges do not have to be centered over the lightning discharge. However, the streamer initiation regions, i.e., the volumes in which the electric field exceeds the streamer threshold, are smaller at these horizontally offset locations, which inhibits streamer growth.

In this chapter, we develop a 3D model of lightning quasi-electrostatic fields and the resulting sprite halos. The purpose of this work is to expand our understanding of sprites and thunderstorm upward coupling through inclusion of the effects which may be only modeled in 3D, such as non-vertical geomagnetic field and non-axially-symmetric horizontal irregularities of ionosphere.

5.2 Model

Our model extends the three-dimensional model explained in Chapter 3 to the post-discharge quasi-electrostatic fields. The fields are found from the solution of continuity and Poisson's equations (Equations 2.2 and 2.3). The ambient neutral and electron density, as well as the ion and electron conductivities are calculated as explained in previous Chapters. The non-linear electron mobility variation due to heating is calculated self-consistently [Pasko *et al.*, 1997a] and the changes in the electron density due to ionization (ν_i), attachment (ν_a) and detachment (ν_d) processes are taken into account using Equations 2.15 and 2.16 where the rates for these processes are taken from previous studies [Marshall, 2012]. The equations are solved on a three-dimensional structured grid in the Cartesian coordinate system with Dirichlet boundary conditions ($\Phi = 0$). For studies of these transient fields, we do not have to employ the more complicated boundary conditions given by Equation (3.2), since for our current purposes we are not interested in the upward penetration of these electric fields into the magnetosphere.

The side boundaries are chosen as far away as possible from the center of charge distribution with consideration of the trade-off between the accuracy and computational expense. The finite-difference equations are second-order in both temporal and spatial steps. They are discretized on a non-uniform grid in the horizontal direction with variable resolution which is higher closer to the center and smoothly decreases

toward the boundaries (see Chapter 3 for more details).

The temporal dynamics of the fields and the electrons is found from Equation 2.3 with a second order “predictor-corrector” scheme which requires tens of thousands of iterations to simulate a few millisecond of sprites development. This scheme, together with the large simulation domain, creates an extremely computationally-expensive simulation. Domain decomposition and parallelization is employed to find the solutions on a cluster of multiprocessor computers. For the results shown in the next section we put the side boundaries at 90 km lateral distance away from the center of charge distributions and the top boundary at 90 km altitude. We discretize the domain with $(215 \times 215 \times 180)$ points with a resolution of 359–7475 m, depending on whether we are at the center of the domain or close to the side boundaries. The equations are solved with 56 processing cores on a cluster of computers each with 64 GB of memory and 12 processors.

5.3 Results

5.3.1 QE Fields at Middle and Low Latitudes

Tonev and Velinov [2005], using an analytical model, predicted an eastward shift of up to ~ 100 km for the maximum quasi-electrostatic fields at altitudes of 75–95 km at equatorial latitudes. This shift of the calculated post-discharge electric fields was similar to the results of *Tonev and Velinov* [2002] for the electrostatic (i.e., pre-discharge) thundercloud fields. As was shown in Chapter 3, results of our 3D numerical model calculations were similar for the case of thunderclouds electrostatic fields [see also *Kabirzadeh et al.*, 2015]. The study of the lightning post-discharge quasi-electrostatic fields at low latitudes thus merits further investigation. Specifically, if lightning QE fields are shifted and stronger at lower latitudes, similar to the case of thunderclouds electrostatic fields, the implications of this result would lead to important revisions in our current understanding of sprites and halo initiation and dynamics.

Figure 5.1 shows our model results for the lightning quasi-electrostatic fields 0.5 ms after the start of the lightning discharge at low latitudes with 10° magnetic dip angle.

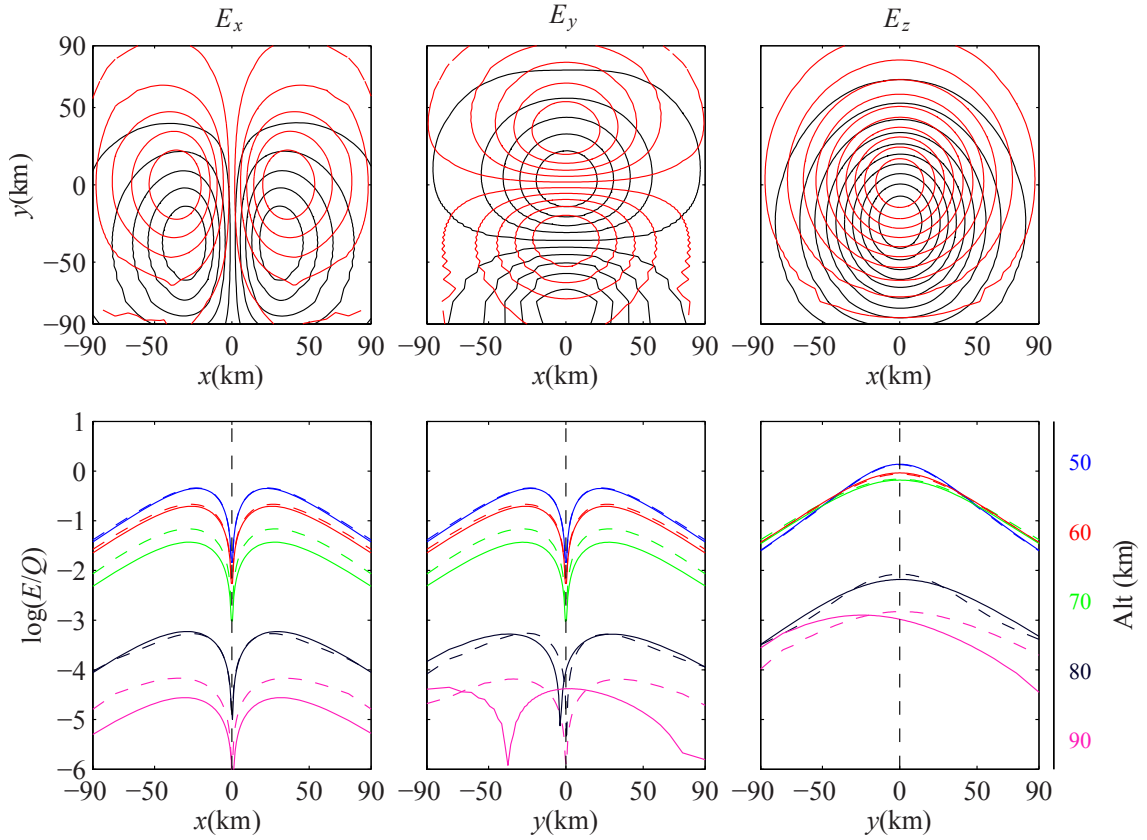


Figure 5.1: Quasi-electrostatic fields at low latitudes (10° dip angle) 0.5 ms after the lightning discharge. Top panels: electric fields contours at 88 km altitude (top view) taking into account the electron heating (red lines) or no heating (black lines). Bottom panels: electric field profiles at various altitudes considering electron heating (dashed lines) or no heating (solid lines).

The top panels illustrate the contour plots of the electric fields in the horizontal plane at 88 km. The red lines show the results when the effects of the electron heating due to the strong quasi-electrostatic fields are self-consistently included in the equations. The black lines show the quasi-electrostatic fields for the case when electron heating is not included in the equations, in which case the fields exhibit the horizontal shift and magnitude similar to the calculations of *Tonev and Velinov* [2005]. The bottom panels show the quasi-electrostatic field profiles at selected altitudes, normalized to the thundercloud charges, also for both situations, with and without heating. For

simplicity in our analysis, only the variation of the electron mobility due to heating was included. Other processes which change the conductivity of atmosphere, i.e., the ionization, attachment, and detachment processes, are neglected in this case, although results when these processes are included (not shown) are not significantly different.

The results of our calculations suggest that with the inclusion of electron heating by the quasi-electrostatic fields, the fields become more centered around the thundercloud charge dipole axis. The strong quasi-electrostatic fields of lightning discharges can heat the ionospheric electrons, increasing their effective collision frequency, ν_{eff} . The higher collision frequency of the electrons diminishes the effects of the Earth's background magnetic field as the gyrofrequency of the electrons, ω_{H} , becomes much smaller than the rate at which they collide with neutrals in the atmosphere. The same effect had been demonstrated previously, in models with a vertical geomagnetic field. Using a numerical model, *Pasko et al.* [1997a] demonstrated this increase in the electron effective collision frequency for various charge moment changes of +CG lightning and indicated that, regardless of the lightning charge moment, $\nu_{\text{eff}} > \omega_{\text{H}}$ below ~ 87 km [*Pasko et al.*, 1997a, Figure 13]. Therefore it appears that the results of *Tonev and Velinov* [2005] are due to the limitation of their model in self-consistently calculating the electron heating.

There is one caveat in the conclusions given above: the calculated horizontal shifts in the electric fields are dependent on the choice of the altitude of the upper boundary of the simulation region. Namely, they are largely diminished even for the electrostatic thundercloud fields if a lower upper boundary is chosen. Further analysis reveals that if one selects the upper boundary of the simulation at 90 km altitude, same as in our model described here and also in *Pasko et al.* [1997a], even the shift in the thundercloud electrostatic fields decrease significantly. This result could be due to the Dirichlet boundary condition used ($\Phi = 0$) at the top boundary instead of the condition in Equation 3.2. The evidence of the effect of the upper boundary choice can be seen from Figure 5.1 where even in the case of no heating the calculations do not show a significant eastward shift of the fields. Thus, for further quantitative study of the structure of the mesospheric quasi-electrostatic fields of the lightning discharges, a higher upper simulation boundary should be chosen (for

example 120 km similar to *Tonev and Velinov [2005]*). Given the numerical scheme used here and its stability criteria, such a selection is not computationally feasible at the moment. Unconditionally stable numerical schemes or methods for removing the stiffness of the quasi-electrostatic system of equations, such as those introduced in Section 2.7, are needed to resolve this problem. The development of such new schemes is left as the subject of future work. Nevertheless, our comparative analysis of the cases with/without self-consistent heating for a given boundary selection still represents a valid indication of the role of heating in minimizing the shift due to the enhanced collision frequency.

5.3.2 Sprite Halos in a Neutral Atmosphere Perturbation

As explained in Section 5.1, the process of sprite streamer initiation is still not fully understood. Recently, *Qin et al. [2014]*, using optical observation of sprites at 16,000 frames per second in combination with a numerical model of sprite halo, argued that sprite steamers are initiated from ionospheric electron irregularities. The origin of these pre-existing irregularities have been associated with previous sprite discharges at the same location or the electron density columns remaining from a previous meteor trail. However, the ionization columns required for numerical studies of the streamer initiation need to be ~ 2 – 5 orders of magnitude larger than the background electron density. The initiation of the sprite streamers thus from a previous sprite body has several unresolved problems. First, this mechanism might only explain a few of the existing observations, but cannot be the dominant mechanism of sprite initiation due to the fact that observations of sprite events do not indicate that sprites happen at one location every time. Second, this mechanism requires that the electron irregularities from the previous sprite body last for a very long time, namely about several tens of minutes, much larger than the reasonable relaxation time of the electron irregularities in *D*-region ionosphere.

Initiation of sprite streamers from the trail of an ablating meteor has been considered from the early years of sprite research [*Symbalisty et al., 2000; Zobotin and*

[Wright, 2001](#)]. However, this mechanism was discarded due to the very low probability of coincident meteor and sprite events. The current estimate for the flux of the meteors (including micro-meteors) entering the Earth atmosphere gives at most 5% chance of one meteor in the entire region of the sprite halo events [[Qin et al., 2014](#)]. Considering the lower chance of streamer initiation away from the center of the sprite halo and the fact that there are often several simultaneous streamer events initiating from a descending halo, meteors seem even more unlikely to be capable of creating electron density irregularities. Despite the above mentioned unresolved questions about the origin of the electron density irregularities, this mechanism remains one of the important candidates of streamer initiation processes for the sprite events.

In this section, we consider another mechanism for creation of sprite streamers first proposed by [Pasko et al. \[1997b\]](#). In this mechanism, it is the irregularities in the *neutral* atmospheric density that create suitable conditions for the initiation of sprite streamers. Recent numerical and observational studies of sprites indicate strong evidence of this mechanism as the driving process of streamer initiation in sprite events [[Liu et al., 2015](#)].

Thunderstorms are known to generate atmospheric neutral density fluctuations called gravity waves. These fluctuations typically have a wavelength of a few tens of kilometers and can propagate to high altitudes where the wave amplitude increases with height [[Hines, 1960](#)]. The upward propagating gravity waves can reach mesospheric regions in tens of minutes where they can break into smaller structures of 5–20 km wide due to instabilities [[Snively and Pasko, 2003](#)]. These small-scale structures can further lead to even smaller turbulence-driven structures [[Yamada et al., 2001](#)]. Due to the strong dependence of the air breakdown limit on the local neutral density, the modulation of the air neutral density can lead to the clustering of sprites as further explained below.

Figure 5.2 compares the result of our numerical model with recent high-speed observations of sprite streamer inception from sprite halos. The model results illustrate the mesospheric state at 10 ms after the removal of the thundercloud upper positive charge of 100 C by a +CG in the presence of a gravity wave. The results show good qualitative correspondence between the structure of the electron density

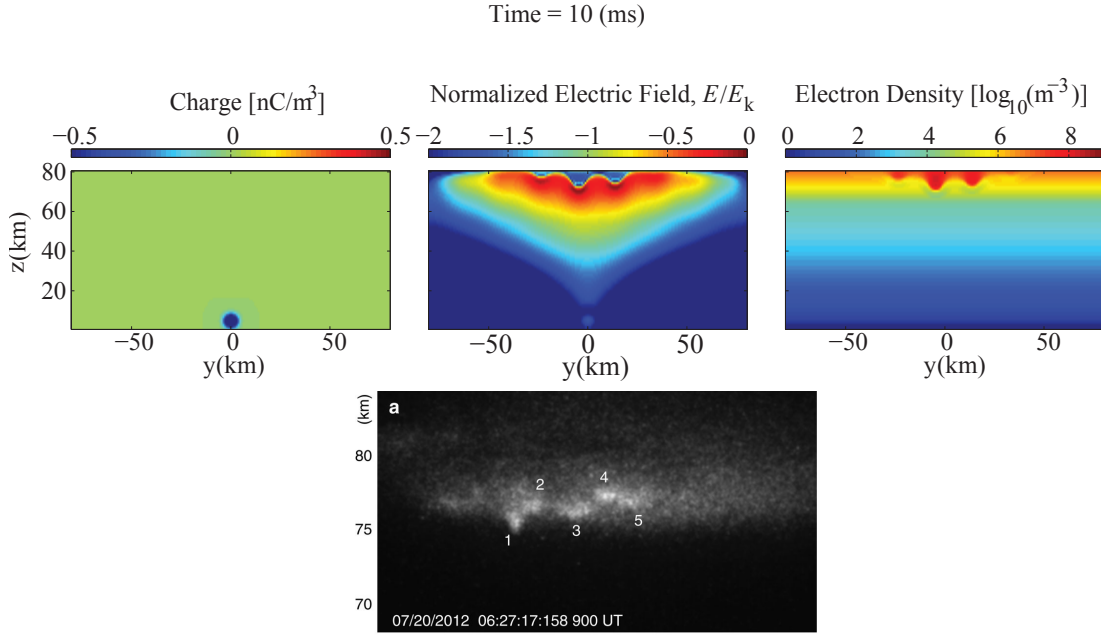


Figure 5.2: Top: simulation results of sprite halos in the mesospheric neutral density fluctuations caused by thunderstorm driven gravity waves. Bottom: high-speed observations of streamer initiation from sprite halos reported by [Qin et al. \[2014\]](#).

enhancements and the observed localized high-intensity emissions within the sprite halos (indicating strong ionization spots from which sprite streamers developed). The effect of the gravity wave is incorporated into the model as a fluctuation of the background neutral density increasing with height:

$$N_{\text{gw}} = 0.15N \sin(2\pi y/\lambda) e^{(z - z_0)/H}$$

The spatial period of the gravity wave is chosen to be $\lambda = 20$ km in the north-south direction (y). The amplitude of the waves increases from the ground exponentially with a scale height of $H = 12$ km (which is approximately double the neutral density scale height), so that at $z_0 = 80$ km the waves have an amplitude of 15% of the background neutral density N , which is within the theoretical predictions for these waves [[Hines, 1960](#)].

The fluctuations of the background neutral density provides periodic structuring of

the reduced electric field (E/N or, equivalently, E/E_k), which is inversely proportional to the neutral density. Thus, the troughs of the gravity waves create hot-spots for the initiation of the sprite streamers inside the sprite halos, as can be seen from Figure 5.2. Therefore, the structuring of the background neutral density leads to structuring of the sprite events and may thus manifest as a quasi-periodic cluster of sprites with the period equal to the horizontal period of the perturbing gravity wave. This result is in good agreement with the observations of sprite discharges, which usually show quasi-periodic clusters of streamer discharges spatially separated by a few to tens of kilometers.

In the current analysis we used a planar gravity wave front, similar to the fronts usually used in the studies of traveling ionospheric disturbance events originating from auroral ovals during magnetospheric substorms [*Davis and Da Rosa, 1969*]. We point out that, unlike the previous 2D models [*Pasko et al., 1997b; Liu et al., 2015*], our 3D model can incorporate any arbitrary shape and structure for the gravity waves. More complicated structuring of the background neutral density can be used, such as the structures expected from turbulent breaking of the gravity waves. It is important to note that if clustering of sprite events is due to the background neutral density fluctuations, observations of sprites can be used as an important remote sensing tool of the mesospheric densities above thunderstorms.

Chapter 6

Thunderstorm and Lightning Evolution

6.1 Introduction

Thunderstorms are an important part of the Earth's global electric circuit and are believed to be the drivers for the maintenance of the fair weather downward directed current density of about -2×10^{-12} A/m² [*Volland, 1984*, p. 15]. The development and evolution of thunderstorms is the result of various thermodynamical, microphysical, kinematical, and electrical processes with a wide range of spatial and temporal scales from micrometer to many kilometers and from microsecond to hours, respectively. To understand this powerful natural phenomenon, one needs to know the details, relative importance, and contributions of the processes involved. Moreover, these processes are often not independent and exhibit complex interactions that must be measured or simulated concurrently in order to be understood. For example, as explained in Section 1.2.1, the electrical processes are closely related to the cloud dynamics, wind patterns, local temperatures, local water content, etc.

Experimental and laboratory measurements of the phenomena related to the thunderstorms have been performed from the early years of their studies. The invention of the cloud chamber by C.T.R. Wilson to study the high-energy particles during his work on atmospheric ions (for which he was awarded the Nobel Prize in 1927) is an

example of these studies. Laboratory measurements, however, are mostly limited by our understanding of and the ability to reproduce the thunderstorm environment and the mechanisms involved. In-situ measurements of particles and fields inside thunderstorms can provide insight about various processes, but cannot provide a complete global picture of the storm evolution and are constantly challenged by the hostile environment of the storms and the limited sensitivity of the instruments. In the experimental studies of thunderstorm electrical activities, remote sensing techniques have been used extensively. For example, the radiated electromagnetic fields from lightning discharges have been used to obtain data such as the location of lightning channel ground attachment point, the temporal and spatial development of lightning leaders, the return stroke speed and peak current, and the charge moment change associated with the lightning discharge.

In this work, we mainly focus on the electrical activity of the storms, specifically on the role of the lightning discharges. Of particular importance for the study of the electrical activity of thunderstorms is the knowledge of the thundercloud charge structure and its variation in time and space. Unfortunately, direct measurements of the charge structure within the entire storm system is currently impractical, as available techniques involve only a local measurement at a specific time. Instead, ground and in-cloud measurements of the electric fields produced by the charges have been used to estimate the charge layer structure of the storms assuming that there is a horizontally uniform charge layer at each altitude [*Marshall et al.*, 1995a,b; *Stolzenburg et al.*, 1998a,b,c]. Multi-point observations of the ground electric field changes produced by intracloud lightning were used to propose a dipole structure of the charges in thundercloud with the main positive layer above the main negative layer [*Wilson*, 1921; *Wilson et al.*, 1929]. Subsequent observations confirmed this general picture of the charge structure, and some of them indicated the presence of a smaller positive layer below the main negative layer [*Simpson and Scrase*, 1937].

The origin of the lower positive layer is still under debate. Nevertheless, there are several proposed theories and mechanisms to explain the creation of such a layer. The collisional charging mechanism explained in Section 1.2 is one of these theories which seems the most plausible. An alternative theory is that these charges are created

by the negative cloud-to-ground ($-CG$) lightning [*Marshall and Winn, 1982; Holden et al., 1983*]. According to this theory, the positive charge, which appears during the discharge on the lightning channel and leader branches, is deposited close to the main negative layer and can be transferred to the precipitating particles. After several lightning flashes a positive charge layer is created below the main negative layer.

However, theoretical and numerical modeling of thunderstorms have not been able to confirm the above theory. The primary reason for this result is the fact that in all models of thunderstorm electrodynamic and lightning activity, a positive lower charge layer is used as the necessary condition for the creation of negative CGs. In other words, based on the current models of the thunderstorms only a tripole charge structure (with a lower positive charge layer) can create a cloud-to-ground lightning discharge [*Mansell et al., 2005; Krehbiel et al., 2008*, and references therein].

However, due to the computational limits most of these models are able to target only a subset of the physics involved. For example, *Mansell et al. [2002]* developed a model including the extensive parametrization of electrification mechanisms, combined with a stochastic dielectric breakdown model to investigate the conditions for lightning generation. The dielectric breakdown model used does not include the physics of the lightning and thus cannot accurately calculate the modifications of the thundercloud charge due to a lightning discharge. Moreover, almost all of the charge structures, which were simulated based on the theoretical charging mechanism used in their model and in a later study by *Mansell et al. [2005]*, predicted a lower positive charge layer. Thus, the modeling results of *Mansell et al. [2002, 2005]* could not be used to study the creation of the lower positive charge layer by lightning discharges.

Krehbiel et al. [2008] used a simpler charging mechanism using constant charging currents, combined with a similar dielectric breakdown model to study upward lightning generated by thunderstorms. Their 2D azimuthally symmetric model prevented them from capturing the spatial structure of the lightning-induced charges inside the thundercloud. To overcome this problem, *Krehbiel et al. [2008]* chose to remove 50% of the charge layer (homogeneously distributed over the entire charge layer) after a CG discharge or reduce both charges by 50% of the smaller charge layer after an IC

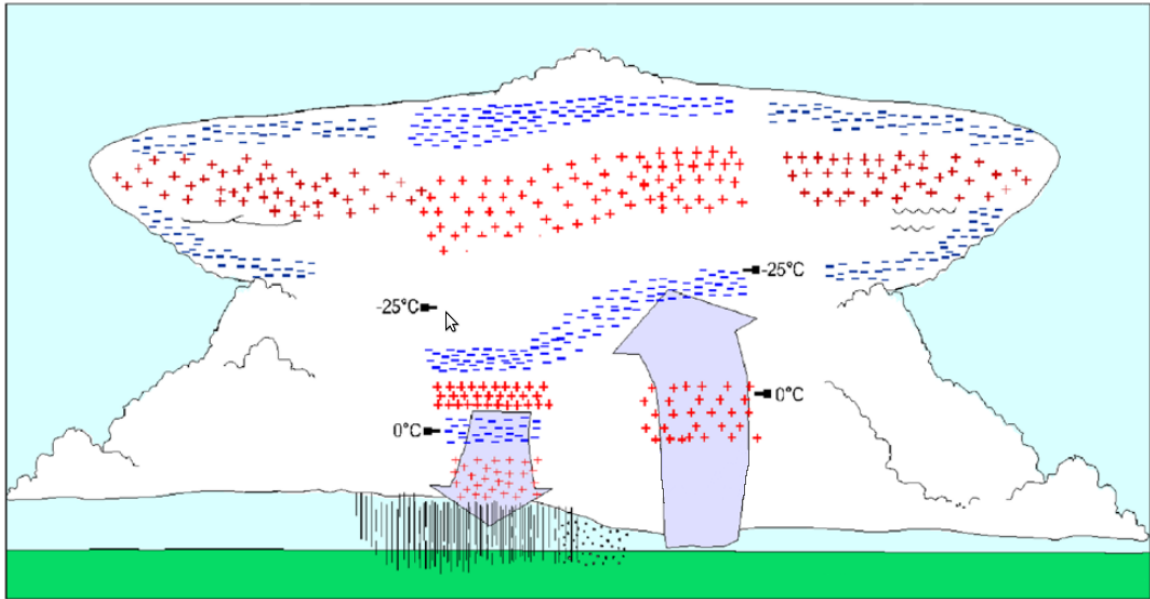


Figure 6.1: Schematic model of charge distribution within an isolated supercell thunderstorm (adapted from [Stolzenburg et al. \[1998c\]](#)).

discharge. As explained later in Section 6.4, this approach and the lack of a physics-based model of lightning discharges limits the applicability of [Krehbiel et al. \[2008\]](#) model for lightning studies.

6.2 Model for Thunderstorm and Lightning Evolution

Any thunderstorm electrodynamic model needs three main components: 1) a thundercloud charging model, 2) a model of the large scale thundercloud fields, and 3) a lightning discharge model. In this section we explain the details of each model and the integration of the models.

6.2.1 Calculation of Charges and Electric Fields

Figure 6.1 shows the general charge structure of a mature, isolated thunderstorm obtained from 49 balloon sounding of various clouds [[Stolzenburg et al., 1998c](#)]. The

illustrated charge distribution has a very complex structure and does not resemble a dipole or tripole structure that is often assumed in theoretical studies. The complex charge structure of a real thunderstorm could lead to various types of lightning activity. Using a complicated charge structure such as that shown in Figure 6.1 in any simulation makes it difficult to interpret any observed features in the lightning activity and to understand the underlying physics and electrodynamics of thunderstorms responsible for different kinds of lightning activity.

For simplifying the interpretation of our results and in order to test various hypotheses regarding the effects of lightning discharges on thunderstorm electrical evolution, we use a model similar to [Krehbiel et al. \[2008\]](#) for the cloud charging mechanism. The model ignores the microphysical activities in the cloud that separate the charged particles on small scales (i.e., the mechanisms explained in Section 1.2.1) and considers only the bulk electrical currents inside the cloud during the accumulation of charges. We further assume a constant charging current inside the cloud, consistent with the remote sensing observations of the thunderclouds [[Krehbiel, 1986](#), p. 102]. With this simplified thunderstorm charging model, any observed feature from the model can be distinctly attributed to interactions and modifications of the charge structure by lightning discharges.

With a constant current which gives a constant rate of charge build-up inside the cloud, the quasi-electrostatic fields are developed in the environment. The 3D parallel model developed for upward electrodynamic coupling of thunderstorms, as explained in previous Chapters, is employed to calculate these electric fields and currents. In this case, the quasi-electrostatic equations need to be modified since we do not know the variation of the charges with lightning discharges during the thunderstorm life time. In fact, the primary objective of our study is to determine this variation so that the variation itself cannot be used as an input to the model. The new equations with a constant charging current are as follows:

$$\frac{\partial \rho_{\text{tot}}}{\partial t} = \nabla \cdot (\hat{\sigma} \nabla \Phi - \vec{J}_{\text{charging}}) \quad (6.1)$$

$$\nabla^2 \Phi = -\frac{\rho_{\text{tot}}}{\epsilon_0} \quad (6.2)$$

where ρ_{tot} is the total charge density including the source charges developed on the cloud particles and the screening charges accumulated close to the boundaries of the charge layers in the cloud. $\vec{J}_{\text{charging}}$ represents the constant currents that build up the charge distributions inside the cloud. The above equations are solved at each time step to obtain the electric fields (Equation 6.2) and the updated charges and currents (Equation 6.1). For the purpose of this chapter, the high-altitude coupling of the thunderstorm can be neglected and the top boundary of the simulation is chosen at ~ 40 km. Due to the high collision frequency of the electrons, the conductivity tensor at this altitude range is mainly diagonal and is dominated by the ion conductivity contribution which is assumed to be independent of the field and therefore to remain constant at each altitude.

6.2.2 Lightning Discharge

In order to accurately calculate the modification of the cloud charges due to a lightning discharge we use a time-domain fractal lightning (TDFL) model developed based on the basic physical principles in combination with some empirical data on leader propagation [Carlson, 2009; Liang, 2014; Carlson et al., 2015]. The TDFL model takes into account the small-scale processes involved in the development and propagation of the lightning structures. The lightning and leader channels are simulated with a thin core of ~ 5 mm wide and a corona sheath of ~ 5 m around it. The core electrodynamics are updated by solving the electric field integral equation [Jackson, 1999, p. 246–248], which relates the currents and charges on the lightning channel to the electric field (by a convolution with Green’s function). At each time step, the thermodynamics of the lightning channel, such as its temperature and pressure, are calculated self-consistently for the ion, electron, and neutral gas inside the channel. The energy transfer between the sheath and the core is taken into account during the simulation.

The growth and development of the lightning channel is taken into account with a probabilistic approach. In this approach, all possible positions for which the electric field exceeds the leader propagation threshold are considered as shown in Figure 6.2a.

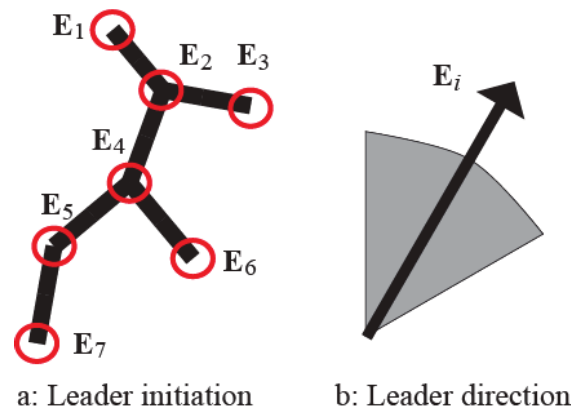


Figure 6.2: Probabilistic model of lightning leaders propagation (adapted from [Liang \[2014\]](#)).

The probability distribution function obtained for the candidate locations for leader growth is further weighted by the field strength at each location. At each time step, a number of leaders are randomly chosen and can simultaneously grow (the number of leaders that can simultaneously grow is an input of the model). The growth is limited to a cone with an angle around the direction of the electric field as shown in Figure 6.2b which is calculated and used as an input before the simulation of this growth begins.

6.2.3 Model Integration

Figure 6.3 describes the computational flow of the three components of the model working together. The model starts by calculating the charge distribution and the resulting fields generated by the charging currents. At each time step, the electric field in the domain is checked against the threshold for initiation of a lightning discharge as explained later in this section. This process repeats as long as the electric fields are too weak for a lightning discharge to initiate. Given enough time, the charging currents lead to accumulation of significant amount of charge in the cloud so that, eventually, at one (or more) location in the simulation domain, the electric field exceeds the threshold for initiation of lightning.

When the condition for lightning initiation is met, the TDFL model simulates

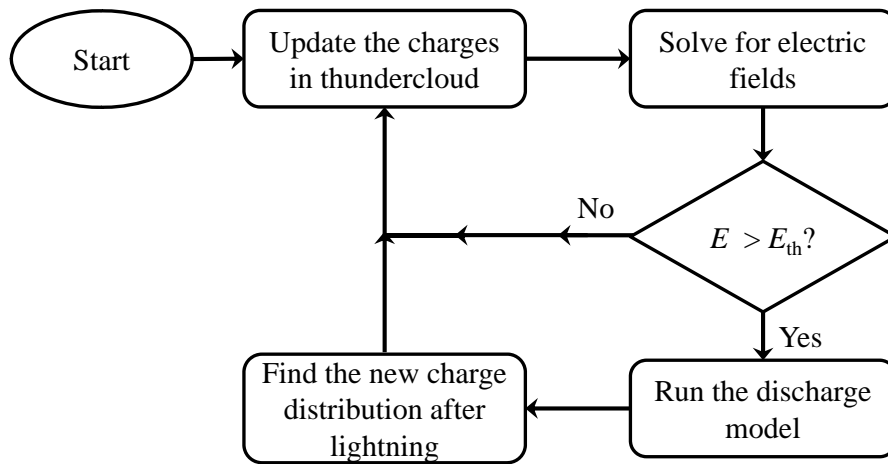


Figure 6.3: Thunderstorm electrodynamic model integration and the computational flow of the model.

the lightning discharge with the given initiation point and background charge distribution, external electric fields, and neutral densities. In case there are multiple locations at which a lightning discharge can initiate, our model selects one of them randomly and simulates the lightning discharge from that location. The lightning discharge propagates until the electric fields on the lightning channels are weaker than the threshold for the leader initiation (which is less than the lightning initiation threshold). When all the lightning leader activities terminate and reach equilibrium, the electric charges which have been induced on the lightning channel are interpolated onto the structured grid of the background charge distribution and are passed to the thunderstorm model. The thundercloud model proceeds to calculate the cloud electrification after adding the lightning-induced charges to the cloud charge distribution, until the lightning initiation threshold is exceeded again, and so on. The cycle is repeated until the model is terminated by the user or until pre-determined simulation time is reached.

The choice of the lightning initiation threshold in the above procedure is a key parameter input of such a model of thunderstorm electrostatics. The lightning initiation process, nonetheless, is still not well understood and remains an open question in thunderstorm physics. The conventional electric breakdown of the atmospheric gas

at the altitudes of lightning initiation requires electric fields in excess of ~ 3 million volts per meter. However, in-cloud observations of the electric fields associated with lightning discharges indicate values that are ~ 3 – 10 times smaller [Marshall and Rust, 1991; Marshall *et al.*, 1995a]. Numerous experimental [Marshall *et al.*, 1995a, 2005; Stolzenburg *et al.*, 2007] and theoretical [Wilson, 1925; Gurevich *et al.*, 1992; Gurevich and Zybin, 2001; Dwyer, 2003, 2005] studies have indicated the initiation process to be related to the electron runaway breakdown process. The electric field required for this breakdown process is about an order of magnitude smaller than the conventional breakdown and is close to various observations of lightning initiating electric fields.

Following the thunderstorm electrodynamic models cited above, we also use the field which is close to the runaway breakdown threshold electric field as the threshold for lightning initiation in our model. This field is altitude-dependent and may be calculated as

$$E_{\text{th}}(z) = E_0 e^{-z/z_0} \quad (6.3)$$

where $E_0 = 302$ kV/m is 40% higher than the runaway breakdown at sea level. This value provides very good empirical estimate of the measured electric field from balloon-borne sounding of the thunderclouds at the time of lightning initiation [Krehbiel *et al.*, 2008]. In Equation 6.3, z represents height in kilometers above the sea level and $z_0 = 8.4$ km is the runaway breakdown atmospheric scale height.

6.3 Results

Figure 6.4b–d illustrates snapshots of a simulated intracloud lightning in a downward dipole external electric field (schematically shown in Figure 6.4a not to true scale) initiated between the two charge layers. Here the negative leaders (blue) propagate upward in the opposite direction of the electric fields toward the positive charge distribution and positive leaders (red) propagate downward toward the negative charge distribution. The thundercloud charge distribution of ± 100 C is distributed with a Gaussian profile in radius and height. The lightning channel is simulated with 100 m long segments, which correspond to the leader steps.

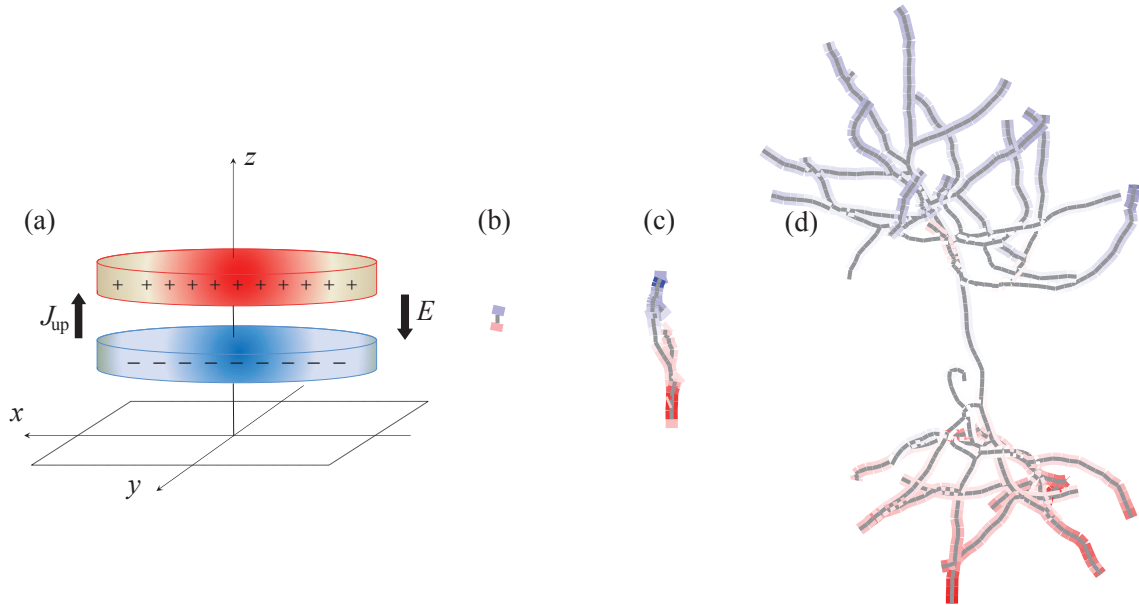


Figure 6.4: Lightning simulation in a dipole thundercloud field using the TDFL model of [Liang \[2014\]](#).

Figure 6.5 shows the dipolar charge structure (bottom panels) and the ratio of electric field over the lightning initiation threshold (top panels). The x axis is the horizontal distance in km from the center of the storm and the vertical axis z is the height in km. Each panel shows the xz slab from the middle of 3D domain (at $y=0$). In this simulation, a dipolar charge structure is used where the charge is distributed with a Gaussian profile in the horizontal and vertical directions with a radius of 20 km and a thickness of 3 km for each layer. The center of the main negative and the main positive layers are chosen at altitudes of 5 km and 10 km respectively. The thunderstorm charges and the electric fields are calculated on a uniform structured grid with $\Delta x = \Delta y = \Delta z = 1$ km.

The left-hand panels show a snapshot of the thunderstorm state at 67 minutes after the start of the charging currents and before the first lightning was initiated. The Figures show the two charge layers that are built due to the charging currents. Strong electric fields close to the lightning initiation threshold are found between the two charge layers. The first lightning discharge initiates between the charge layers and

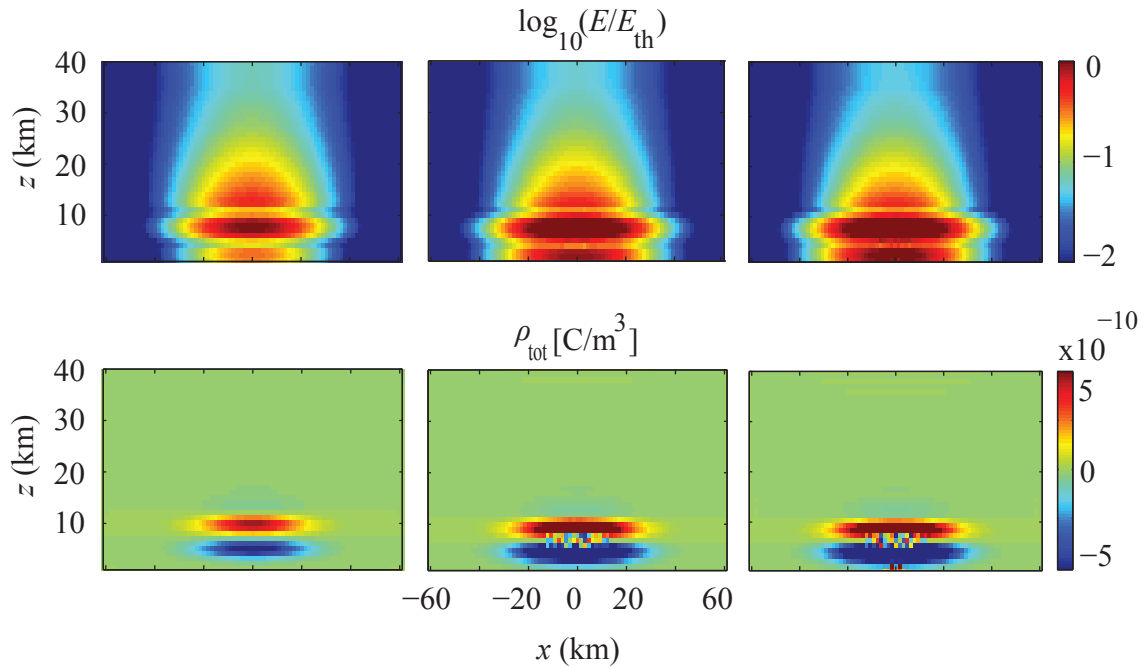


Figure 6.5: Thunderstorm electrodynamics and lightning activity. Electric field (top) and charge distribution (bottom) state of the thundercloud at 67 minutes (before the first lightning), 222 minutes (after an intense IC activity), and 285 minutes (after the CG activity) from left to right respectively.

develops into an IC discharge. The middle panels in Figure 6.5 show the thunderstorm state at 222 minutes after a period of strong IC activity followed by a period of weaker IC activity. The modification of the thundercloud charge distribution due to the lightning discharges can be seen between the two charge layers. Strong electric fields are developed between the two charge layers as well as below the main negative layer. The right-hand panels in Figure 6.5 show the thunderstorm state after some $-CG$ discharges have occurred. The electric field plot shows strong electric field below the main negative layer that is capable of initiating a lightning discharge. These fields initiate a lightning discharge below the main negative charge layer that can attach to the ground.

The temporal and spatial evolution of the lightning discharges for the simulated thunderstorm is shown in Figure 6.6. After about an hour of charging of the cloud,

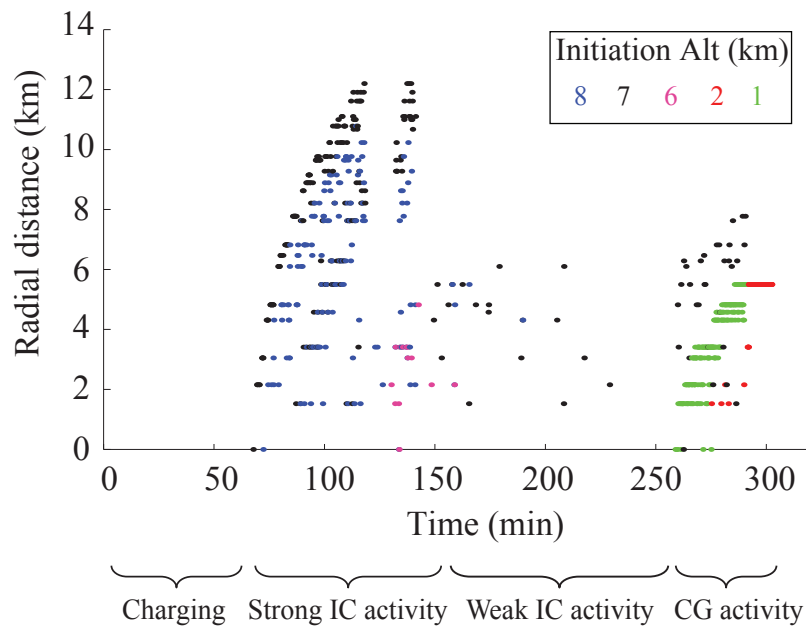


Figure 6.6: Lightning evolution and various phases of thunderstorm electrical activity.

lightning activity starts with an intracloud discharge initiated at 7 km above the ground between the two charge layers and at the center of the charge distributions which corresponds to the strongest charging currents. The next IC discharge occurs about 2 km away from the first discharge. The thunderstorm continues with many other IC discharges up to ~ 12 km away from the center of the storm for more than an hour. After this strong IC activity phase, a period of weak IC activity with some scattered lightning discharges is observed which lasts about 100 minutes. The lightning rates subsequently increase once again, this time with mostly CG lightning initiated below the main negative charge layer along with some IC discharges at higher altitudes.

6.4 Discussion

In the previous sections we explained the combination of the 3D model of thundercloud electric fields developed in Chapter 2 with a thundercloud charging model, and the use of the resultant new thunderstorm model with a separate lightning discharge

model, which enabled the simulation of long-timescale thunderstorm evolution.

The lightning discharge model which we used is the most important improvement in our study compared to the previous models of thunderstorm electrodynamics. The TDFL model solves for the electrodynamics and thermodynamics of the lightning channel based on fundamental physical principles. Moreover, the model simulates the lightning structure with a collection of lightning channel segments and thus does not have a fixed grid. Previous dielectric breakdown models of lightning discharge [Krehbiel *et al.*, 2008; Mansell *et al.*, 2002] do not include the physics of the lightning channel and are confined to propagation on the background grid structure which constrains the new leader channels to grow at a zero or 90 degree angle from the previous leader channel. Using the TDFL model for lightning discharge also enables us to use various spatial scales in our models. In particular, the large scale electric fields of the thundercloud charges are calculated on a coarse grid (1 km resolution), while the small scale electric fields of the lightning channels are determined on a fine spatial scale (100 m for the results shown in previous section).

The model results show many interesting aspects of thunderstorm electrical evolution. The sequence of lightning activity shown in Figure 6.6 is consistent with experimental observations of lightning evolution [Krehbiel, 1986]. Namely, the lightning activity often starts with IC discharges followed by the CG discharges that appear later in the storm lifetime. Another interesting observation is the generation of CG lightning from a dipole charge structure. As explained in Section 6.1 of this Chapter, all of the previous models of thunderstorm electrodynamics and lightning generation had indicated that the generation of CG lightning requires a lower positive charge layer. Based on these models, a cloud-to-ground lightning discharge initiates between the main negative and the lower positive charge layers.

However, our simulation results shown in the previous section suggest a new mechanism for the generation of CG discharges. The lightning activity starts with IC discharges since the strongest electric fields are first developed between the dipolar charge distribution layers and the lightning initiation threshold is lower at higher altitudes due to a lower atmospheric neutral density. Each IC discharge removes a

pocket of charge comparable in size to the lightning structure. The sequence of intracloud lightning activity removes the lower/upper surface of the positive/negative charge layers, which increases the effective distance between the remaining charges. This increase in the distance between the charges reduces the electric fields between the two layers. The fact that the electric fields are reduced below the lightning initiation threshold inhibits the lightning initiation as represented with the weak IC activity phase in Figure 6.6. The increased charge density in the lower part of the negative charge layer creates strong electric fields below the charge layer, which eventually overcome the initiation threshold for a discharge and lead to a cloud-to-ground discharge.

The above mechanism indicates that the generation of CG lightning does not necessarily require a lower positive charge layer. Nevertheless, the existence of the lower positive charge layer has been shown to assist the generation of CG discharges. The observations of CG discharges from a tripole charge structure with a lower positive charge layer could thus be due to both causes.

It is interesting to note that the results shown in the right-hand panels of Figure 6.5 suggest the possibility of the creation of the lower positive charge layer by negative cloud-to-ground discharges [Marshall and Winn, 1982; Holden *et al.*, 1983]. As suggested in these works, the deposition of the positive charge from the lightning channel of the $-CG$ discharges close to the lower boundary of the main negative charge layer inside the cloud may indeed be the mechanism that creates the lower positive charge layer. This mechanism, unlike other proposed mechanisms, is consistent with the observations that indicate “the main negative charge layer is laterally extensive and a major reservoir of charge in the storm, while the lower positive charge is more pointlike and a lesser reservoir of charge” [Krehbiel, 1986]. Although in our simulation we terminate the TDFL model after the lightning attaches to the ground, similar to the approach adopted by Mansell *et al.* [2005], we expect similar results even with further propagation of the in-cloud growth of lightning channels.

Similar to the main negative charge layer, the charge density in the upper boundary of the main positive charge layer also increases with time in the course of the simulation. Due to exponentially larger atmospheric conductivity at higher altitudes,

the electric fields at the upper side of the thunderstorm are better screened by the induced atmospheric charges. The observations of upward electric discharges such as blue jets and gigantic jets could be an indication of the deposition of the screening charges onto the particles at the upper boundary of the cloud, which creates a negatively charged screening layer within the cloud that could then assist in producing an upward discharge, consistently with the observations [*Krehbiel et al., 2008*]. However, these processes are neglected in our present study due to insufficient observational and theoretical support and our current limited understanding of their generation mechanisms.

Chapter 7

Conclusions and Suggestions for Future Work

7.1 Summary of results

In this work, we develop and apply for the first time a three dimensional model of thunderstorm electrodynamics and upward coupling to the ionosphere. Chapter 1 reviewed the important physical concepts related to this work starting with an overview of the Earth's electrical structure in Section 1.1. The parameters and characteristics of the Earth's upper atmosphere and its ionosphere relevant to this work were introduced. Thunderstorm electrodynamics and upward coupling processes were introduced in Section 1.2. Several cloud electrification mechanisms were reviewed in Section 1.2.1, followed by a brief introduction to lightning and its characteristics in Section 1.2.2. Sections 1.2.3 and 1.2.4 reviewed some of the current theories of upward electrodynamic coupling of thunderstorms, along with their experimental evidences like TLEs and early VLF events.

The quasi-electrostatic (QES) model described in Chapter 2 extends the previous work of *Pasko* [1996] from two to three spatial dimensions. Particularly, the inclusion of a realistic Earth geomagnetic field was explained in Section 2.5. In order to improve the computational performance of the model, domain decomposition techniques were used to parallelize the model as explained in Section 2.6. Two new numerical schemes

were designed and analyzed in Section 2.7 in order to achieve a larger stability region and to improve the performance of the numerical models.

Chapter 3 presented the results for the thunderstorm electrostatic fields generated by the accumulating charges inside a thundercloud. Two new findings of the model were that these fields are laterally displaced in the eastward and equatorial directions and are much stronger in magnitude than it was previously estimated by the 2D models.

Chapter 4 investigated the implications of the larger thundercloud fields and the resulting greater thundercloud upward energy coupling. Particularly, the sustained heating of the ionospheric electrons by the electrostatic fields was analyzed. Using a subionospheric VLF signal propagation model, it was found that the sustained heating mechanism for the Early/Fast events as proposed by *Inan et al.* [1996b] is a strong candidate that can explain many observations of these VLF events. Specifically, this mechanism can explain the vast range of the observed recovery rates of the VLF events which could not be explained by any other single mechanism. Moreover, the theoretical relation between the perturbation amplitude of the VLF signal and the ionospheric electron density profile and the geomagnetic dip angle was established in Section 4.4.

The results of the model application to 3D simulation of the lightning quasi-electrostatic fields and sprite halos are presented in Chapter 5. First, in Section 5.3.1, the effects of the Earth's geomagnetic field were investigated to test the previous predictions of *Tonev and Velinov* [2005]. Our model results indicated that lightning quasi-electrostatic fields significantly heat the ionospheric electrons and thus demagnetize the electrons by increasing their effective collision frequency. Therefore, the predicted eastward shifts in the model of *Tonev and Velinov* [2005] was attributed to the limitation of their model, which was unable to take into account the electron conductivity changes self-consistently. Section 5.3.2 presented the effects of the background neutral density fluctuations caused by thunderstorm driven gravity waves. It was concluded that the existence of gravity waves above thunderstorms may be responsible for the observations of sprite clusters, by helping the sprite steamer initiation from within or below the sprite halos at locations determined by the variations

of background atmosphere density in the gravity wave.

The application of the model to long timescale thunderstorm and lightning activity evolution studies was presented in Chapter 6. Using an accurate and physics-based lightning discharge model, several hours of thunderstorm electrodynamics and lightning activity was simulated. The model successfully reproduced the experimentally observed IC to CG transition of the lightning activity with a thunderstorm dipolar charge distribution. Furthermore, a new mechanism for creation of CG discharges was proposed based on the model results and the simulated thunderstorm electro-dynamics. The new CG discharge process does not require the existence of a lower positive charge layer in the thunderstorm charge structure as a necessary condition. On the other hand, the model results support the previously proposed theories of creation of the lower positive charge layer as a result of the $-$ CG lightning activity.

The scientific contributions of the work presented in this dissertation are:

1. Developed a parallel 2D and the first parallel 3D and self-consistent model of the nonlinear upward coupling of quasi-electrostatic thundercloud fields;
2. Predicted an eastward and equatorial shift in the high-altitude electric fields created by thunderclouds;
3. By including the geomagnetic field direction, demonstrated that thundercloud electric field intensities in the mesosphere were until now underestimated;
4. Constructed a full thunderstorm development model by integrating a thundercloud charging model, the quasi-electrostatic model and a time domain lightning fractal model;
5. Simulated long-timescale thunderstorm development and reproduced IC to CG evolution of thundercloud discharges; and
6. Proposed a new mechanism for development of cloud-to-ground lightning from dipolar charge layers.

7.2 Suggestions for Future Work

The current model used for the upward electrodynamic coupling of thunderstorms is only capable of simulating sprite halos. Drift-diffusion fluid equations are needed to simulate the sprite streamer physics which can be included similar to the previously published studies [*Luque and Ebert, 2009; Qin et al., 2011*, etc.]. Multi-scale simulation of sprite halos and sprite streamers can be performed using the parallel 2D model as developed in Chapter 2. 3D modeling of sprite streamers branching mechanisms and off-axis streamer initiations are also very important studies that have not yet been performed.

Although for the purposes of this dissertation, the numerical schemes presented in Section 2.7 produced stable results, more rigorous mathematical analysis is needed to establish their accuracy and stability region criteria more precisely, if they are to be used for other applications. Additionally, efforts could be made to use general purpose computing on graphic processing units (GPGPU) to increase the computational performance significantly.

The long-timescale model of the ionosphere heating (Chapters 3, 4) may be improved in accuracy by including more physical processes. In particular, additional chemical processes of the ionosphere plasma need to be included [*Gordillo-Vazquez et al., 2008*].

A quantitative analysis of the role of the thundercloud electrostatic fields as the generation mechanism for whistler ducts is needed for the non-vertical geomagnetic field, as pointed out in the Discussion in Chapter 3. This analysis can yield potentially very interesting results since the resultant upward coupling of electrostatic fields is predicted to be significantly different from axially-symmetric solutions with vertical geomagnetic field. Particularly, the thunderstorm electrostatic fields penetrate easier to ionospheric heights at lower latitudes which in turn are mapped to the equatorial magnetosphere with less attenuation.

Currently, only a 2D slab of the 3D domain solutions of the electron disturbances are used in modeling the interaction of the VLF transmitter signals with the lightning produced ionospheric disturbances. A 3D model of VLF signal propagation [*Lehtinen*

and Inan, 2009; Foust et al., 2011] is needed to take into account the full 3D solution of the thundercloud quasi-electrostatic fields. Such a model would reduce the 2D model error in the calculated signal amplitude perturbation, as well as allowing to test the theory by direct comparison with observations, e.g., those of *Johnson et al. [1999]*.

Effects of the non-vertical magnetic field direction, horizontal charge transfer, ionospheric irregularities, and realistic charge distribution inside the thundercloud on the lightning-generated quasi-electrostatic fields in the mesosphere need further analysis and quantitative investigations. For the studies of thunderstorm electrodynamic and lightning evolution, a more detailed charging model could be used similar to those used by *Mansell et al. [2005]*. Currently, most of the thunderstorm electrodynamic simulation time is spent in the lightning discharge model which is a sequential code [*Liang, 2014*]. Parallel techniques or other software performance optimization techniques could be used to increase the speed of the lightning discharge model and thus decrease the total thunderstorm simulation time.

Bibliography

- Ahrens, C. D. (2007), *Meteorology today*, Thomson Brooks/Cole, CA, USA. 537pp.
- Armstrong, W. (1983), Recent advances from studies of the Trimpf effect, *Antarct. JUS*, 18, 281–283.
- Baginski, M., and A. Hodel (1994), A case study comparing the lossy wave equation to the continuity equation in modeling late-time fields associated with lightning, *Applied Computational Electromagnetics Society Journal*, 9(2), 98–110.
- Baker, B., M. Baker, E. Jayaratne, J. Latham, and C. Saunders (1987), The influence of diffusional growth rates on the charge transfer accompanying rebounding collisions between ice crystals and soft hailstones, *Quarterly Journal of the Royal Meteorological Society*, 113(478), 1193–1215.
- Barrington-Leigh, C. P., U. S. Inan, and M. Stanley (2001), Identification of sprites and elves with intensified video and broadband array photometry, *Journal of Geophysical Research: Space Physics (1978–2012)*, 106(A2), 1741–1750, doi:10.1029/2000JA000073.
- Barrington-Leigh, C. P., V. P. Pasko, and U. S. Inan (2002), Exponential relaxation of optical emissions in sprites, *Journal of Geophysical Research: Space Physics (1978–2012)*, 107(A5), SIA–6, doi:10.1029/2001JA900117.
- Bell, T. F., S. C. Reising, and U. S. Inan (1998), Intense continuing currents following positive cloud-to-ground lightning associated with red sprites, *Geophysical Research Letters*, 25(8), 1285–1288.

- Boeck, W. L., O. H. Vaughan, R. Blakeslee, B. Vonnegut, and M. Brook (1992), Lightning induced brightening in the airglow layer, *Geophysical Research Letters*, *19*(2), 99–102, doi:10.1029/91GL03168.
- Brooks, I., and C. Saunders (1994), An experimental investigation of the inductive mechanism of thunderstorm electrification, *Journal of geophysical research*, *99*(D5), 10,627–10,632.
- Carlson, B. E. (2009), Terrestrial gamma-ray flash production by lightning, Ph.D. thesis, Stanford University.
- Carlson, B. E., C. Liang, P. Bitzer, and H. Christian (2015), Time domain simulations of preliminary breakdown pulses in natural lightning, *Journal of Geophysical Research: Atmospheres*, *120*(11), 5316–5333, doi:10.1002/2014JD022765, 2014JD022765.
- Carpenter, D. L., and U. S. Inan (1987), Seasonal, latitudinal and diurnal distributions of whistler-induced electron precipitation events, *Journal of Geophysical Research: Space Physics (1978–2012)*, *92*(A4), 3429–3435.
- Chen, A. B., C.-L. Kuo, Y.-J. Lee, H.-T. Su, R.-R. Hsu, J.-L. Chern, H. U. Frey, S. B. Mende, Y. Takahashi, H. Fukunishi, Y.-S. Chang, T.-Y. Liu, and L.-C. Lee (2008), Global distributions and occurrence rates of transient luminous events, *Journal of Geophysical Research: Space Physics*, *113*(A8), doi:10.1029/2008JA013101, a08306.
- Chevalier, T. W., U. S. Inan, and T. F. Bell (2008), Terminal impedance and antenna current distribution of a VLF electric dipole in the inner magnetosphere, *Antennas and Propagation, IEEE Transactions on*, *56*(8), 2454–2468, doi:10.1109/TAP.2008.927497.
- Christian, H. J., R. J. Blakeslee, D. J. Boccippio, W. L. Boeck, D. E. Buechler, K. T. Driscoll, S. J. Goodman, J. M. Hall, W. J. Koshak, D. M. Mach, et al. (2003), Global frequency and distribution of lightning as observed from space by the optical

- transient detector, *Journal of Geophysical Research: Atmospheres (1984–2012)*, *108*(D1), ACL–4.
- Cotts, B. R., and U. S. Inan (2007), Vlf observation of long ionospheric recovery events, *Geophysical Research Letters*, *34*(14).
- Cox, S., and P. Matthews (2002), Exponential time differencing for stiff systems, *Journal of Computational Physics*, *176*(2), 430–455.
- Cummer, S. A., and U. S. Inan (1997), Measurement of charge transfer in sprite-producing lightning using elf radio atmospherics, *Geophysical Research Letters*, *24*(14), 1731–1734, doi:10.1029/97GL51791.
- Cummer, S. A., J. Li, F. Han, G. Lu, N. Jaugey, W. A. Lyons, and T. E. Nelson (2009), Quantification of the troposphere-to-ionosphere charge transfer in a gigantic jet, *Nature Geoscience*, *2*(9), 617–620.
- Dash, J., B. Mason, and J. Wetzlauffer (2001), Theory of charge and mass transfer in ice-ice collisions, *Journal of Geophysical Research: Atmospheres (1984–2012)*, *106*(D17), 20,395–20,402.
- Davies, D. (1983), Measurements of swarm parameters in dry air, *Tech. rep.*, Westinghouse R&D Center, Pittsburg.
- Davis, M., and A. Da Rosa (1969), Traveling ionospheric disturbances originating in the auroral oval during polar substorms, *Journal of Geophysical Research*, *74*(24), 5721–5735.
- Dejnakarintra, M., and C. Park (1974), Lightning-induced electric fields in the ionosphere, *Journal of Geophysical Research*, *79*(13), 1903–1910.
- Dowden, R., C. Adams, J. Brundell, and P. Dowden (1994), Rapid onset, rapid decay (RORD), phase and amplitude perturbations of VLF subionospheric transmissions, *Journal of Atmospheric and Terrestrial Physics*, *56*(11), 1513–1527, doi:10.1016/0021-9169(94)90118-X.

- Dwyer, J. (2003), A fundamental limit on electric fields in air, *Geophysical Research Letters*, *30*(20).
- Dwyer, J. (2005), The initiation of lightning by runaway air breakdown, *Geophysical research letters*, *32*(20).
- Falgout, R. D., J. E. Jones, and U. M. Yang (2006), The design and implementation of hypre, a library of parallel high performance preconditioners, in *Numerical solution of partial differential equations on parallel computers*, pp. 267–294, Springer.
- Ferguson, J., F. Snyder, D. Morfitt, and C. Shellman (1989), Longwave Propagation Capability and Documentation, *Tech. Doc., Naval Ocean Systems Center, San Diego, CA*.
- Foust, F., M. Spasojevic, T. Bell, and U. Inan (2011), Modeling scattering from lightning-induced ionospheric disturbances with the discontinuous galerkin method, *Journal of Geophysical Research: Space Physics (1978–2012)*, *116*(A12).
- Franz, R., R. Nemzek, and J. Winckler (1990), Television image of a large upward electrical discharge above a thunderstorm system, *Science*, *249*(4964), 48–51.
- Fukunishi, H., Y. Takahashi, M. Kubota, K. Sakanoi, U. S. Inan, and W. A. Lyons (1996), Elves: Lightning-induced transient luminous events in the lower ionosphere, *Geophysical Research Letters*, *23*(16), 2157–2160, doi:10.1029/96GL01979.
- Gerken, E., U. S. Inan, and C. P. Barrington-Leigh (2000), Telescopic imaging of sprites, *Geophysical Research Letters*, *27*(17), 2637–2640, doi:10.1029/2000GL000035.
- Gerken, E. A., and U. S. Inan (2002), A survey of streamer and diffuse glow dynamics observed in sprites using telescopic imagery, *Journal of Geophysical Research: Space Physics (1978–2012)*, *107*(A11), SIA–4, doi:10.1029/2002JA009248.
- Goldberg, R., J. Barcus, L. Hale, and S. Curtis (1986), Direct observation of magnetospheric electron precipitation stimulated by lightning, *Journal of atmospheric and terrestrial physics*, *48*(3), 293–299.

- Gordillo-Vazquez, F. J., et al. (2008), Air plasma kinetics under the influence of sprites, *Journal Of Physics. D. Applied Physics*, *41*(23), 234,016.
- Gurevich, A., G. Milikh, and R. Roussel-Dupre (1992), Runaway electron mechanism of air breakdown and preconditioning during a thunderstorm, *Physics Letters A*, *165*(5), 463–468.
- Gurevich, A. V., and K. P. Zybin (2001), Runaway breakdown and electric discharges in thunderstorms, *Physics-Uspeski*, *44*(11), 1119.
- Haldoupis, C., T. Neubert, U. Inan, A. Mika, T. H. Allin, and R. Marshall (2004), Subionospheric early VLF signal perturbations observed in one-to-one association with sprites, *Journal of Geophysical Research: Space Physics (1978–2012)*, *109*(A10), doi:10.1029/2004JA010651.
- Haldoupis, C., R. Steiner, A. Mika, S. Shalimov, R. Marshall, U. Inan, T. Bösinger, and T. Neubert (2006), “early/slow” events: A new category of VLF perturbations observed in relation with sprites, *Journal of Geophysical Research: Space Physics (1978–2012)*, *111*(A11), doi:10.1029/2006JA011960.
- Hale, L. C. (1984), Middle atmosphere electrical structure, dynamics and coupling, *Advances in Space Research*, *4*(4), 175–186, doi:10.1016/0273-1177(84)90283-7.
- Hale, L. C. (1994), Coupling of ELF/ULF energy from lightning and MeV particles to the middle atmosphere, ionosphere, and global circuit, *Journal of Geophysical Research: Atmospheres (1984–2012)*, *99*(D10), 21,089–21,096.
- Hampton, D., M. Heavner, E. Wescott, and D. Sentman (1996), Optical spectral characteristics of sprites, *Geophysical Research Letters*, *23*(1), 89–92.
- Han, F., and S. A. Cummer (2010), Midlatitude nighttime D region ionosphere variability on hourly to monthly time scales, *Journal of Geophysical Research: Space Physics (1978–2012)*, *115*(A9).
- Helliwell, R., J. Katsufakis, and M. Trimpi (1973), Whistler-induced amplitude perturbation in VLF propagation, *J. geophys. Res.*, *78*(22), 4679–4688.

- Helsdon, J. H., S. Gattaleeradapan, R. D. Farley, and C. C. Waits (2002), An examination of the convective charging hypothesis: Charge structure, electric fields, and Maxwell currents, *Journal of Geophysical Research: Atmospheres*, *107*(D22), ACL 9–1–ACL 9–26, doi:10.1029/2001JD001495, 4630.
- Hines, C. (1960), Internal atmospheric gravity waves at ionospheric heights, *Canadian Journal of Physics*, *38*(11), 1441–1481.
- Holden, D., C. Holmes, C. Moore, W. Winn, J. Cobb, J. Griswold, and D. Lytle (1983), Local charge concentrations in thunderclouds, in *Sixth International Conference on Atmospheric Electricity (University of Manchester, Manchester, England, 1980)*.
- Holzer, R. E., and D. S. Saxon (1952), Distribution electrical conduction currents in the vicinity of thunderstorms, *Journal of Geophysical Research*, *57*(2), 207–216, doi:10.1029/JZ057i002p00207.
- Holzworth, R., M. Kelley, C. Siefring, L. Hale, and J. Mitchell (1985), Electrical measurements in the atmosphere and the ionosphere over an active thunderstorm: 2. Direct current electric fields and conductivity, *Journal of Geophysical Research: Space Physics (1978–2012)*, *90*(A10), 9824–9830.
- Hu, W., S. A. Cummer, W. A. Lyons, and T. E. Nelson (2002), Lightning charge moment changes for the initiation of sprites, *Geophysical Research Letters*, *29*(8), 120–1, doi:10.1029/2001GL014593.
- Hu, W., S. Cummer, and W. Lyons (2007), Testing sprite initiation theory using lightning measurements and modeled electromagnetic fields, *Journal of Geophysical Research: Atmospheres (1984–2012)*, *112*(D13), doi:10.1029/2006JD007939.
- Illingworth, A. (1972), Electric field recovery after lightning as the response of the conducting atmosphere to a field change, *Quarterly Journal of the Royal Meteorological Society*, *98*(417), 604–616.

- Inan, U., and J. Rodriguez (1993), Lightning-induced effects on VLF/LF radio propagation, *Had-A267* 991.
- Inan, U., D. Carpenter, R. Helliwell, and J. Katsufakis (1985), Subionospheric VLF/LF phase perturbations produced by lightning-whistler induced particle precipitation, *Journal of Geophysical Research: Space Physics (1978–2012)*, 90(A8), 7457–7469.
- Inan, U., C. Barrington-Leigh, S. Hansen, V. Glukhov, T. Bell, and R. Rairden (1997), Rapid lateral expansion of optical luminosity in lightning-induced ionospheric flashes referred to as elves, *Geophys. Res. Lett*, 24(5), 583–586.
- Inan, U. S., and D. L. Carpenter (1986), On the correlation of whistlers and associated subionospheric vlf/lf perturbations, *Journal of Geophysical Research: Space Physics (1978–2012)*, 91(A3), 3106–3116.
- Inan, U. S., D. Shafer, W. Yip, and R. Orville (1988), Subionospheric VLF signatures of nighttime D region perturbations in the vicinity of lightning discharges, *Journal of Geophysical Research: Space Physics (1978–2012)*, 93(A10), 11,455–11,472.
- Inan, U. S., T. F. Bell, and J. V. Rodriguez (1991), Heating and ionization of the lower ionosphere by lightning, *Geophysical Research Letters*, 18(4), 705–708.
- Inan, U. S., J. V. Rodriguez, and V. Idone (1993), VLF signatures of lightning-induced heating and ionization of the nighttime D-region, *Geophysical Research Letters*, 20(21), 2355–2358.
- Inan, U. S., T. F. Bell, V. Pasko, D. Sentman, E. Wescott, and W. Lyons (1995), VLF signatures of ionospheric disturbances associated with sprites, *Geophysical Research Letters*, 22(24), 3461–3464, doi:10.1029/95GL03507.
- Inan, U. S., A. Slingeland, V. Pasko, and J. Rodriguez (1996a), VLF and LF signatures of mesospheric/lower ionospheric response to lightning discharges, *Journal of Geophysical Research: Space Physics (1978–2012)*, 101(A3), 5219–5238, doi: 10.1029/95JA03514.

- Inan, U. S., V. P. Pasko, and T. F. Bell (1996b), Sustained heating of the ionosphere above thunderstorms as evidenced in “early/fast” VLF events, *Geophysical Research Letters*, *23*(10), 1067–1070, doi:10.1029/96GL01360.
- Inan, U. S., D. Piddiyachiy, W. B. Peter, J. Sauvaud, and M. Parrot (2007), DEMETER satellite observations of lightning-induced electron precipitation, *Geophysical research letters*, *34*(7).
- Jackson, J. D. (1999), *Classical Electrodynamics*, John Wiley & Sons, Hoboken, NJ.
- Jayarathne, E., C. Saunders, and J. Hallett (1983), Laboratory studies of the charging of soft-hail during ice crystal interactions, *Quarterly Journal of the Royal Meteorological Society*, *109*(461), 609–630.
- Johnson, M., U. Inan, S. Lev-Tov, and T. Bell (1999), Scattering pattern of lightning-induced ionospheric disturbances associated with early/fast VLF events, *Geophysical Research Letters*, *26*(15), 2363–2366, doi:10.1029/1999GL900521.
- Kabirzadeh, R., N. G. Lehtinen, and U. S. Inan (2015), Latitudinal dependence of static mesospheric E -fields above thunderstorms, *Geophysical Research Letters*, *42*(10), 4208–4215, doi:10.1002/2015GL064042.
- Kelley, M. C. (2009), *The Earth’s Ionosphere: Plasma Physics & Electrodynamics*, vol. 96, Academic press.
- Krehbiel, P. R. (1986), The electrical structure of thunderstorms, *The Earths Electrical Environment*, pp. 90–113.
- Krehbiel, P. R., M. Brook, and R. A. McCrory (1979), An analysis of the charge structure of lightning discharges to ground, *Journal of Geophysical Research: Oceans (1978–2012)*, *84*(C5), 2432–2456.
- Krehbiel, P. R., J. A. Rioussset, V. P. Pasko, R. J. Thomas, W. Rison, M. A. Stanley, and H. E. Edens (2008), Upward electrical discharges from thunderstorms, *Nature Geoscience*, *1*(4), 233–237.

- Lehtinen, N., M. Walt, U. Inan, T. Bell, and V. Pasko (1996), γ -ray emission produced by a relativistic beam of runaway electrons accelerated by quasi-electrostatic thundercloud fields, *Geophysical research letters*, *23*(19), 2645–2648.
- Lehtinen, N. G., and U. S. Inan (2009), Full-wave modeling of transionospheric propagation of vlf waves, *Geophysical Research Letters*, *36*(3).
- Lehtinen, N. G., T. F. Bell, V. Pasko, and U. Inan (1997), A two-dimensional model of runaway electron beams driven by quasi-electrostatic thundercloud fields, *Geophysical research letters*, *24*(21), 2639–2642.
- Leyser, T., U. Inan, D. Carpenter, and M. Trimpi (1984), Diurnal variation of burst precipitation effects on subionospheric VLF/LF signal propagation near L= 2, *Journal of Geophysical Research*, *89*, 9139–9143.
- Liang, C. (2014), Electrodynamic and thermodynamic modeling of the lightning channel, Ph.D. thesis, Stanford University.
- Liu, N. (2012), Multiple ion species fluid modeling of sprite halos and the role of electron detachment of O⁻ in their dynamics, *Journal of Geophysical Research: Space Physics (1978–2012)*, *117*(A3), doi:10.1029/2011JA017062.
- Liu, N., J. R. Dwyer, H. C. Stenbaek-Nielsen, and M. G. McHarg (2015), Sprite streamer initiation from natural mesospheric structures, *Nature communications*, *6*.
- Lu, G., S. A. Cummer, W. A. Lyons, P. R. Krehbiel, J. Li, W. Rison, R. J. Thomas, H. E. Edens, M. A. Stanley, W. Beasley, et al. (2011), Lightning development associated with two negative gigantic jets, *Geophysical Research Letters*, *38*(12).
- Luque, A., and U. Ebert (2009), Emergence of sprite streamers from screening-ionization waves in the lower ionosphere, *Nature Geoscience*, *2*(11), 757–760, doi: 10.1038/NGEO662.

- Luque, A., and F. Gordillo-Vázquez (2012), Mesospheric electric breakdown and delayed sprite ignition caused by electron detachment, *Nature Geoscience*, 5(1), 22–25.
- Luque, A., F. Brau, and U. Ebert (2008), Saffman-Taylor streamers: Mutual finger interaction in spark formation, *Physical Review E*, 78(1), 016,206.
- Lyons, W. A., et al. (1996), Sprite observations above the US High Plains in relation to their parent thunderstorm systems, *Journal of Geophysical Research. D. Atmospheres*, 101, 29,641–29,652.
- Mansell, E. R. (2000), Electrification and lightning in simulated supercell and non-supercell thunderstorms, Ph.D. thesis, University of Oklahoma.
- Mansell, E. R., D. R. MacGorman, C. L. Ziegler, and J. M. Straka (2002), Simulated three-dimensional branched lightning in a numerical thunderstorm model, *Journal of Geophysical Research: Atmospheres (1984–2012)*, 107(D9), ACL–2.
- Mansell, E. R., D. R. MacGorman, C. L. Ziegler, and J. M. Straka (2005), Charge structure and lightning sensitivity in a simulated multicell thunderstorm, *Journal of Geophysical Research: Atmospheres (1984–2012)*, 110(D12).
- Marshall, R., and J. Snively (2014), Very low frequency subionospheric remote sensing of thunderstorm-driven acoustic waves in the lower ionosphere, *Journal of Geophysical Research: Atmospheres*, 119(9), 5037–5045, doi:10.1002/2014JD021594.
- Marshall, R. A. (2009), Very low frequency radio signatures of transient luminous events above thunderstorms, Ph.D. thesis, Stanford University.
- Marshall, R. A. (2012), An improved model of the lightning electromagnetic field interaction with the D-region ionosphere, *Journal of Geophysical Research: Space Physics (1978–2012)*, 117(A3), doi:10.1029/2011JA017408.
- Marshall, R. A., U. S. Inan, and W. Lyons (2006), On the association of early/fast

- very low frequency perturbations with sprites and rare examples of VLF backscatter, *Journal of Geophysical Research: Atmospheres (1984–2012)*, 111(D19), doi:10.1029/2006JD007219.
- Marshall, R. A., U. S. Inan, and T. Chevalier (2008), Early VLF perturbations caused by lightning EMP-driven dissociative attachment, *Geophysical Research Letters*, 35(21), doi:10.1029/2008GL035358.
- Marshall, R. A., U. S. Inan, and V. Glukhov (2010), Elves and associated electron density changes due to cloud-to-ground and in-cloud lightning discharges, *Journal of Geophysical Research: Space Physics (1978–2012)*, 115(A4), doi:10.1029/2009JA014469.
- Marshall, T., M. Stolzenburg, C. Maggio, L. Coleman, P. Krehbiel, T. Hamlin, R. Thomas, and W. Rison (2005), Observed electric fields associated with lightning initiation, *Geophysical research letters*, 32(3).
- Marshall, T. C., and W. D. Rust (1991), Electric field soundings through thunderstorms, *Journal of Geophysical Research: Atmospheres (1984–2012)*, 96(D12), 22,297–22,306.
- Marshall, T. C., and W. P. Winn (1982), Measurements of charged precipitation in a new mexico thunderstorm: Lower positive charge centers, *Journal of Geophysical Research: Oceans (1978–2012)*, 87(C9), 7141–7157.
- Marshall, T. C., M. P. McCarthy, and W. D. Rust (1995a), Electric field magnitudes and lightning initiation in thunderstorms, *Journal of Geophysical Research: Atmospheres (1984–2012)*, 100(D4), 7097–7103.
- Marshall, T. C., W. Rison, W. D. Rust, M. Stolzenburg, J. C. Willett, and W. P. Winn (1995b), Rocket and balloon observations of electric field in two thunderstorms, *Journal of Geophysical Research: Atmospheres (1984–2012)*, 100(D10), 20,815–20,828.

- Mason, J. (1988), The generation of electric charges and fields in thunderstorms, in *Proceedings of the Royal Society of London A: Mathematical, Physical and Engineering Sciences*, vol. 415, pp. 303–315, The Royal Society.
- McCormick, R. J., C. J. Rodger, and N. R. Thomson (2002), Reconsidering the effectiveness of quasi-static thunderstorm electric fields for whistler duct formation, *Journal of Geophysical Research: Space Physics (1978–2012)*, *107*(A11), SIA–16.
- Mende, S., R. L. Rairden, G. Swenson, and W. Lyons (1995), Sprite spectra; N₂ 1 PG band identification, *Geophysical Research Letters*, *22*(19), 2633–2636.
- Mende, S., H. Frey, R.-R. Hsu, H. Su, A. Chen, L. Lee, D. Sentman, Y. Takahashi, and H. Fukunishi (2005), D region ionization by lightning-induced electromagnetic pulses, *Journal of Geophysical Research: Space Physics (1978–2012)*, *110*(A11).
- Mika, A., C. Haldoupis, R. Marshall, T. Neubert, and U. Inan (2005), Subionospheric VLF signatures and their association with sprites observed during eurosprite-2003, *Journal of atmospheric and solar-terrestrial physics*, *67*(16), 1580–1597, doi:10.1016/j.jastp.2005.08.011.
- Mika, A., C. Haldoupis, T. Neubert, H.-T. Su, R.-R. Hsu, R. Steiner, and R. Marshall (2006), Early VLF perturbations observed in association with elves, in *Annales Geophysicae*, vol. 24, pp. 2179–2189, doi:10.5194/angeo-24-2179-2006.
- Moelter, M. J., J. Evans, G. Elliott, and M. Jackson (1998), Electric potential in the classical hall effect: An unusual boundary-value problem, *American Journal of Physics*, *66*(8), 668–677.
- Moin, P. (2010), *Fundamentals of engineering numerical analysis*, Cambridge University Press.
- Moore, R. C., C. P. Barrington-Leigh, U. S. Inan, and T. F. Bell (2003), Early/fast VLF events produced by electron density changes associated with sprite halos, *Journal of Geophysical Research: Space Physics (1978–2012)*, *108*(A10), doi:10.1029/2002JA009816.

- Moudry, D., H. Stenbaek-Nielsen, D. Sentman, and E. Wescott (2003), Imaging of elves, halos and sprite initiation at 1ms time resolution, *Journal of atmospheric and solar-terrestrial physics*, *65*(5), 509–518, doi:10.1016/S1364-6826(02)00323-1.
- Papadopoulos, K., G. Milikh, A. Gurevich, A. Drobot, and R. Shanny (1993), Ionization rates for atmospheric and ionospheric breakdown, *Journal of Geophysical Research: Space Physics (1978–2012)*, *98*(A10), 17,593–17,596.
- Park, C., and M. Dejnakarindra (1973), Penetration of thundercloud electric fields into the ionosphere and magnetosphere: 1. Middle and subauroral latitudes, *Journal of Geophysical Research*, *78*(28), 6623–6633.
- Park, C., and R. Helliwell (1971), The formation by electric fields of field-aligned irregularities in the magnetosphere, *Radio Science*, *6*(2), 299–304, doi:10.1029/RS006i002p00299.
- Pasko, V., U. Inan, and T. Bell (1996), Blue jets produced by quasi-electrostatic pre-discharge thundercloud fields, *Geophysical Research Letters*, *23*(3), 301–304.
- Pasko, V., U. Inan, T. Bell, and Y. N. Taranenko (1997a), Sprites produced by quasi-electrostatic heating and ionization in the lower ionosphere, *Journal of Geophysical Research: Space Physics (1978–2012)*, *102*(A3), 4529–4561.
- Pasko, V. P. (1996), Dynamic coupling of quasi-electrostatic thundercloud fields to the mesosphere and lower ionosphere: sprites and jets, Ph.D. thesis, Stanford University.
- Pasko, V. P., and U. S. Inan (1994), Recovery signatures of lightning-associated VLF perturbations as a measure of the lower ionosphere, *Journal of Geophysical Research: Space Physics (1978–2012)*, *99*(A9), 17,523–17,537, doi:10.1029/94JA01378.
- Pasko, V. P., and H. C. Stenbaek-Nielsen (2002), Diffuse and streamer regions of sprites, *Geophysical research letters*, *29*(10), 82–1, doi:10.1029/2001GL014241.

- Pasko, V. P., U. S. Inan, Y. N. Taranenkov, and T. F. Bell (1995), Heating, ionization and upward discharges in the mesosphere, due to intense quasi-electrostatic thundercloud fields, *Geophysical Research Letters*, *22*(4), 365–368.
- Pasko, V. P., U. S. Inan, and T. F. Bell (1997b), Sprites as evidence of vertical gravity wave structures above mesoscale thunderstorms, *Geophysical Research Letters*, *24*(14), 1735–1738.
- Pasko, V. P., U. S. Inan, and T. F. Bell (1998), Ionospheric effects due to electrostatic thundercloud fields, *Journal of atmospheric and solar-terrestrial physics*, *60*(7), 863–870, doi:10.1016/S1364-6826(98)00022-4.
- Pasko, V. P., M. A. Stanley, J. D. Mathews, U. S. Inan, and T. G. Wood (2002), Electrical discharge from a thundercloud top to the lower ionosphere, *Nature*, *416*(6877), 152–154.
- Pasko, V. P., J. Qin, and S. Celestin (2013), Toward better understanding of sprite streamers: initiation, morphology, and polarity asymmetry, *Surveys in Geophysics*, *34*(6), 797–830, doi:10.1007/s10712-013-9246-y.
- Peter, W. B. (2007), Quantitative measurement of lightning-induced electron precipitation using VLF remote sensing, Ph.D. thesis, Stanford University.
- Pulinets, S., K. Boyarchuk, V. Hegai, V. Kim, and A. Lomonosov (2000), Quasi-electrostatic model of atmosphere-thermosphere-ionosphere coupling, *Advances in Space Research*, *26*(8), 1209–1218.
- Qin, J., S. Celestin, and V. P. Pasko (2011), On the inception of streamers from sprite halo events produced by lightning discharges with positive and negative polarity, *Journal of Geophysical Research: Space Physics (1978–2012)*, *116*(A6).
- Qin, J., S. Celestin, and V. P. Pasko (2012), Minimum charge moment change in positive and negative cloud to ground lightning discharges producing sprites, *Geophysical Research Letters*, *39*(22), doi:10.1029/2012GL053951.

- Qin, J., V. P. Pasko, M. G. McHarg, and H. C. Stenbaek-Nielsen (2014), Plasma irregularities in the D-region ionosphere in association with sprite streamer initiation, *Nature communications*, 5.
- Quarteroni, A., and A. Valli (1999), *Domain decomposition methods for partial differential equations*, CMCS-BOOK-2009-019, Oxford University Press.
- Rakov, V. A., and M. A. Uman (2003), *Lightning: physics and effects*, Cambridge University Press.
- Rodger, C. J., N. R. Thomson, and R. L. Dowden (1998a), Testing the formulation of park and dejnakarindra to calculate thunderstorm dc electric fields, *Journal of Geophysical Research: Space Physics (1978–2012)*, 103(A2), 2171–2178.
- Rodger, C. J., N. R. Thomson, and R. L. Dowden (1998b), Are whistler ducts created by thunderstorm electrostatic fields?, *Journal of Geophysical Research: Space Physics (1978–2012)*, 103(A2), 2163–2169.
- Rodger, C. J., N. R. Thomson, and R. L. Dowden (2002), Correction to “are whistler ducts created by thunderstorm electrostatic fields?” by c. j. rodger et al., *Journal of Geophysical Research*, 107(A6), 1068, doi:10.1029/2001JA009152.
- Said, R., U. Inan, and K. Cummins (2010), Long-range lightning geolocation using a VLF radio atmospheric waveform bank, *Journal of Geophysical Research: Atmospheres (1984–2012)*, 115(D23).
- Sampath, H., U. Inan, and M. Johnson (2000), Recovery signatures and occurrence properties of lightning-associated subionospheric VLF perturbations, *Journal of Geophysical Research: Space Physics (1978–2012)*, 105(A1), 183–191.
- São Sabbas, F. T., D. D. Sentman, E. M. Wescott, O. Pinto, O. Mendes, and M. J. Taylor (2003), Statistical analysis of space–time relationships between sprites and lightning, *Journal of Atmospheric and Solar-Terrestrial Physics*, 65(5), 525–535, doi:10.1016/S1364-6826(02)00326-7.

- Saunders, C. (2008), Charge separation mechanisms in clouds, in *Planetary Atmospheric Electricity*, pp. 335–353, Springer.
- Sentman, D. D., E. M. Wescott, D. Osborne, D. Hampton, and M. Heavner (1995), Preliminary results from the Sprites94 aircraft campaign: 1. Red sprites, *Geophysical Research Letters*, *22*(10), 1205–1208, doi:10.1029/95GL00583.
- Silva, C. L., and V. P. Pasko (2013), Vertical structuring of gigantic jets, *Geophysical Research Letters*, *40*(12), 3315–3319.
- Simpson, G., and F. Scrase (1937), The distribution of electricity in thunderclouds, *Proceedings of the Royal Society of London. Series A, Mathematical and Physical Sciences*, pp. 309–352.
- Snively, J. B., and V. P. Pasko (2003), Breaking of thunderstorm-generated gravity waves as a source of short-period ducted waves at mesopause altitudes, *Geophysical research letters*, *30*(24).
- Stolzenburg, M., and T. C. Marshall (2008), Charge structure and dynamics in thunderstorms, *Space Science Reviews*, *137*(1-4), 355–372.
- Stolzenburg, M., W. D. Rust, B. F. Smull, and T. C. Marshall (1998a), Electrical structure in thunderstorm convective regions: 1. Mesoscale convective systems, *Journal of Geophysical Research: Atmospheres (1984–2012)*, *103*(D12), 14,059–14,078.
- Stolzenburg, M., W. D. Rust, and T. C. Marshall (1998b), Electrical structure in thunderstorm convective regions: 2. Isolated storms, *Journal of Geophysical Research: Atmospheres (1984–2012)*, *103*(D12), 14,079–14,096.
- Stolzenburg, M., W. D. Rust, and T. C. Marshall (1998c), Electrical structure in thunderstorm convective regions: 3. synthesis, *Journal of Geophysical Research: Atmospheres (1984–2012)*, *103*(D12), 14,097–14,108.

- Stolzenburg, M., T. C. Marshall, W. D. Rust, E. Bruning, D. R. MacGorman, and T. Hamlin (2007), Electric field values observed near lightning flash initiations, *Geophysical research letters*, *34*(4).
- Su, H.-T., R.-R. Hsu, A. Chen, Y. Wang, W. Hsiao, W. Lai, L.-C. Lee, M. Sato, and H. Fukunishi (2003), Gigantic jets between a thundercloud and the ionosphere, *Nature*, *423*(6943), 974–976.
- Sweers, G., B. Birch, and J. Gokcen (2004), lightning strikes: Protection, inspection, and repair, *AERO Quarterly. GTR*, *12*, 19–28.
- Symbalisty, E. M., R. A. Roussel-Dupré, D. O. ReVelle, D. M. Suszcynsky, V. A. Yukhimuk, and M. J. Taylor (2000), Meteor trails and columniform sprites, *Icarus*, *148*(1), 65–79.
- Takahashi, T. (1978), Riming electrification as a charge generation mechanism in thunderstorms, *Journal of the Atmospheric Sciences*, *35*(8), 1536–1548.
- Taranenko, Y. N., U. S. Inan, and T. F. Bell (1993a), The interaction with the lower ionosphere of electromagnetic pulses from lightning: Excitation of optical emissions, *Geophysical Research Letters*, *20*(23), 2675–2678, doi:10.1029/93GL02838.
- Taranenko, Y. N., U. S. Inan, and T. F. Bell (1993b), Interaction with the lower ionosphere of electromagnetic pulses from lightning: Heating, attachment, and ionization, *Geophysical Research Letters*, *20*(15), 1539–1542, doi:10.1029/93GL01696.
- Taylor, W. L. (1978), A VHF technique for space-time mapping of lightning discharge processes, *Journal of Geophysical Research: Oceans (1978–2012)*, *83*(C7), 3575–3583.
- Thomson, N. R., M. A. Clilverd, and W. M. McRae (2007), Nighttime ionospheric D region parameters from VLF phase and amplitude, *Journal of Geophysical Research: Space Physics (1978–2012)*, *112*(A7).

- Tonev, P., and P. Velinov (2002), Electrostatic fields above thunderclouds at different latitudes and their ionospheric effects, *Advances in Space Research*, 30(11), 2625–2630.
- Tonev, P., and P. Velinov (2005), Variations of quasi-electrostatic fields and ionosphere potential above lightning discharge at equatorial latitudes, *Advances in Space Research*, 35(8), 1461–1466.
- Tzur, I., and R. Roble (1985), The interaction of a dipolar thunderstorm with its global electrical environment, *Journal of Geophysical Research: Atmospheres (1984–2012)*, 90(D4), 5989–5999.
- Velinov, P., and P. Tonev (1995), Modelling the penetration of thundercloud electric fields into the ionosphere, *Journal of Atmospheric and Terrestrial Physics*, 57(6), 687–694.
- Vellinov, P., and P. Tonev (1994), Penetration of multipole thundercloud electric fields into the ionosphere, *Journal of atmospheric and terrestrial physics*, 56(3), 349–359.
- Veronis, G., V. P. Pasko, and U. S. Inan (1999), Characteristics of mesospheric optical emissions produced by lightning discharges, *Journal of Geophysical Research: Space Physics (1978–2012)*, 104(A6), 12,645–12,656, doi:10.1029/1999JA900129.
- Volland, H. (1984), *Atmospheric Electrodynamics*, vol. 11, Springer Science & Business Media.
- Voss, H., W. Imhof, M. Walt, J. Mobilia, E. Gaines, J. Reagan, U. Inan, R. Helliwell, D. Carpenter, J. Katsufakis, et al. (1984), Lightning-induced electron precipitation, *Nature*, doi:10.1038/312740a0.
- Wait, J. R., and K. P. Spies (1964), *Characteristics of the Earth-ionosphere waveguide for VLF radio waves*, 300, US Dept. of Commerce, National Bureau of Standards: for sale by the Supt. of Doc., US Govt. Print. Off.

- Wescott, E., H. Stenbaek-Nielsen, D. Sentman, M. Heavner, D. Moudry, and F. Sao Sabbas (2001), Triangulation of sprites, associated halos and their possible relation to causative lightning and micrometeors, *Journal of Geophysical Research: Space Physics (1978–2012)*, 106(A6), 10,467–10,477.
- Wescott, E. M., D. Sentman, D. Osborne, D. Hampton, and M. Heavner (1995), Preliminary results from the Sprites94 aircraft campaign: 2. Blue jets, *Geophysical research letters*, 22(10), 1209–1212.
- Williams, E. R. (1989), The tripole structure of thunderstorms, *Journal of Geophysical Research: Atmospheres (1984–2012)*, 94(D11), 13,151–13,167.
- Wilson, C. (1916), On some determinations of the sign and magnitude of electric discharges in lightning flashes, *Proceedings of the Royal Society of London. Series A, Containing Papers of a Mathematical and Physical Character*, pp. 555–574.
- Wilson, C. (1921), Investigations on lightning discharges and on the electric field of thunderstorms, *Philosophical Transactions of the Royal Society of London. Series A, Containing Papers of a Mathematical or Physical Character*, pp. 73–115.
- Wilson, C. (1924), The electric field of a thundercloud and some of its effects, *Proceedings of the Physical Society of London*, 37(1), 32D.
- Wilson, C. (1956), A theory of thundercloud electricity, in *Proceedings of the Royal Society of London A: Mathematical, Physical and Engineering Sciences*, vol. 236, pp. 297–317, The Royal Society.
- Wilson, C., et al. (1929), Some thundercloud problems, *Journal of the Franklin Institute*, 208(1), 1–12.
- Wilson, C. T. (1925), The acceleration of β -particles in strong electric fields such as those of thunderclouds, in *Mathematical Proceedings of the Cambridge Philosophical Society*, vol. 22, pp. 534–538, Cambridge Univ Press.

- Winckler, J. R., W. A. Lyons, T. E. Nelson, and R. J. Nemzek (1996), New high-resolution ground-based studies of sprites, *Journal of Geophysical Research: Atmospheres*, *101*(D3), 6997–7004, doi:10.1029/95JD03443.
- Yair, Y., P. Israelevich, A. D. Devir, M. Moalem, C. Price, J. H. Joseph, Z. Levin, B. Ziv, A. Sternlieb, and A. Teller (2004), New observations of sprites from the space shuttle, *Journal of Geophysical Research: Atmospheres (1984–2012)*, *109*(D15).
- Yamada, Y., H. Fukunishi, T. Nakamura, and T. Tsuda (2001), Breaking of small-scale gravity wave and transition to turbulence observed in oh airglow, *Geophysical research letters*, *28*(11), 2153–2156.
- Zabotin, N., and J. Wright (2001), Role of meteoric dust in sprite formation, *Geophysical research letters*, *28*(13), 2593–2596.
- Ziegler, C. L., P. S. Ray, and D. R. MacGorman (1986), Relations of kinematics, microphysics and electrification in an isolated mountain thunderstorm, *Journal of the atmospheric sciences*, *43*(19), 2098–2115.